Thermomechanical fatigue failure of interfaces in lead-free solders

Müge Erinç

This research was financially supported by the Dutch Technology Foundation STW (project number EWT.4924), applied science division of NWO and the technology program of the Ministry of Economic Affairs of the Netherlands.

CIP-DATA LIBRARY TECHNISCHE UNIVERSITEIT EINDHOVEN

Erinç, Müge

Thermomechanical fatigue failure of interfaces in lead-free solders.

Eindhoven University of Technology, 2007.
Proefschrift.

A catalogue record is available from the Eindhoven University of Technology Library. ISBN: 978-90-386-1149-5

This thesis is prepared with LaTeX2$_\epsilon$

Cover design: Sjoerd Cloos

Printed by the Universiteitsdrukkerij TU Eindhoven, Eindhoven, The Netherlands.

Thermomechanical fatigue failure of interfaces in lead-free solders

Proefschrift

ter verkrijging van de graad van doctor
aan de Technische Universiteit Eindhoven,
op gezag van de Rector Magnificus, prof.dr.ir. C.J. van Duijn,
voor een commissie aangewezen door het College voor Promoties
in het openbaar te verdedigen op
maandag 3 december 2007 om 16.00 uur

door

Müge Erinç

geboren te Ankara, Turkije

Dit proefschrift is goedgekeurd door de promotor:

prof.dr.ir. M.G.D. Geers

Copromotor:
dr.ir. P.J.G. Schreurs

Contents

Summary

Thermomechanical fatigue failure of interfaces in lead-free solders

The European Union Waste Electrical and Electronic Equipment Directive (WEEE) and Restriction of Hazardous Substances Directive (RoHS) banned lead from electronic systems from July 1, 2006 onwards, which has led to much interest in lead-free solders in the past years. Among several lead-free solder alternatives, SnAgCu is a widely accepted replacement due to its better creep-fatigue resistance and microstructural stability. SnAgCu has been extensively studied in the past decade, however, there are still issues to be resolved concerning solder reliability, the underlying mechanisms of thermo-mechanical fatigue failure, fatigue life predictions and the overall effect of decreasing component size, driven by the ongoing miniaturization trend. This thesis aims to scientifically contribute to this subject by a coupled experimental-numerical approach.

In solder joint reliability, the bump/pad interface has a crucial role, the quality of which is determined by the metallization and interfacial defects. Solder balls, solder paste and cast eutectic SnAgCu are reflowed on Cu, Ni/Au and Cu/Ni(V)/Au metallization layers and the substrate influence on the bulk and interfacial metallurgy is examined. The damage propagation at SnAgCu soldered joints on Cu and Ni/Au substrates are investigated and microstructure related damage localization is identified as the dominant failure mechanism. Therefore, continuum damage approaches are believed to be inadequate for solder joint reliability predictions. Nano-indentation and tensile testing is used for the mechanical characterization of SnAgCu. An assessment on indentation parameters for solders is conducted and the influence of the Ag content on material properties of SnAgCu is presented.

One of the main causes of ball grid array (BGA) failure is thermo-mechanical fatigue crack propagation in the solder, which is almost always observed at the bump/pad junction. Motivated by this fact, a combined experimental-numerical study on the cyclic mechanical response of SnAgCu/Ni-Au interface is conducted. In this study, damage evolution at the bond/pad interface is characterized by dedicated fatigue tests. Local deformations leading to crack propagation are simulated by separation

of interfaces through a cohesive zone approach. Solder joints are tested under cyclic shear and cyclic tension for different specimen sizes and strain amplitudes. Two different damage mechanisms are observed: local deformations in the bulk and at the bonding interface. The interfacial failure mode is typically favored at a high initial stress, and a small solder volume. Crack propagation is simulated by an irreversible linear traction-separation cohesive zone law accompanied by a non-linear interfacial damage parameter. Later, tensile and shear experiments are used to characterize the cohesive zone parameters for the normal and the tangential opening, respectively.

Interfacial fatigue damage in BGA solders is caused by the difference in coefficient of thermal expansion (CTE) of the materials in the package. Apart from this thermal incompatibility in the package, Sn based solders are themselves prone to thermal fatigue damage due to the intrinsic thermal anisotropy of the β-Sn phase. Thermal fatigue causes local deformations especially at the grain boundaries. Hence, the thermal fatigue response of bulk SnAgCu is investigated as well. Bulk SnAgCu specimens are thermally cycled between -40 and 125°C and mechanically tested afterwards in order to quantify the thermal fatigue damage. A size dependent cyclic softening behavior is observed. Test specimens are individually modeled including the microstructure and local crystallographic orientations, on the basis of orientation imaging scans (OIM). Both thermal cycling and tensile testing are imposed as boundary conditions. Reproducing the experimental results in the simulations, parameters of a cohesive zone based intergranular fatigue damage model are identified. Finally, the intergranular damage law characterized in this study is combined with the bump/pad interfacial damage law, and a 2D microstructure-incorporated fatigue life prediction tool is established. Using this tool, it is shown that the failure mode of a soldered joint depends extensively on its geometry.

The model presented above is extended to 3D for a more complete description of the problem. To provide the microstructural input, a database containing OIM scans of several SnAgCu solder balls is constructed. A missing constituent in the model so far, interfacial defects, i.e. voids, are examined statistically using newly manufactured BGA packages, revealing information on their size, position and frequency. Combining all the data collected, i.e. material properties, microstructure, defects, local damage laws, a 3D slice model from a BGA package is constructed. The slice model contains a single solder ball connecting the board and the chip. A series of case studies is created using experimental input such as different microstructures and initial defects allowing a statistical analysis. Fatigue life of these models are predicted and the results are validated by failure distribution analyses of BGA packages provided by the industry. Here the critical solder ball assumption is made: if a solder ball fails, the electrical circuit of the BGA package is open, thus the package fails. Setting a critical damage value for the interfaces accumulating fatigue damage, a good agreement with the experiments and simulations is obtained. It is seen that microstructural modeling allows to predict and understand the scatter in the solder ball fatigue life observed in reality.

Finally, the effect of solder ball size and geometry on interconnect reliability is dis-

cussed on the basis of numerical analyses. For this purpose, a geometry factor and a microstructure factor is defined, and their influence on damage evolution is discussed.

CHAPTER ONE

Introduction

1.1 Solders in Microelectronics

Soft solders are fusible metal alloys with a melting point up to 450°C, used to connect metallic surfaces, especially in the fields of electronics and plumbing. The most frequent application of soldering is assembling electronic components to printed circuit boards (PCBs). Today, miniaturization is the major driving force in consumer electronics design and production. Efforts in decreasing component dimensions have led to the development of ball grid array (BGA) and flip chip packages (Figure 1.1); with the introduction of BGAs more than 1000 in/out terminals can be placed in a single assembly. Bonding of the die to a substrate and its encapsulation is referred to as 1^{st} level, bonding of the mold and die to PCB is referred as 2^{nd} level packaging. In flip-chips, no wiring is necessary because the chip is flipped over and directly connected via tiny solder balls (ϕ <100 μm) to the board. The 2^{nd} level solder ball diameters are in the range of 300-760 μm. The pads on both the chip side and the printed circuit board side contain thin films of lamellar metallic layers, the so-called under bump metallization (UBM). The purpose of the UBM is to prevent oxidation of copper and to enhance wetting of solder to the pad. In commercial packages, standard UBM thickness is in the range of 5-20 μm.

As a joining material, solder provides electrical, thermal and mechanical continuity in electronic packages. Solder balls in a microelectronic assembly are subjected to different types of loading:

- Thermal cycling due to repeated power switching evokes heat related phenomena. In connection, the mismatch in the coefficient of thermal expansion (CTE) between the package components causes cyclic mechanical strains.
- As a result of the multi-phase nature of Sn based solder alloys and the thermal anisotropy of β-Sn, internal stresses build up in the solder.

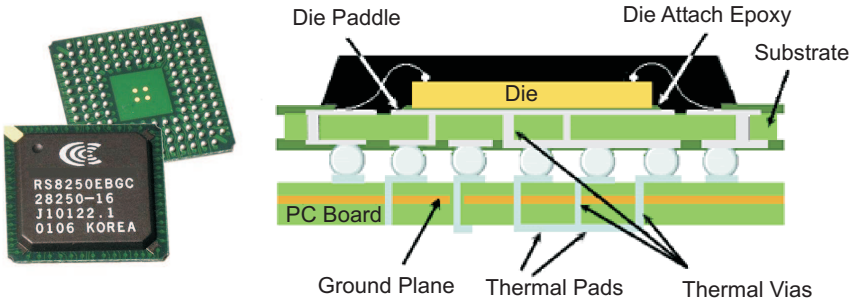

Figure 1.1: A commercial ball grid array package and its cross-section.

- Cyclic thermomechanical loading evokes creep-fatigue damage or creep rupture.
- Flex bending and buckling of the board induces bending moments as well as shear and tensile stresses on the solder joints.

The strains in a solder ball are dependent on the location of the ball on the BGA. The balls at corners experience the highest strains, resulting from a combination of shear stresses and large tensile stresses, decreasing towards a neutral point at the center. The outer solder balls are termed as the critical balls; they exhibit a high risk of failure compared to inner solder balls (Figure 1.2). Selection of an appropriate solder/substrate combination, in other words, the metallization, determines the long-term joint reliability since failure often occurs near metallization layers.

Imposed by the European Union Waste Electrical and Electronic Equipment Directive (WEEE) and Restriction of Hazardous Substances Directive (RoHS), lead is banned from electronic systems by July 1, 2006 except a limited number of special applications, triggering much interest in lead-free solders. Apart from the legal enforcement, there are also a number of technological drivers emerging from the miniaturization trend:

- Miniaturization enforces the pitch size to be continuously reduced. The internal liquid pressure of molten SnPb does not allow production of very small solder balls, because the SnPb droplet cannot solidify preserving the radius of curvature.
- Furthermore, smaller packages result in high current densities causing overheating in heat-sink parts, such as the solder balls. It is well established that SnPb is highly susceptible to heat, invoking coarsening in the eutectic lamellae which further leads to mixed creep-fatigue failure at the phase boundaries.

Due to the reasons stated above, lead-free solder alternatives have become an important research topic for the microelectronics industry. SnAgCu was indicated as the most promising solder in avionics and automotive applications where the solder joints are subjected to numerous thermal cycles and mechanical vibrations,

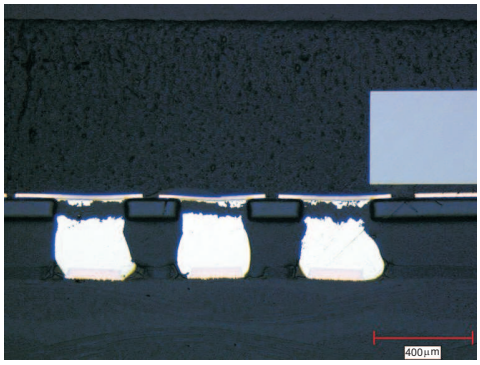

Figure 1.2: BGA solder balls after N=2000 thermal cycles, ΔT = -45 to 125 °C, courtesy of Dr.J.W.C.de Vries.

and are expected to perform at operational temperatures up to 150°C. The alloy SnAg3.5Cu0.9, with a melting point of 217°C, is determined to be truly eutectic. Other commonly used near-eutectic compositions are SnAg3.0Cu0.5 (used mainly in Japan), SnAg3.5Cu0.7, SnAg3.8Cu0.7 (recommended by European IDEALS consortium) and SnAg3.9Cu0.6 (recommended by the US NEMI consortium).

1.2 Objective

SnAgCu attracted attention in the past decade as a valuable alternative solder alloy in replacement of SnPb. Being a fairly new alloy, there was a certain lack of knowledge in its material properties, mechanical behavior, solder/substrate interactions, thermomechanical fatigue life, fatigue life predictability, etc. This thesis aims to scientifically contribute to each of these items.

The objectives of this thesis are as follows:

- Microstructural examination of SnAgCu and solder/substrate interactions for a variety of metallizations.
- Determining mechanical properties of SnAgCu and related intermetallic compounds by nano-indentation.
- Characterizing the SnAgCu/NiAu bond/pad interface under cyclic mechanical loading, establishing a thermomechanical damage evolution model for the bond/pad interface by simulating local deformations leading to fatigue crack propagation by separation of interfaces.
- Characterizing the SnAgCu bulk material under thermal cycling, investigating corresponding fatigue damage paths in correlation with the microstructure and local crystallographic orientations, and establishing a thermal fatigue damage evolution model for bulk SnAgCu by microstructural modeling.

- Developing a package size computational tool for solder joint reliability including microstructure, local crystallography and initial defects.
- Further predictions on solder joint reliability regarding solder geometry and solder size (miniaturization).

1.3 Outline of thesis

Chapter 1 gives a brief introduction on lead-free solders in ball grid array packages and solder fatigue.

In Chapter 2, microstructural observations on SnAgCu solder and solder/substrate interaction are presented. Nano-indentation is used to determine the mechanical properties of SnAgCu. The exploitation of the nano-indentation technique for soft metals like solders is discussed.

Chapter 3 focuses on fatigue damage characterization of the bump/pad interface by inverse modeling. A combined experimental-numerical study on the cyclic mechanical response of SnAgCu/Ni-Au interface is conducted. Fatigue experiments are simulated reproducing the stress state in the specimen, from which the parameters of a cohesive zone based fatigue damage model are identified.

Chapter 4 exploits the same methods developed in Chapter 3 further, in order to investigate thermal fatigue in bulk SnAgCu. Here, bulk SnAgCu samples are thermally cycled, followed by mechanical testing to evaluate the fatigue damage. Test samples are modeled including the original microstructure on the basis of which the experiments are simulated. Reproducing the experimental results, parameters of a cohesive zone based fatigue damage model are identified.

In Chapter 5, the numerical tools used so far are extended to 3D. The damage laws identified are combined and integrated in a 3D solder interconnect model. Many models are created using experimental input such as different microstructures and initial defects, enabling statistical analysis. Fatigue life of these models are predicted and the results are validated using industrial failure distribution charts.

In Chapter 6, the solder ball model developed so far is extended in order to predict the effect of solder ball size and geometry, in other words miniaturization, on interconnect reliability on the basis of numerical analyses.

The conclusions drawn from the current study are presented in Chapter 7.

CHAPTER TWO

Microstructural Analysis of SnAgCu[1]

Abstract

In solder joint reliability, the solder/pad interface plays a vital role, the quality of which is determined by the metallization. In this paper, microstructural analyses of SnAgCu alloy and soldered joints are conducted in connection with the metallization. Solder balls, solder paste and cast SnAgCu are reflowed on Cu, Ni/Au and Cu/Ni(V)/Au substrates. The influence of the selected substrate on bulk and interfacial metallurgy, and the preferential crack propagation under tensile and shear loading is examined. It is seen that microstructural entities, i.e. intermetallic layers and primary crystals, strongly influence the crack path. Void formation is a common problem in BGA production, since voids degrade the mechanical properties of the solder joint. In order to increase the joint quality, different laser reflow parameters are investigated, and an optimum procedure is established. Nano-indentation and tensile testing is used for the mechanical characterization of SnAgCu. The elastic modulus of SnAgCu is found to increase with increasing Ag content for the considered alloys. Noticing the strong influence of indentation depth, sequential loading and peak hold time on the results obtained by nano-indentation, an assessment on these indentation parameters for solders is conducted.

[1] *Reproduced in part from:* M. Erinç, P.J.G. Schreurs, G.Q. Zhang, M.G.D. Geers, (2005). Microstructural Damage Analysis of SnAgCu Solder Joints and an Assessment on Indentation Procedures. *Journal of Materials Science: Materials in Electronics*, **16**, 93–100.

2.1 Introduction

Efforts in decreasing component dimensions led to the development of ball grid arrays (BGAs) and flip chips replacing lead-frame packages. SnAgCu is by now the most widely accepted Pb-free replacement for SnPb solder in microelectronics industry, due to its microstructural stability and improved creep-fatigue resistance [1, 2]. BGAs can contain more than 1000 in/out terminals with solder balls of 300-760 μm in diameter. In flip-chips, galvanic deposition techniques allow for solder diameters of as small as 35 μm. The pads on both the chip side and the printed circuit board (PCB) side contain thin films of lamellar metallic layers, the so-called under bump metallization (UBM), which serves as a passivation and diffusion barrier layer, as shown in Figure 2.1. Selection of an appropriate solder/UBM combination determines the long-term joint reliability since failure often occurs along these layers. Important characteristics of the metallization are the structure of the intermetallic compounds (IMCs), their morphology and thickness, mechanical properties of individual layers, adhesion between IMC layers and solder, microstructural evolution after multiple reflows and diffusion properties [3, 4]. Studies on the intermetallic compounds in SnAgCu during reflow and in the solid state can be found in [5–8].

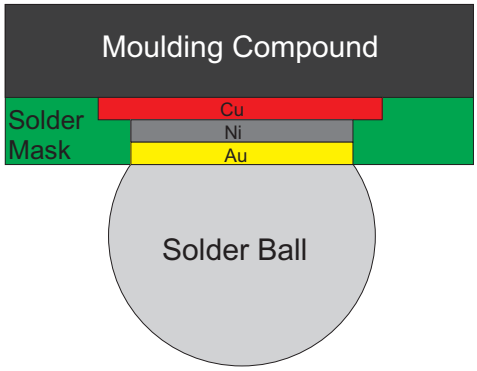

Figure 2.1: Under bump metallization.

For Sn-rich solders, nickel based UBMs, Ni(P)/Cu, Ni(P)/Au, Ni(V)/Cu, Ni(V)/Al, etc. are commonly used. A 10-15 μm thick Ni film serves as a diffusion barrier between the Cu pad and the solder, and slows down the reaction kinetics of formation of Cu_6Sn_5 [9, 10]. Phosphorus addition ($\sim$9wt%) decreases the high internal stress induced by electroless nickel deposition. With a different purpose, addition of vanadium decreases the magnetism of nickel and speeds up the fabrication. Vanadium as an impurity in nickel is also reported to lower the Ni(V)/Cu_6Sn_5 interfacial energy and thereby prevents spalling into the solder [11]. Above the nickel layer, a 300 nm - 1 μm thick Au, Cu, Al or Sn film is deposited for passivation. Details of the interfacial reaction of SnAgCu on electroless Ni(P)/Au UBM are given in [12]. During reflow, Ni(P) crystallizes to Ni_3P and Ni_3Sn_4, among which Ni_3P is a brittle phase. A Ni(V)/Cu UBM is shown to be unstable with SnAgCu due to the spalling of inter-

metallic compounds after 20 reflows [13]. When Au is used as a passivation layer, it diffuses rapidly in SnAgCu during reflow. It is reported that the precipitation of $AuSn_4$, being a brittle phase, might take place in the solder after reflow [14].

In the literature, lead-free solder joint reliability is generally approached in a statistical manner, for which failure distribution charts are reported as typically used by the industry. In order to reveal the underlying damage mechanisms and understand the role of metallization on crack propagation, a more fundamental approach is required. Hence, the current study focuses on a detailed analysis of the morphology of the bulk, and interfacial structures of SnAgCu reflowed on Cu, Ni/Au and Ni(V)/Au substrates, in order to establish a correlation between the interfacial microstructure and corresponding crack paths. The data collected in this study will be used later in a microstructure incorporated solder joint simulation to predict the fatigue life of the joint. The material properties that will be used in such a simulation are here collected using the nano-indentation technique.

There have been several research initiatives towards determining material properties of solders and related intermetallic compounds by nano-indentation [15–19]. Motivated by the large scatter in the reported results, an assessment of indentation procedures for solders is conducted. Operating parameters such as indentation depth, sequential loading and peak hold time have a strong influence on the results obtained by nano-indentation.

Void formation is a common problem in BGA production, since voids degrade the mechanical properties of the solder joint. In order to increase the joint quality, different laser reflow parameters are investigated, and an optimum procedure is established.

2.2 Experimental Procedure

The following experimental set-ups have been made to address the present questions at hand:

1. SnAgCu solder balls (0.3-0.76 mm in diameter) from different manufacturers and a cast SnAgCu sample were supplied. The composition of the alloys varied between 3.5-4.0 Ag and 0.5-0.7 Cu. The initial microstructure of the solder balls, and the cast alloy is investigated after standard metallographical preparation.

2. Sn3.8Ag0.7Cu solder paste is reflowed on commercial purity copper, representing a non-UBM case. For better wetting, the cross-sections to be soldered were polished. Specimens shown in Figure 2.2 were soldered at 260°C on a hot plate and air cooled, and mounted to a computer controlled tensile stage. Specimens were flat and symmetric in order to minimize non-planar forces and bending moments. The load applied corresponded to a strain of 0.3-1% with a strain rate of 10^{-4}. This strain range is concurrent with BGA flexure measurements [20–22].

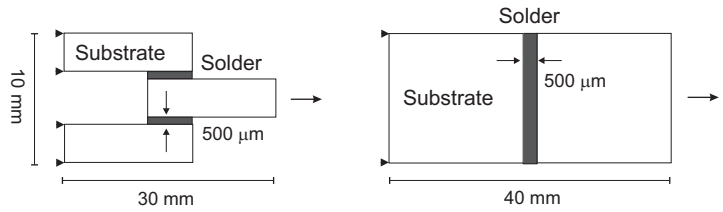

Figure 2.2: Shear and tensile test specimens.

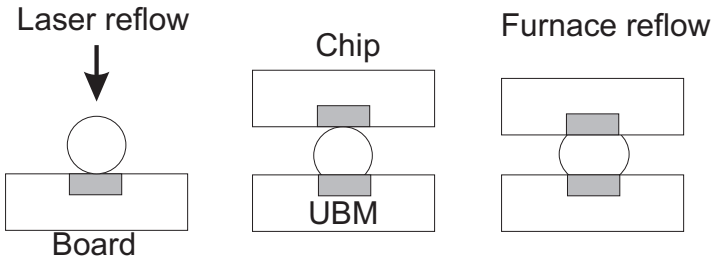

Figure 2.3: Production of single solder ball joints using 760 μm diameter solder balls.

3. Sn3.8Ag0.7Cu solder paste is reflowed on 99.8% pure nickel, coated with a 0.5-0.8 μm thick Au layer by ion sputtering, representing a commercial Ni/Au metallization. Soldering conditions and the load applied were similar to the previous case.

4. The bonding interface in a commercial BGA package (WT1T1-BGA256) with Sn4.0Ag0.5Cu solder balls was investigated by sampling randomly from the production line. The metallization on the FR4 board consisted of Cu (17 μm), Ni(V)(10$\pm$2 μm), and Au finish (1$\pm$0.1μm).

5. Sandwich specimens as shown in Figure 2.3 were produced by laser reflowing on the board side, followed by furnace reflowing at 260°C on the chip side. For the laser reflow, an MBL-500 type Solder Ball Bumper was employed, which was optically pumping a 200 μm diameter Nd:YAG-laser beam. The solder alloy used was Sn4.0Ag0.5Cu.

The microstructural examinations were conducted using an E-SEM and EDX elemental mapping. Nano-indentation experiments were conducted with an MTS nano-indenter using a Berkovich tip. In data analysis, the Oliver&Pharr elastic contact analysis method was used [23].

2.3 Results & Discussion

2.3.1 Microstructure

The results of the case studies explained in the previous section are summarized below.

Case 1

The microstructures of solder balls with slight differences in the chemical composition, appear to be distinct. The main differences are the morphology and quantity of β-Sn dendrites. Since these solder balls originate from different manufacturers, it can be concluded that the production and cooling rate differences have a big impact on the final microstructure.

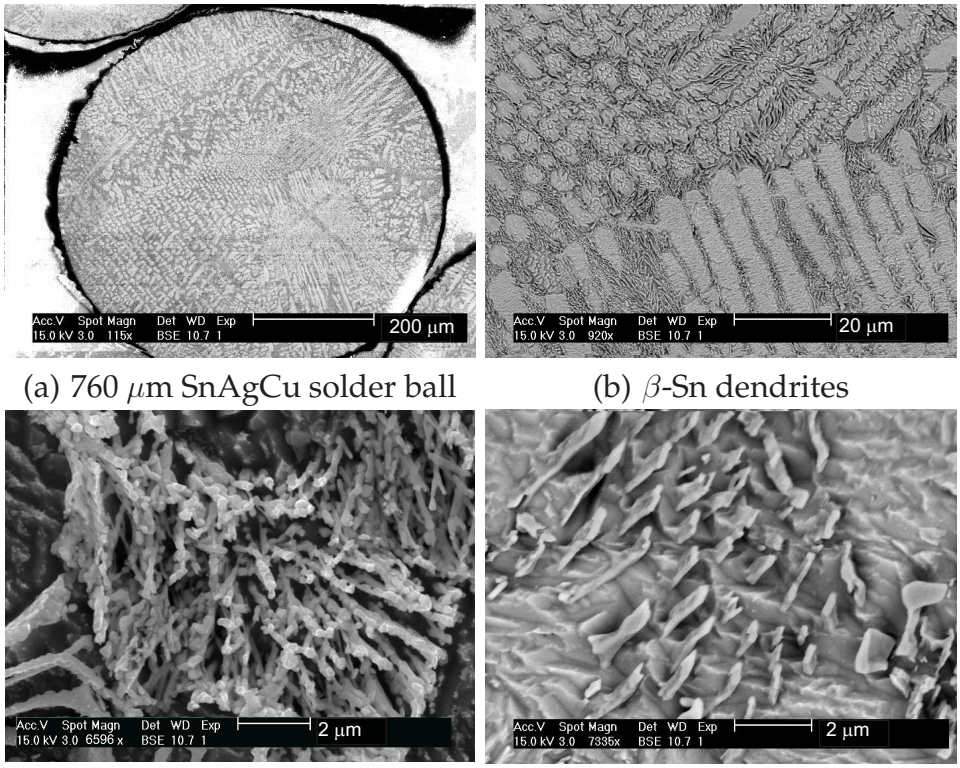

(a) 760 μm SnAgCu solder ball (b) β-Sn dendrites

(c) Ternary eutectic Cu_6Sn_5 (d) Ternary eutectic Ag_3Sn

Figure 2.4: SnAgCu microstructure at different scales.

The microstructure of SnAgCu solder balls at different scales are shown in Figure 2.4. Although the composition is near-eutectic, probably due to rapid cooling the structure is highly dendritic. Between the β-Sn dendrites, the ternary eutectic matrix resides. Matrix is composed of fine particles of Ag_3Sn and Cu_6Sn_5 in β-Sn matrix. The

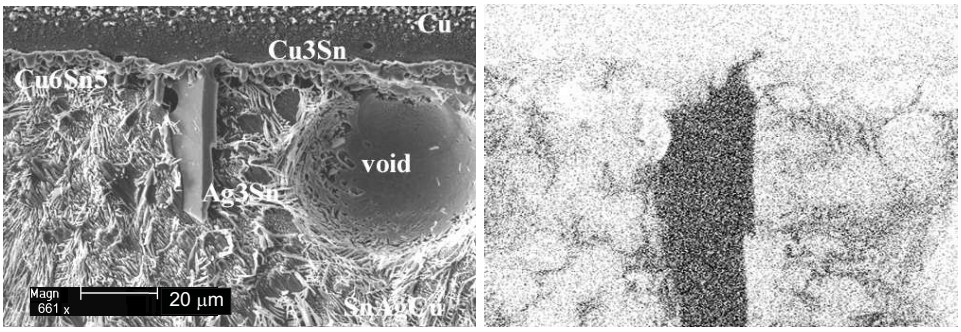

Figure 2.5: Copper-SnAgCu bonding interface. E-SEM image (left), Ag L elemental mapping (right).

dimensions of Ag_3Sn strips are measured as 300-600 nm in width and 2.5-3.5 μm in length. Cu_6Sn_5 rods are the smallest constituents, they are approximately 500 nm in diameter and 1-2 μm in length.

Case 2

The interfacial structure formed after reflowing SnAgCu on Cu substrate is shown in Figure 2.5. At the bonding interface two layers of intermetallic compounds form, Cu_3Sn and Cu_6Sn_5. Cu_3Sn has a typical thin layer morphology, however Cu_6Sn_5 grows into the solder and forms a structure known as scallop morphology.

During soldering copper diffuses rapidly into the solder and precipitates as primary Cu_6Sn_5 crystals during solidification. These crystals may have different morphologies as shown in Figure 2.6. Primary Cu_6Sn_5 crystals have a relatively big size in the microstructure, being brittle with sharp edges. Therefore, excessive copper diffusion into the solder should be prohibited by diffusion barriers, such as nickel metallization.

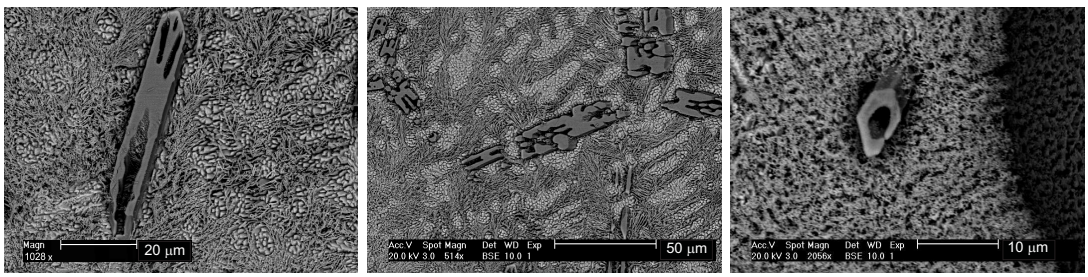

(a) Hexagon (b) Blocky (c) Hollow tube

Figure 2.6: Primary crystals in SnAgCu after reflowing on Cu substrate.

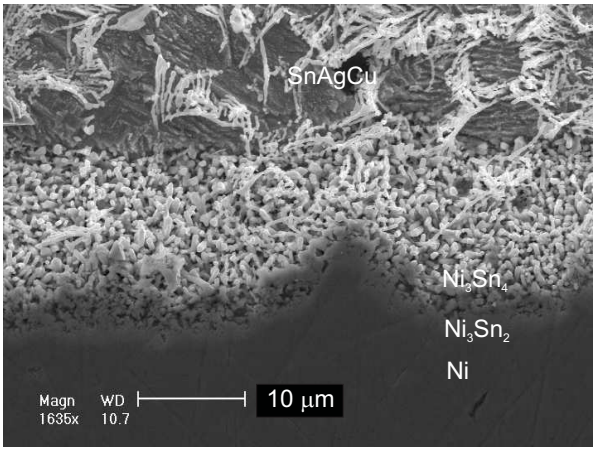

Figure 2.7: Ni/Au-SnAgCu bonding interface.

Case 3

The Ni/Au-SnAgCu interface is shown in Figure 2.7. During reflow, two transition intermetallic layers form between Ni and SnAgCu, i.e. a 2.5-6.4 μm thick Ni_3Sn_2 layer and a 2-3.75 μm thick Ni_3Sn_4 layer. The morphology is similar to a Cu/SnAgCu interface, even tough Ni_3Sn_4 scallops are narrower and have a rough lateral surface compared to Cu_6Sn_5. It can be expected that narrow scallops provide a larger surface area for Ni diffusion into the solder. Near the bonding interface, primary crystals of Ni_3Sn_4 precipitate. Some of these crystals have a well-defined morphology, i.e. dipyramids, though some are idiomorphic. Since Ni acts as a diffusion barrier between Cu and the solder, large Cu-Sn crystals do not appear in the matrix, even tough some Cu already present in the solder still precipitates as shown in Figure 2.8.

After reflow, no Au was detectable at the bonding interface. The high diffusion rate of Au in Sn [3], together with hot-plate reflowing allows Au to diffuse longer distances without segregation. Little Au (1-3%wt) was detected in the solid solution and in the intermetallic compounds.

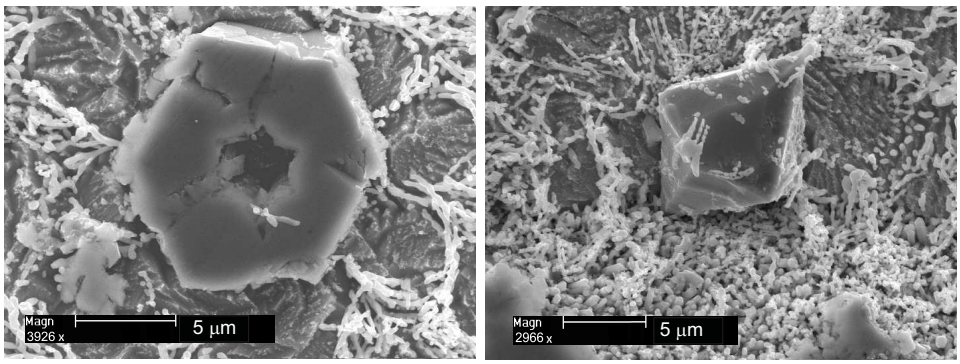

(a) $(Cu,Ni)_6Sn_5$ hollow tube (b) Ni_3Sn_4 pyramid

Figure 2.8: Primary crystals in SnAgCu after reflowing on Ni substrate.

Case 4

The interfacial structure of SnAgCu solder balls on Cu/Ni(V)/Au UBM is examined by cross-sectioning BGA packages. Before ball placement, the initial Au thickness on the metallization was measured as $\sim$1 μm by elemental mapping. The observed microstructures at the bonding interface are shown in Figure 2.9. Different plate-like morphologies of $(Cu,Ni)_6Sn_5$ were detected. At some instances the eutectic structure of $AuSn_4$-Au was also observed. Au was also detected in the solid solution. This suggests that, either the Au layer was too thick at some spots, or the reflow temperature was not high enough to promote Au diffusion.

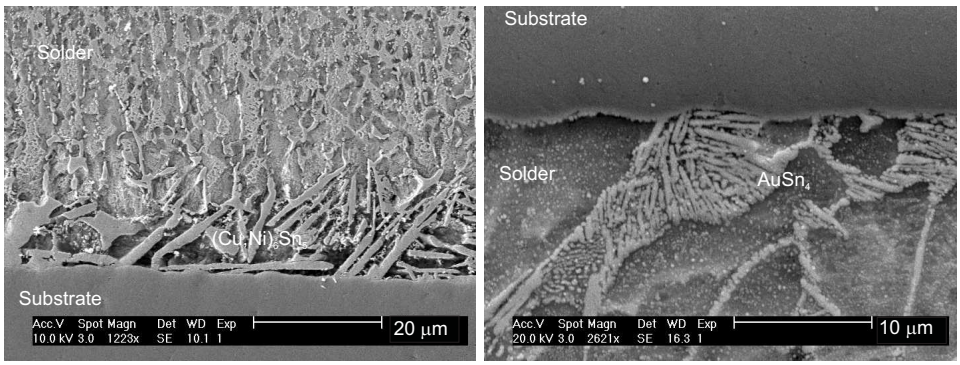

(a) $(Cu,Ni)_6Sn_5$ formation (b) $AuSn_4$-Au eutectic formation

Figure 2.9: Structures observed at SnAgCu-Cu/Ni(V)/Au interface.

Case 5

Several defective structures were encountered in the BGA solder balls. The most common defects were interfacial voids. Interfacial voids, or blowholes, are analyzed in detail in Chapter 5. A second class of defects was large intermetallic compounds, which grew from the interface into the solder. An example is shown in Figure 2.10a, where an Ag_3Sn plate is seen in its cross-section, thus the longest dimension of the plate is out of plane. The third class of defects consists of over-reflow voids in the solder bulk, especially at the inter-dendritic regions, shown in Figure 2.10b.

The reflow time has to be long enough to melt the solder and grow intermetallic compounds at the adjoining interface that will join two substrates. On the other

Table 2.1: Laser solder reflow parameters.

Current [A]	Time [ms]	Energy [mJ]	Interface	Bulk
60	9	520	voids	ok
60	10	570	ok	ok
60	11	630	ok	voids

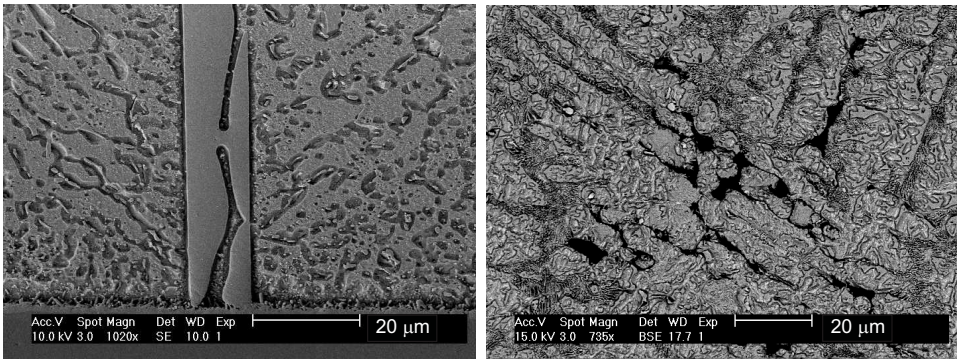

(a) A large Ag_3Sn crystal (b) Over-flow voids

Figure 2.10: Faulty structures in BGA solder balls.

hand, prolonged reflow time promotes excessive diffusion from the metallization into the solder and causes oversized intermetallic compounds. Furthermore, partial melting between dendrites initiates voids. The latter happens because the melting temperature of the eutectic matrix is lower than the β-Sn dendrites, which is the pro-eutectic phase. To investigate these problems, solder balls were reflowed using three different laser exposure times, and the resulting structures were compared. The reflow parameters and results are tabulated in Table 2.1. After 9 ms exposure, a significant amount of voids were observed at the bonding interface. Laser exposure was apparently not enough to release the reflow gases. After 10 ms, a continuous intermetallic layer was observed at the interface without any morphological change in the bulk. At 11 ms, partial melting in the solder was observed.

2.3.2 Mode I and Mode II failure

Preferential crack propagation under tensile and shear loading in connection with the microstructure is examined. Specimens shown in Figure 2.2 were loaded under monotonic shear and tension. The stress-strain curves for the tested specimens are shown in Figure 2.11. The strain value is calculated from the distance between the clamps, representing a global value. For both types of substrates (Ni/Au and Cu), the soldered joints are stronger in shear loading than tensile loading. For both types of loading, solder joints with Cu substrate perform better.

Figure 2.12 shows the damaged zones under shear (a) and tensile (b) loading at the Cu/SnAgCu bonding interface. In shear loading, smeared cracks (100-200 nm spacing) in the intermetallic layer along with decohesion of the intermetallic layer from the substrate leads to failure. Under tensile loading, overall failure occurs due to the decohesion of the solder from the intermetallic layer. Apart from the bonding interface, grain boundaries and dendrite arm tips in the solder were also damaged.

Damaged zones under tensile (a) and shear (b) loading at the Ni/Au-SnAgCu interface are shown in Figure 2.13. Unlike the Cu substrate, a good adhesion between the intermetallic layers and SnAgCu here exists. Under tensile loading, the intermetallic

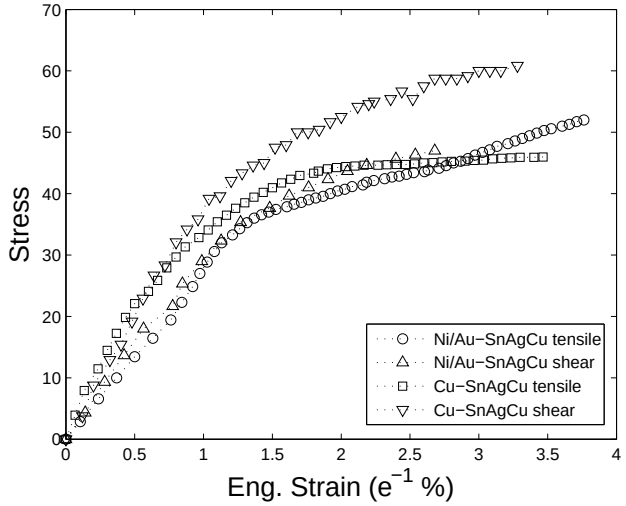

Figure 2.11: Engineering stress-strain curves for soldered joints with Ni/Au and Cu substrate.

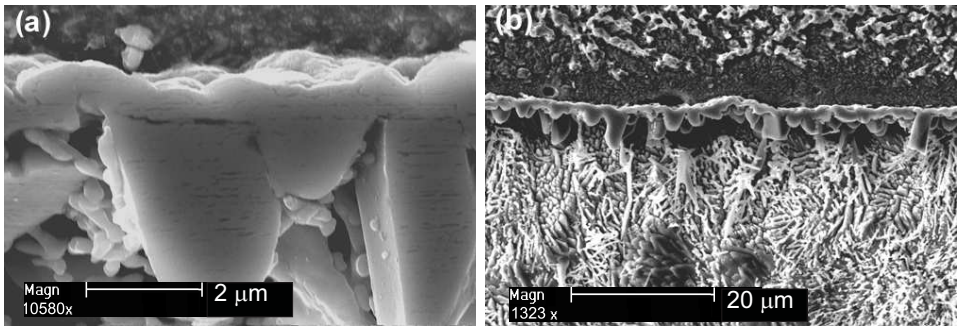

Figure 2.12: Cu-SnAgCu (a) Smeared cracks in Cu_6Sn_5 under shear loading, (b) Delamination of solder under tensile loading.

layers fail first. Under shear loading, the crack path is located between the solder and the intermetallic layer. Delamination of primary intermetallic crystals from the surrounding solder is also observed.

The failure mechanisms discussed above can be used to explain the results of mechanical tests shown in Figure 2.11. The intermetallic layer at the bonding interface has a characteristic irregular morphology, i.e. scallops. Apparently this layer provides a mechanical barrier to shear loading.

Inspired by the results reported above, a descriptive failure mechanism for a solder/substrate bonding interface is proposed. Dominant crack paths under tensile and shear loading can be represented in a normal and tangential separation scheme, as shown in Figure 2.14. Later, these results are used to develop a solder joint reliability model, using constitutive laws for the normal and tangential tractions as typically implemented in cohesive zones.

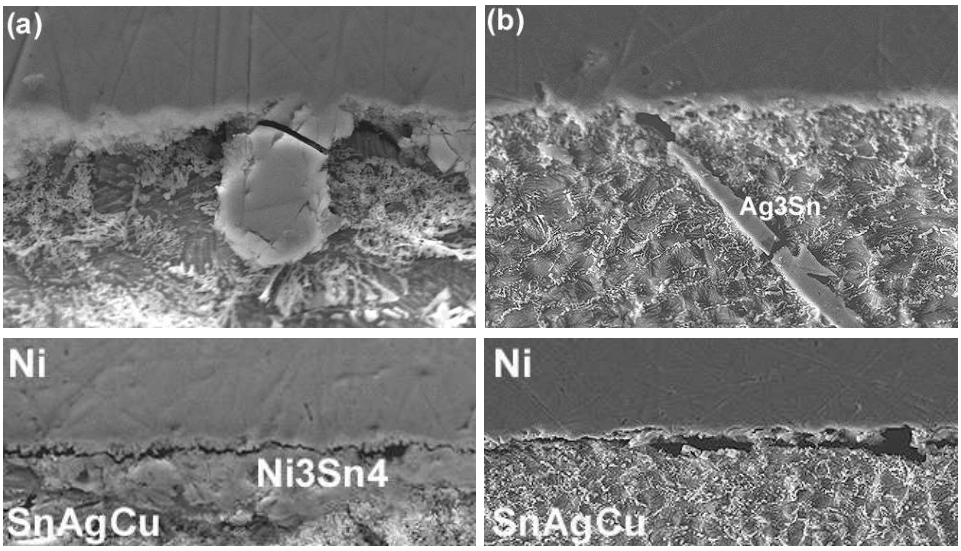

Figure 2.13: Ni/Au-SnAgCu (a) Brittle cracking in the intermetallic under tensile loading, (b) Crack propagation at the bonding interface under shear loading.

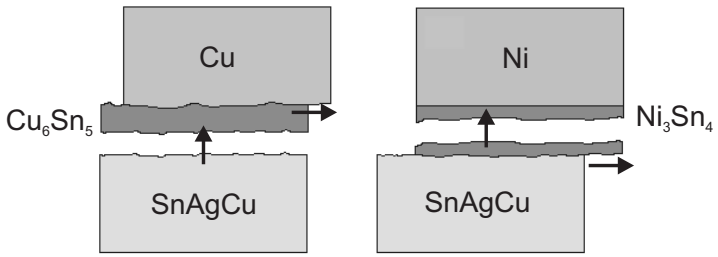

Figure 2.14: Crack path scheme under normal and tangential tractions.

A single solder ball specimen is shear loaded until failure. Fracture surfaces are examined by E-SEM, as shown in Figure 2.15. The fracture surface shows a mixture of brittle and ductile failure. The circumference of the solder ball indicates brittle fracture (region A). Towards the middle (region C), parabolic dimples are observed implicating a highly ductile fracture. Between these two fracture regimes, fluting occurs (B). Along the loading axis, the last region to fail (region D) is heavily deformed.

2.3.3 Micro-mechanical properties

Nano-indentation is a well-established method for collecting micro-mechanical material properties for a variety of materials. The indenter is forced into the specimen surface, then it is withdrawn. From the unloading force-displacement data, elastic properties are calculated (Oliver and Pharr method [23]), provided that the materials Poisson's ratio is known.

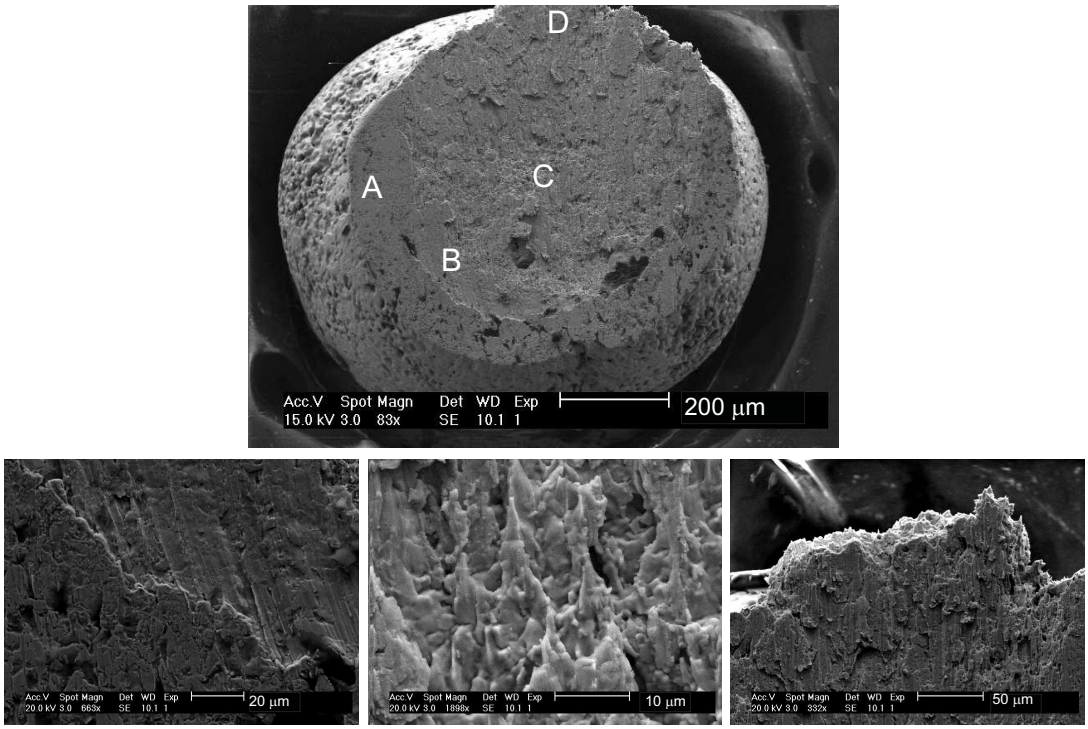

(a) Region B, fluting (b) Region C, dimples (c) Region D, heavy deformation

Figure 2.15: Shear fracture surfaces of a SnAgCu solder ball.

As reported in [23], displacements recovered during the first unloading stage may not be entirely elastic, and the use of a holding time at the peak load before unloading diminishes time dependent effects. To investigate this phenomenon for solders, a 1 mm thick plate of cast SnAgCu alloy is metallographically prepared for indentation. Between the successive indents, a 100 μm distance is left. As shown in Figure 2.16, four loading schemes are applied:

i) max 5 mN, 1 loading step

ii) max 20 mN, 1 loading step

iii) max 5 mN, 3 loading steps

iv) max 20 mN, 3 loading steps

The results are shown in Figure 2.17. Calculated elastic moduli decrease about 15-25% with successive load steps, being more pronounced by increased indentation depth. Since room temperature corresponds to a homologous temperature T_h=0.6 for SnAgCu, the internal elasto-visco-plastic mechanisms are operative during the test. Therefore, testing time should be minimized, whereas high strain rates should be avoided as well. Indentation depths of more than 2 μm causes excessive plastic deformation on the surface (pile-up). The effect of the peak hold time is investigated

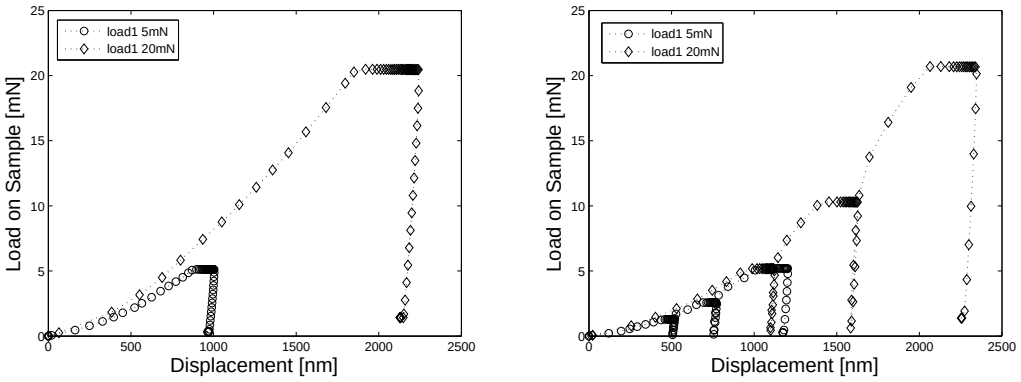

Figure 2.16: Single (left) and multiple (right) loading schemes, with peak loads 5 mN and 20 mN.

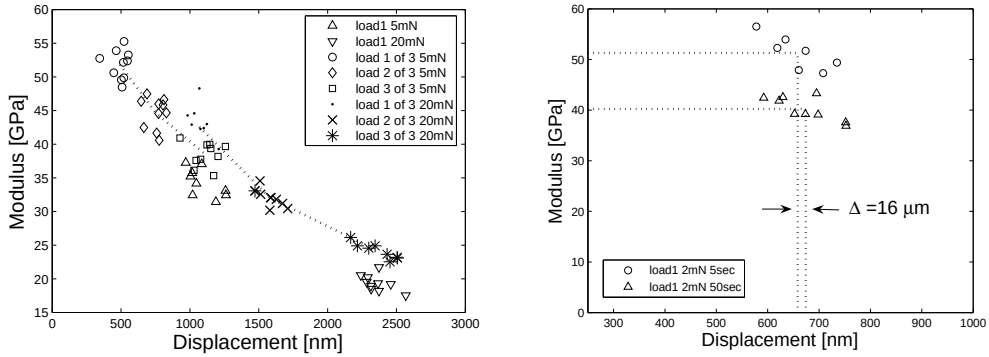

Figure 2.17: Elastic modulus w.r.t. the displacement into the surface and loading sequences (left), and peak hold time (right).

by holding a 2 mN peak load for 5 and 50 seconds. The average elastic modulus decreases 22% by increasing the peak hold time. The results show a slight displacement during the constant load regime indicating time-dependent mechanisms.

It can be concluded that, for soft solders, i.e. SnAgCu, multiple loading and prolonged peak load interfere adversely with the intrinsic static mechanical properties. In the following indentation experiments, the indentation parameters are set as 2mN for the peak load and 5 sec for the peak hold time.

Indentation results of the intermetallic compounds Cu_6Sn_5 and Ag_3Sn, SnAgCu alloys with varying Ag content, copper and nickel are shown in Table 2.2. The measured elastic moduli of Cu and Ni are in good agreement with the literature. As the material gets stiffer, the spread in the results gets wider, even though the mean value closely represents the real material behavior. Increasing the Ag content in SnAgCu increases the stiffness for the tested compositions, whereas hardness is not affected. The increase in elastic modulus might be due to solid solution hardening effect of Ag in β-Sn.

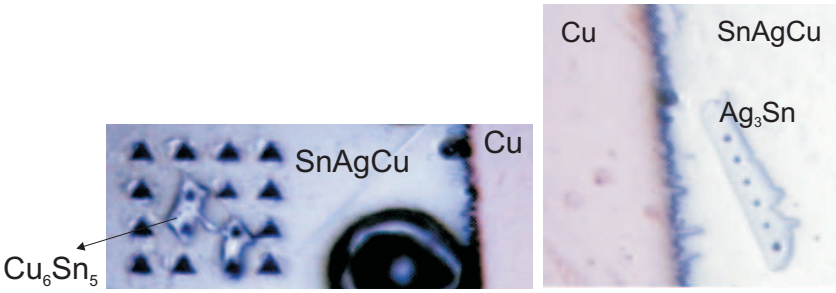

Figure 2.18: Indentations over intermetallic compounds Cu_6Sn_5 (left) and Ag_3Sn (right), 20× optical images.

Table 2.2: Results of nano-indentation tests.

	Young's modulus [GPa]	Hardness [GPa]	Poisson's ratio
Sn-4.0Ag-0.5Cu	64.1±2.0	0.21±0.02	0.35
Sn-3.8Ag-0.5Cu	57.9±3.4	0.21±0.02	0.35
Sn-3.5Ag-0.5Cu	51.3±4.0	0.21±0.06	0.35
Cu	128.7±10	1.23±0.07	0.34
Ni	197.0±8.9	3.83±0.2	0.35
Cu_6Sn_5	94.1±5.7	5.24±0.6	0.35[a]
Ag_3Sn	55.27±3.9	0.79±0.21	0.35[a]

[a] Lee et al. 2003

2.4 Conclusions

SnAgCu alloy has been investigated on the basis of interfacial structures it produces with Cu, Ni/Au and Cu/Ni(V)/Au substrates. Crack paths in solder joints under different types of loading conditions are investigated on the basis of the underlying microstructure, and a descriptive failure mechanism is presented. Nano-indentation method is employed to collect the elastic material properties of the materials discussed. For soft solders, several aspects of an indentation procedure are assessed. The following conclusions are drawn from the current study:

- As a surface finishing layer on Ni based metallizations, a Au film thickness of less than 1 μm dissolves completely in the solder. In BGA packages, at some spots, Au-$AuSn_4$ eutectic formation is observed.
- In BGA solder balls, Ag_3Sn growth and solidification voids are common problems. Soldered connections created by different laser reflow parameters are microstructurally examined, and an optimum procedure is established.
- Mode I and mode II crack propagation in SnAgCu soldered joints on Cu and Ni/Au substrates are investigated. The crack paths are closely connected to

the underlying microstructure. Therefore, continuum damage approaches are believed to be inadequate for solder joint reliability predictions.

- For soft metals (or alloys) like Sn based solders, a strong influence of indentation parameters on the measured material properties is observed. For SnAgCu solder, an indentation depth of more than 500nm, and sequential loading schemes cause an underestimate in the elastic material properties due to temperature effects. Prolonging the peak hold time evokes time-dependent internal mechanisms.
- The Ag content has a direct effect on the elastic modulus of SnAgCu alloys. For a 3.5-3.8 and 4.0 Ag content, the elastic modulus is found to increase with increasing Ag content. This phenomenon is believed to be due to the dispersion hardening effect of Ag_3Sn or solid solution hardening of (Ag).

CHAPTER THREE

Bump/pad interfacial fatigue fracture[1]

Abstract

In ball grid array (BGA) packages, solder balls are exposed to cyclic thermomechanical strains arising from the thermal mismatch between package components. Thermo-mechanical fatigue crack propagation in solder balls is almost always observed at the chip side of the bump/pad junction. The objective of the experimental part of this study is to characterize the bump/pad interface under fatigue loading. Fatigue specimens are prepared by reflowing Sn3.8Ag0.5Cu lead-free solder alloy on Ni/Au substrates. Obtained results show that fatigue damage evolution strongly depends on the microstructure. Applied strain and solder volume both have an influence on the fatigue damage mechanism. In the numerical part of the study, fatigue experiments are modeled using the finite element technique. A cohesive zone approach is used to predict the fatigue damage evolution in soldered connections. Crack propagation is simulated by an irreversible linear traction-separation cohesive zone law accompanied by a non-linear damage parameter. Cohesive zone elements are placed where failure is experimentally observed. Damage evolution parameters for normal and tangential interaction are scrutinized through dedicated fatigue tests in pure tensile and shear directions. The proposed cohesive zone model is quantitatively capable of describing fatigue failure in soldered joints, which can be further extended to a numerical life-time prediction tool in microelectronic packages.

[1] *Reproduced from*: M. Erinc, P.J.G. Schreurs, M.G.D. Geers (2007). Integrated numerical-experimental analysis of interfacial fatigue fracture in SnAgCu solder joints. *International Journal of Solids and Structures*, **44**, 5680–5694.

3.1 Introduction

Miniaturization trend in microelectronics has recently led to the development of ball grid array (BGA) and flip-chip packages. As size gets smaller, local operating temperatures increase, hence the package components are exposed to higher mechanical strains. In service use, thermal expansion coefficient mismatch between the package components leads to cyclic thermomechanical strains. In a microelectronic package, solder balls are prone to thermomechanical fatigue failure (Figure 1.2), which results in an open circuit and causes the electronic device to stop functioning. Another consequence of miniaturization is that in small parts mechanical properties become inhomogeneous due to size effects. It is previously reported that size effect causes microstructurally driven damage localization in lead-free solders [24]. Therefore, an in-depth study relating microstructure and fatigue damage evolution is crucial for the physical understanding of the thermomechanical fatigue problem in solder joints.

From July 2006 on, lead (Pb) containing parts are not used in microelectronic packages due to legislation. Among lead-free alternatives SnAgCu is a widely accepted lead-free replacement due to its better creep-fatigue resistance and microstructural stability. A broad review on lead-free solders in microelectronics is available in the literature [3]. Microstructural evolution in annealed cast SnAgCu alloy is reported in [1]. In their study, eutectic intermetallic components were found to coarsen, however the rate of reaction was significantly slower than in SnPb solder. On bond pads, Ni/Au is the most widely used surface finish. Interfacial structure between SnAgCu and Ni/Au metallization has been extensively studied [6, 14, 25–27]. Solders are exposed to high homologous temperatures in service, therefore, in microstructural and mechanical characterization, evaluation of time-dependent properties becomes crucial. Time dependent material behavior of SnAgCu in connection with microstructure is studied in detail [28–31]. A review on solder joint fatigue models is given in [32]. However, experimental validation of these models at the level of a single solder interconnect is hardly existing in the literature. A chip size experimental and numerical study of SnPb solder fatigue fracture is carried out in [33].

Fatigue life predictions for solder joints are generally carried out by using a Coffin-Manson rule or a similar empirical relationship, where the solder material is treated as a homogenous continuum. Driven by miniaturization, solder joints have become so small that the size of microstructural entities in the solder is comparable to that of the joint itself. In order to predict fatigue failure at these size scales, rather than scale independent continuum-based approaches, local damage formulations in the solder joint are needed.

The objectives of this study are:

(i) to establish a link between microstructure and damage in lead-free solder joints under cyclic mechanical loading,

(ii) to characterize fatigue damage evolution at the bond/pad interface and

(iii) to simulate local deformations leading to fatigue crack propagation by separation of interfaces.

As motivated above, eutectic SnAgCu is here selected as the lead-free solder alloy of interest, and Ni/Au as the substrate in order to incorporate the full metallurgy at the bump/pad interface. In commercial packages, Ni is used as a diffusion barrier between Cu and solder, therefore Cu is not needed in the test specimens. It has been previously shown by the authors that the crack path between Ni/Au substrate and SnAgCu follows physical boundaries in the microstructure (interfaces) and the crack propagation can be split into normal and tangential components [26]. Such an interfacial failure scheme can be modeled effectively with a cohesive zone approach. In the cohesive zone formulation used in this study, normal and tangential tractions are decoupled. Therefore, two sets of experiments are set up; specimens that will induce pure tensile loading at the solder/metallization interface, and specimens that will induce pure shear loading at the solder/metallization interface. Later, tensile experiments are used to characterize the cohesive zone parameters for normal opening, and shear experiments are used to characterize the cohesive zone parameters for tangential opening.

Ni/Au-SnAgCu fatigue specimens are cyclically loaded with constant amplitude. Fatigue life is determined by the decrease in the reaction force. Experimental procedures and the results of fatigue tests are explained in Section 3.2 and Section 3.3, respectively. For every fatigue test sample, the stress-strain data as a function of number of cycles is plotted. Individual fatigue test samples are modeled using the finite element technique. Cohesive zone elements are placed at the regions where failure is observed. In Section 3.4, the cohesive zone model used in this study and the details of inverse parameter estimation is discussed. Last, in Section 3.5, a solder ball is modeled in 2D, and the fatigue life is predicted using the methodology discussed so far.

3.2 Experimental Procedure

First, mechanical properties of the materials that are going to be used in fatigue tests are measured. For this purpose, two half tensile parts are soldered with Sn3.8Ag0.5Cu. In order to be able to measure the Young's modulus for soft materials like solders, very small strains should be measured with high accuracy. Contact strain measuring techniques at these small scales may induce undesired effects, i.e. sliding of extenso-meter legs, holes for extenso-meter pins. For this reason, a non-contact optical strain mapping method is used. The specimen is first sprayed to create a fine distribution of black dots on white background. The tensile test is carried out in-situ under an optical microscope and high resolution digital images are acquired periodically by a digital camera. These images are then uploaded to strain mapping software [34] where local strains are calculated by masking the substrate. The soldered joint was 200 μm thick and 10 mm long. Since image acquisition

time is known in advance, the images captured are synchronized with the force-time recording and thereby a stress-strain curve is obtained. For SnAgCu, Young's modulus and yield stress is measured as 51 GPa and 25.24 MPa, respectively. Initial yield stress is taken as the engineering stress at 0.2% strain offset. The stress-strain curve for Sn3.8Ag0.5Cu is shown in Figure 3.1; the associated hardening rule is determined from the experimental data points.

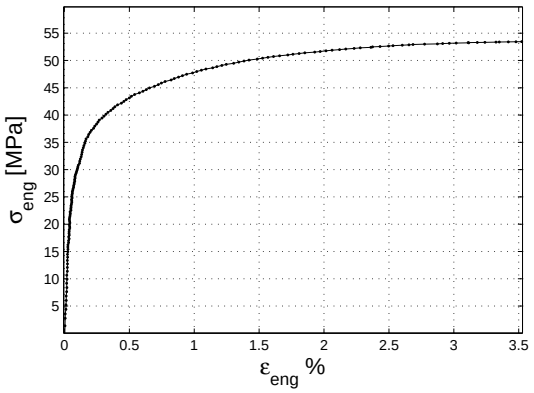

Figure 3.1: Stress-strain curve for Sn3.8Ag0.5Cu.

Two sets of fatigue experiments, being pure tensile and pure shear are set up. The specimen geometries are shown in Figure 3.2. First, Ni substrates are machined from 1 mm thick 99.98% purity nickel plates by wire-erosion using an electro-discharge machine (EDM). Except for the external faces to be soldered, machined parts are teflon-coated in order to prevent excessive wetting of the solder on nickel. Next, the surface to be soldered is Au coated by ion sputtering to a thickness of 0.5-0.8 μm, which represents a typical printed circuit board (PCB) bump pad. Ni/Au substrates are soldered by Sn3.8Ag0.5Cu solder flux on a hot plate at 250°C and air cooled. Metallographic surface preparation is applied on both sides of the sample. All specimens were 5 cm in the longest axis and $<$1 mm in thickness (due to grinding). For the tensile specimens, four different geometries are considered; the gage width, shown with an arrow in Figure 3.2a, is taken as 10, 5, 3 and 1 mm. Two 10 mm, six 5 mm, eight 3 mm and eight 1 mm specimens are produced. For the double joint shear specimens, two different geometries are considered: the gage width is taken as 3 and 1 mm (Figure 3.2b). Three specimens for each double joint geometry is produced. For the single joint shear specimens, nine 3 mm gage specimens are produced (Figure 3.2c). Polished samples are first examined under polarized light, where grains and solder dimensions are measured. The solder thickness varied between 500$\pm$200 μm. On average, the solder volume in 10, 5, 3 and 1 mm tensile samples was approximately 4, 2, 2 and 0.4 mm^3, respectively. The 3 mm double joint shear specimens contained 1.2 mm^3, and 1 mm contained 0.4 mm^3 solder. Single joint shear specimens contained 1.2 mm^3 solder.

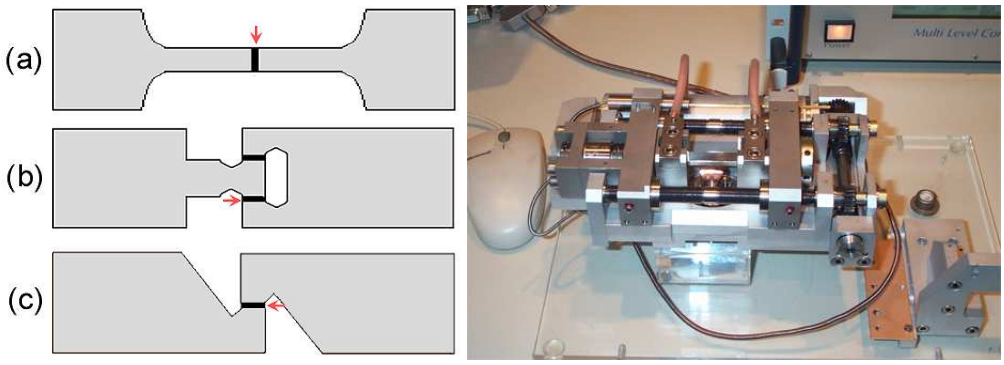

Figure 3.2: Sn3.8Ag0.5Cu-Ni/Au soldered joints of shape: (a) Tensile, (b) Double joint shear, (c) Single joint shear (left). Double spindle micro-tensile stage (right).

Fatigue tests were conducted in a computer controlled double spindle micro-tensile stage where reaction force and elongation were recorded. An external extenso-meter and a 500 N load cell was used. Clamp speed was set to 1-2 μm/s depending on experimental convenience. Triangular cyclic elongation was prescribed. Tests took place at constant room temperature. The solder joint was considered as failed when the recorded reaction force dropped to half of the maximum stress attained in the first cycle, and the corresponding number of cycles is referred as the solder joint's strain life (half life criterion) [35]. Applied strain varied in the range -1%–3.5%.

3.3 Results of fatigue tests

Figure 3.3 shows the local strain field distribution in a soldered joint under tensile loading at various global strain values. SnAgCu solder is situated in the middle and on the left and right is the Ni/Au substrate. Strain fields are monitored throughout the deforming region until 1% strain level is reached. Strain is distributed homogeneously at the start of experiment, up to a threshold value of $\sim$0.04%. After 0.04% global strain, local strain fields at the bonding interfaces are observed to be higher than the strain in the bulk solder, indicating damage localization. With further increase in global strain, a fairly homogeneous strain distribution is seen in the solder. At 0.5% global strain, local strain in the solder corresponds to 4%, which is well in the plastic region. At later stages, crack propagation is observed at the interfacial regions having the highest local strain values. Post-mortem analysis showed that regions near the solder interface were heavily deformed. Figure 3.4 shows an $(Cu,Ni)_6Sn_5$ intermetallic compound that has delaminated from the solder matrix and cracked, thereby triggered secondary cracks to initiate in its surroundings. Intermetallic compounds form during reflow and they act as stress concentration points due to their sharp edges. Furthermore, they are more brittle than the matrix (Hardness $H_{Cu_6Sn_5}$ = 3.7 GPa, H_{SnAgCu} = 0.83 GPa [16]).

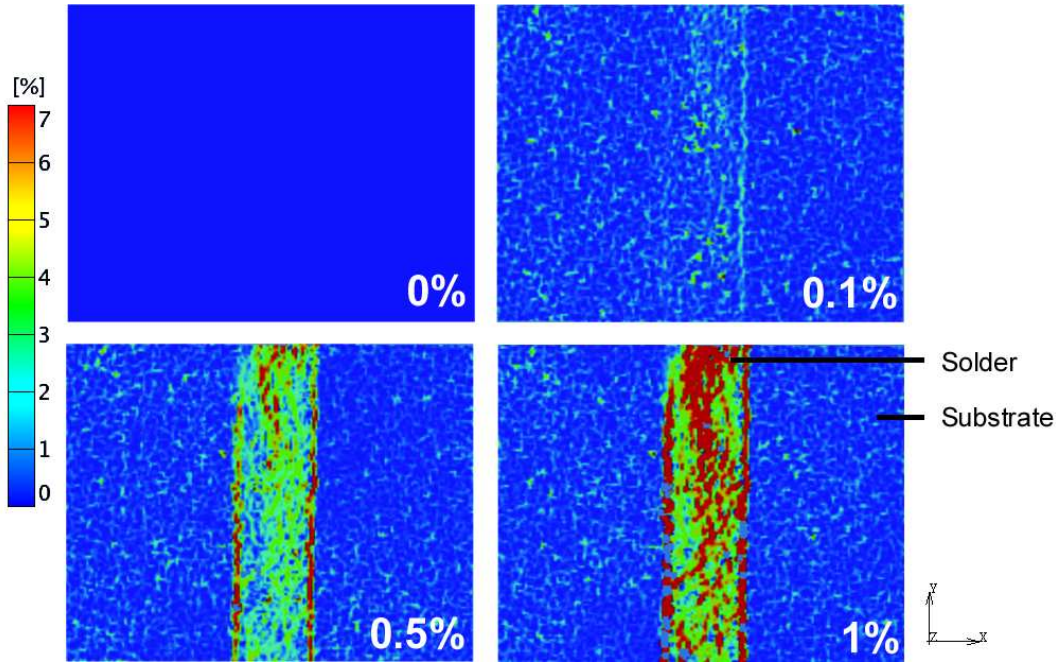

Figure 3.3: Local strain field distribution in Ni/Au-SnAgCu-Ni/Au solder joint having global strain values ε_{xx}=0%, 0.1%, 0.5% and 1%.

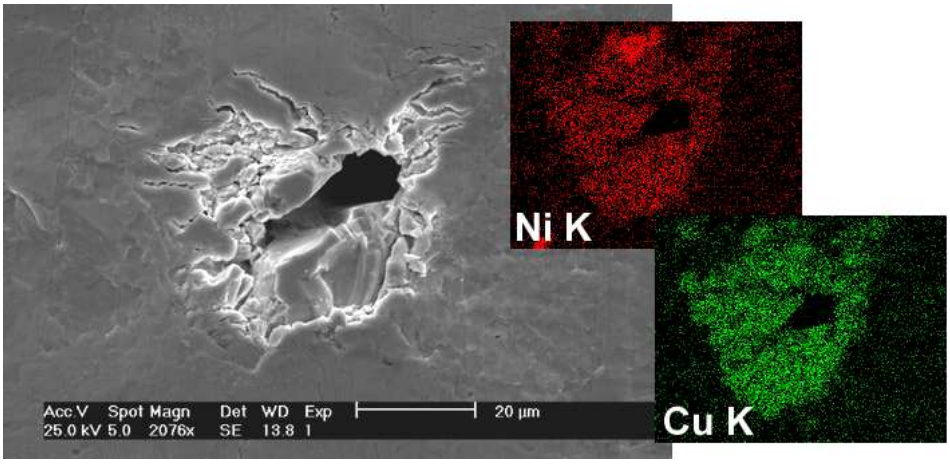

Figure 3.4: Upon tensile loading, $(Cu,Ni)_6Sn_5$ intermetallic compound has cracked into pieces and initiated secondary cracks in the surrounding solder matrix.

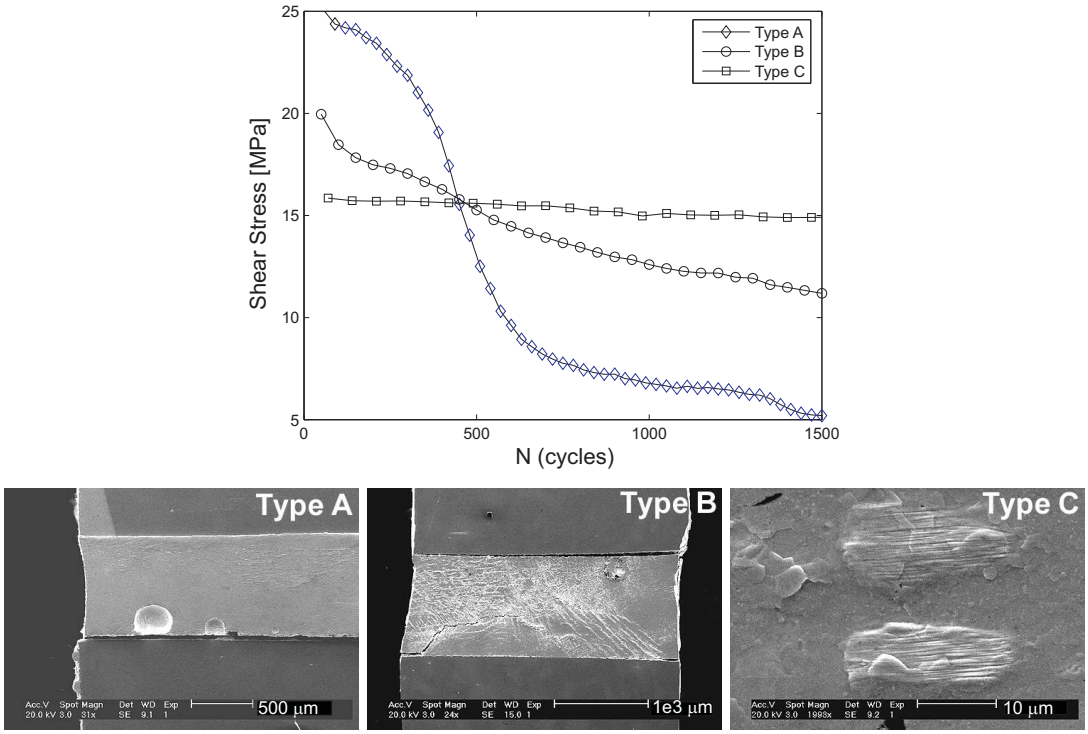

Figure 3.5: Stress drop regimes observed in cyclic strain controlled experiments and typical micrographs corresponding to A, B and C failure types.

3.3.1 Failure Types

In this study, fatigue failure is defined as the number of cycles when the reaction force has dropped to half of the initial value. If the sample did not fail before N=1e4 cycles, the test was stopped due to time limitations. For every fatigue specimen, stress vs. number of cycles is plotted (Figure 3.5). Results can be categorized in one of the three following schemes: a delamination regime (type A), an infinite life regime (type C), and in between type A and C, a gradual failure regime (type B). Microstructural observations suggest that there are two different failure mechanisms operative:

(i) heterogeneous matrix deformation, and

(ii) localization of deformation at the bonding interface.

Type A failure can be examined in three stages: (1) incubation period in the beginning where stress reached at peak strain is steady, (2) fatigue failure stage where stress at peak strain decreases steeply and (3) the last stage where stress decreases gradually as a result of crack bridging and friction. Fractographs show highly localized damage at the bonding interface since the major crack propagates on the interface and there is almost no matrix deformation. If there are blowholes in the solder, main

crack preferentially propagates on that weaker interface. Here the dominating failure mechanism is delamination. Strain life is between N=1000-2000 cycles. Type A failure is observed in the fatigue specimens in which the initial stress was highest. In addition, solder volume being less than $\sim$1 mm^3 seemed to increase the tendency towards delamination.

An infinite fatigue life (type C) is observed when the initial stress was less than 17 MPa, and/or when solder volume exceeded 3 mm^3. This suggests that strain life of SnAgCu solder joints is not only determined by the initial stress state but also depends on geometry. In the solder matrix many small cracks are observed. The pattern of these cracks coincides with the pattern observed in the polarized images taken before the fatigue tests. For the present case, it can be concluded that fatigue cracks initiate on domain boundaries where there is a slight difference in the crystallographic orientation. Another interesting point was that slip lines appeared in β-Sn dendrite arms but not in the eutectic matrix, most probably due to the hard intermetallic particles in the ternary eutectic matrix. In type C specimens, a major fatigue crack was still not observed after N=1e4 cycles. These results suggest that a fatigue limit exists in both normal and tangential directions of the bonding interface, with a roughly estimated value of σ_f=17 MPa. In order to verify the fatigue limit, a separate testing procedure is necessary.

Specimens in which fatigue failure proceeds gradually are referred as type B. Fractographs show heavy deformation in the matrix as well as an interfacial crack which has led to failure. Surface relief in the solder matrix consists of slip in β-Sn dendrites, many short cracks on domain boundaries in the eutectic matrix, deformation bands 45° in the loading direction, and secondary cracks on grain boundaries. Strain life is between N=2000-5000 cycles. Here, both deformation mechanisms mentioned above are operative.

Whether the fracture behavior will be abrupt (by delamination) or gradual depends on local soldering conditions. Existence of manufacturing defects on the surface, under wetting, insufficient intermetallic growth will favor delamination leading to a sudden failure. If the fatigue crack propagation is taking place in the solder very close to the bump/pad, dimples and fatigue striations are observed in the fractographs and the expected failure type is gradual.

Shear specimens show more matrix deformation than tensile specimens. This suggests that the interfacial region is weaker in the normal direction than in the tangential direction. In the tangential direction, the scallop geometry of intermetallic compounds serve as a mechanical barrier and solder cannot delaminate easily. Therefore, energy dissipation due to plastic deformation in the matrix is promoted over damage localization at the bonding interface. This observation is in accordance with the results shown in Section 2.3.2.

3.3.2 Size Effect

Results of the fatigue tests are classified according to specimen size and geometry. Strain life versus applied strain for four different types of tensile specimens, i.e. gage width being 10, 5, 3 and 1 mm, are shown in Figure 3.6 a. Indicated strain values are corrected for the elongation in the substrate and thus correspond to the actual strain in the solder. For the shear specimens, strain life versus initial shear stress is plotted in Figure 3.6 b for three different types of shear specimens indicated in the figure. Comparison is made on the basis of both applied strain and initial stress. Applied strain is directly related to the fatigue life, however, during specimen preparation (grinding and polishing), sample thickness decreases differently for different samples and comparison with respect to stress takes into account the difference in cross-section.

It is clearly seen that there is a size driven trend in the fatigue lives of both tensile and shear specimens. As the gage width decreases, fatigue life under the same initial stress also decreases. Apparently, a smaller solder volume increases the tendency towards localized deformations at the bonding interfaces. Interestingly, 1 mm gage tensile specimens do not follow this pattern; strain life of 1 mm specimens is higher than 3 mm specimens. This can be explained in the following way: the probability of having casting defects in a smaller volume is less than the probability of having a defect in a bigger volume. Since fatigue cracks initiate at the surface or at defects, 1 mm tensile specimens have a smaller surface area and apparently contain less defects. To summarize, for SnAgCu-Ni/Au soldered joints, smaller joints are weaker than bigger joints until 0.4 mm^3 solder volume. Our results agree with previous studies on solder joints [36] and confirm that mechanical properties of soldered joints are size dependent.

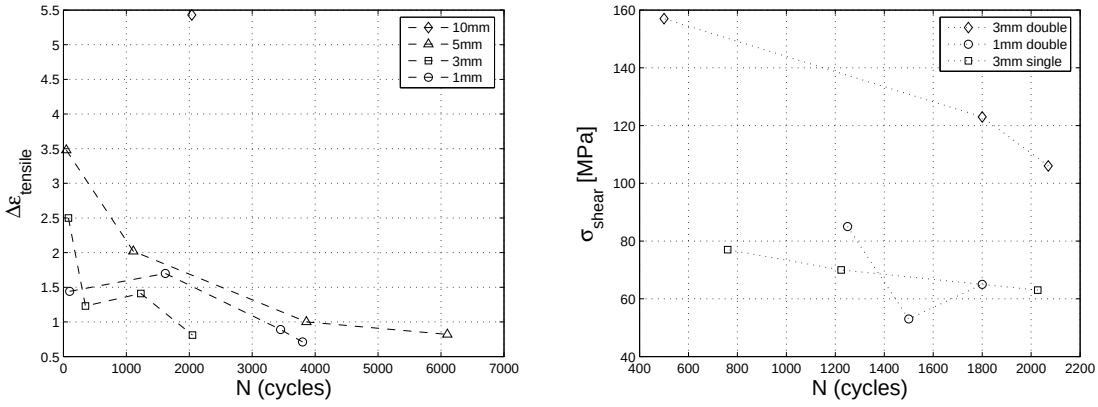

Figure 3.6: Strain life versus strain on solder (top) and strain life versus initial stress (bottom), for tensile and shear specimens.

3.3.3 Fractography

It was possible to examine the fracture surfaces in cases where fatigue samples fell apart in two pieces. Some examples of fatigue fracture surfaces between SnAgCu and Ni/Au are shown in Figure 3.7. In Figure 3.7a, b and c ductile fracture patterns are seen. Dimples and striations are clearly visible. On the substrate side of the fracture surface, Ni_3Sn_4 scallops are seen. This suggests that delamination starts from scallop tips and the fatigue crack propagates by coalescence of these voids. In some instances, the solder has completely delaminated from the substrate. In delaminated samples, only the interfacial intermetallic compounds were visible on the substrate side (Figure 3.7d).

The reaction force against number of cycles for a 3 mm tensile specimen is plotted in Figure 3.8a. As fatigue deformation initiates, the upper part of the F-N plot approaches the x-axis as a result of damage evolution and crack growth. However, the lower part of the curve also approaches the x-axis where it is expected to remain constant. Figure 3.8b shows the lateral cross-section of the specimen where the solder moved out of the sample plane. Apparently, as a result of crack propagation, material continuity is lost and grains are free to move out of plane. Since the in-plane material volume decreases by this movement, the external force required to displace the material back to its original position also decreases.

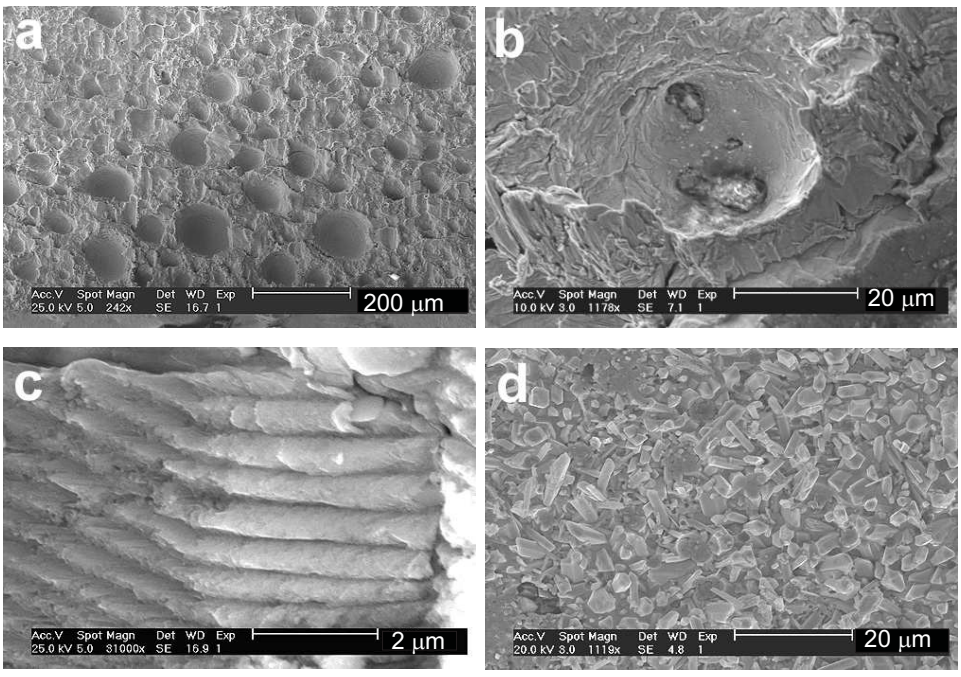

Figure 3.7: Fatigue fracture surfaces at the bonding interface: (a) dimples on solder side, (b) corresponding dimples on substrate side, (c) fatigue striations, (d) delamination surface on substrate side.

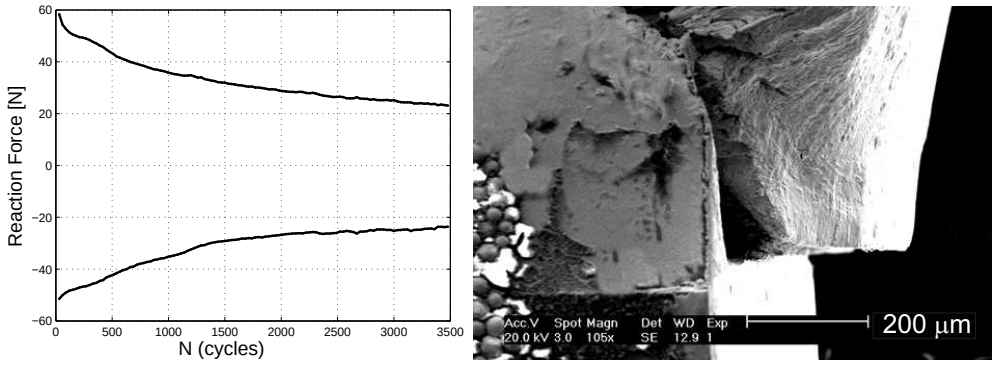

Figure 3.8: (a) F-N plot of a 3 mm tensile specimen, (b) lateral view of the specimen after N=3500 cycles.

3.4 Cohesive Zone Model (CZM)

Cohesive zones were developed to model crack initiation and propagation as the separation between two surfaces resisted by cohesive tractions [37–39]. Static cohesive zone models are extended to model interfacial failure under cyclic loading [40], whereas other models have been proposed on the basis of the incorporation of a damage parameter [41]. Based on previous formulations [42], an irreversible damage model for interface fatigue crack growth for solder joints is described [43]. A damage variable D is introduced in the model which evolves from the undamaged state D=0, until complete failure D=1. As damage increases, the apparent stiffness k(1-D) in:

$$\mathrm{T}_\alpha = \mathrm{k}_\alpha(1-\mathrm{D}_\alpha)\Delta_\alpha \quad \text{, where} \quad \alpha = \mathrm{n,t} \tag{3.1}$$

where k is the initial stiffness, diminishes until no traction is needed for separation. Damage evolution is determined by Eqn 3.2:

$$\dot{\mathrm{D}}_{\mathrm{n,t}} = \mathrm{c}_{\mathrm{n,t}}|\dot{\Delta}_{\mathrm{n,t}}|\left(1-\mathrm{D}_{\mathrm{n,t}}+\mathrm{r}_{\mathrm{n,t}}\right)^{\mathrm{m}_{\mathrm{n,t}}}\left\langle\frac{|\mathrm{T}_{\mathrm{n,t}}|}{1-\mathrm{D}_{\mathrm{n,t}}}-\sigma_{\mathrm{f}}\right\rangle \tag{3.2}$$

where $\dot{\Delta}_{\mathrm{n,t}}$ is the rate of relative opening, σ_{f} is the fatigue limit, c, m and r are constants that control damage evolution and thus the decay of the cohesive interaction. In the current study, the damage evolution parameters for the SnAgCu-Ni/Au interface are established by a coupled experimental-numerical analysis.

A schematic representation of a cohesive zone model is shown in Figure 3.9a, where two surfaces are attached by two perpendicular springs, which allows the two surfaces to be separated from each other in the tangential (t) and the normal (n) directions. Figure 3.9b shows the cohesive traction T as a function of opening displace-

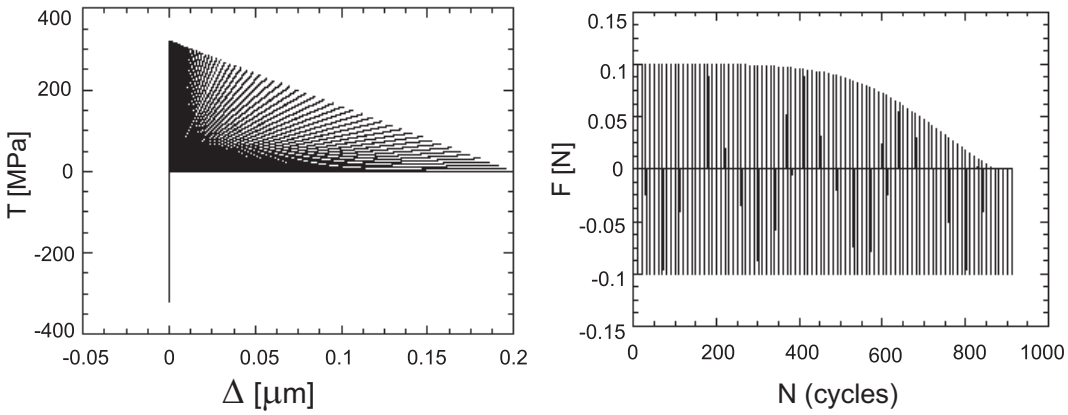

Figure 3.9: Constitutive behavior of the CZM.

ment Δ for various number of cycles. A cyclic sinusoidal displacement is applied to the upper nodes and the lower nodes are restricted. As maximum opening displacement increases, maximum traction decreases as a result of damage evolution via cyclic loading. The cohesive zone formulation is implemented in the commercial finite element package MSC.Marc/Mentat as a user defined element in 2D which can be used both in plane strain and in plane stress to describe the interfacial interaction.

3.4.1 Characterization of CZM

As confirmed by the present fatigue experiments, the bonding interface is prone to thermomechanical fatigue failure. In order to simulate this failure mechanism, cohesive zone elements are placed at the intermetallic/solder interface. Since all physical interfaces have a very small, though a finite thickness, the interfacial zone is given 100 nm initial thickness (t_{cz}). In classical cohesive zone approaches, cohesive zones do not need to have an initial thickness. However, assigning a finite thickness allows one to calculate a finite initial stiffness which prevents the known initial stiffness problem and also describes the interphase [44]. Initial stiffness of the cohesive elements for normal (k_n) and tangential (k_t) directions are computed from the adjacent materials 1 and 2, in order to provide an equivalent elastic deformation initially with and without the cohesive elements. Initial stiffness for tangential and normal directions are given by:

$$k_t = \frac{2G_1G_2}{t_{cz}(G_1+G_2)} \quad , \quad k_n = \frac{2E_1E_2}{t_{cz}(E_1+E_2)} \tag{3.3}$$

where E is the Young's modulus and G is the shear modulus. Eqn 3.3 gives a harmonic mean type of relationship between the initial stiffness of the interface element with its neighbors, depending on the initial thickness of the cohesive element. When t_{cz} goes to zero, k_n and k_t go to infinity.

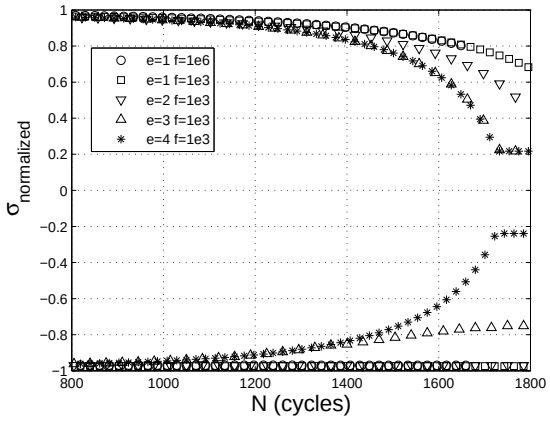

Figure 3.10: Effect of constants in the cohesive zone compression correction term.

As the numerical calculations were initiated, it appeared that two issues were not well addressed in the cohesive zone formulation. During the simulations of tensile specimens, cohesive zone elements start failing after a certain number of cycles which results in a mutual penetration of continuum elements. Second, as emphasized in Section 3.3, in the later stages of tensile fatigue tests, material continuity is lost and some solder grains are free to move out of the sample plane. To account for both issues, an additional correction term $\mathrm{f} * \mathrm{k_n} * |\Delta_\mathrm{n}|^\mathrm{e}$ is introduced in Eqn 3.4 to penalize material penetration:

$$\mathrm{T_n} = \begin{cases} \mathrm{k_n}(1-\mathrm{D_n})\Delta_\mathrm{n} - \mathrm{f} * \mathrm{k_n} * |\Delta_\mathrm{n}|^\mathrm{e} & \text{if} \quad \Delta_\mathrm{n} < 0 \\ \mathrm{k_n}(1-\mathrm{D_n})\Delta_\mathrm{n} & \text{if} \quad \Delta_\mathrm{n} \geq 0 \end{cases} \tag{3.4}$$

Compression penalty is controlled by the constant f. In plane material loss due to 3D movement is taken into account by the constant e. In the early stages of loading, the compression penalty dominates over the out of plane movement, and the cohesive zone is prohibited from penetrating into neighboring elements. As damage evolves, cohesive zones open up more, Δ_n increases and the out-of-plane movement starts to be significant. A number of calculations have been performed to see the effect of constants in the correction term, which are plotted in Figure 3.10. From both a numerical convenience point of view and to represent experimental results best, constants in the correction term are set as f=1e3 and e=3.7.

3.4.2 Parameter determination

Test specimens shown in Figure 3.2 are modeled using 2D plane stress elements. Fatigue experiments are simulated by prescribing the real experimental conditions

Table 3.1: Cohesive zone parameters for normal and tangential direction characterizing interfacial separation in a SnAgCu solder joint under cyclic loading.

Tensile experiments	Gage [mm]	ϵ^{peak} %	c_n [N/mm]	m_n	r
Exp. 11	5	2.0	68000	3.16	1e-6
Exp. 12	1	1.7	68000	3.16	3e-5
Exp. 13	3	1.4	68000	3.16	1e-6
Shear experiments	Gage [mm]	γ^{peak} %	c_t [N/mm]	m_t	r
Exp. 21	3	1.8	46000	3.14	4e-5
Exp. 22	3	2.9	48000	3.13	3e-6

at the specimen boundaries. Cohesive zone elements are placed between the intermetallic compound and solder, where fatigue failure is typically observed. In the simulations, damage evolution parameters are tuned to obtain the same global stress-strain response as measured in the experiments. By modeling the complete test-specimen, experimental stress-strain data is converted indirectly to the traction-displacement in the cohesive zones. A set of damage evolution parameters c, m and r in Eqn 3.2 is obtained which characterizes the strength of SnAgCu-Ni/Au bonding interface under cyclic strain. Among these, c is related to the damage initiation before any softening starts. The power parameter m takes values between 3 and 3.3, and is responsible from the sharpness of the softening. Parameter r takes values close to 0^+, and is the slope of the softening tail in the last stages of deformation. Smaller values of r predict a longer life time.

In the present model, damage evolution is activated only during loading, and inhibited during unloading in the cyclic load sequence. SnAgCu is modeled as indicated in Section 3.2, with Poisson's ratio ν=0.35. Young's modulus and Poisson's ratio of Ni is taken as 198 GPa and 0.31. Young's modulus of the intermetallic compound Ni_3Sn_4 is reported as 140.4 GPa [45], and Poisson's ratio is taken as ν=0.2. Substrate nickel and the intermetallic compound Ni_3Sn_4 are modeled linear elastically, since the stress state at the peak of the cycle is safely below the yield stress of both materials. Fatigue experiments were conducted at room temperature. SnAgCu is modeled by a time independent elasto-plastic material model combined with a steady-state creep model for bulk SnAgCu [30] shown in Eqn 3.5, where A_1 and A_2 are 4e-7 and 1e-12 s^{-1}, Q_1 and Q_2 are 26.8 and 61.4 kJ/mol, n_1 and n_2 are 3 and 12, respectively.

$$\dot{\varepsilon} = A_1 \left(\frac{\sigma}{\sigma_N}\right)^{n_1} \exp\left(-\frac{Q_1}{RT}\right) + A_2 \left(\frac{\sigma}{\sigma_N}\right)^{n_2} \exp\left(-\frac{Q_2}{RT}\right) \tag{3.5}$$

Blowholes are a common problem in soldering. A blowhole is a void at the bump/pad junction which decreases the cross-sectional area and therefore decreases the strength of the interface. For this reason, test specimens were examined in the presence of blowholes. In the numerical simulation of these specimens, initial damage in the corresponding cohesive zone elements is set to 1. Figure 3.11 shows the

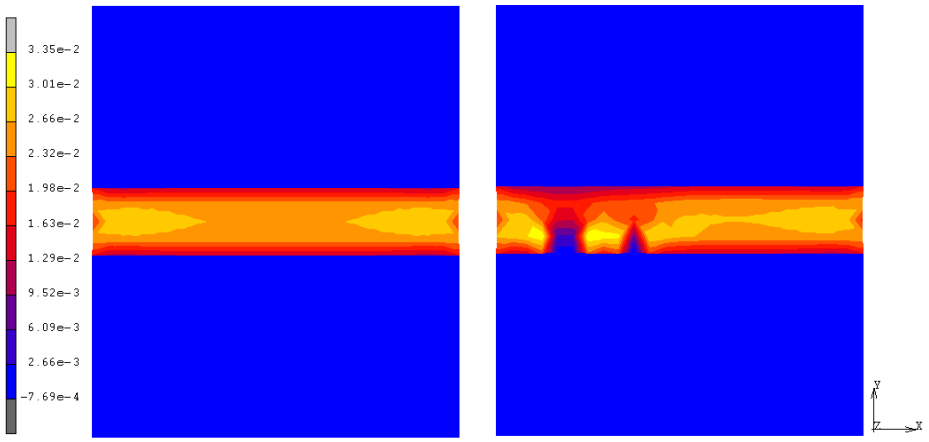

Figure 3.11: Simulation of specimen type A shown in Figure 3.5, local strain distribution in the loading direction ε_{yy}, with (right) and without (left) the blowholes.

total strain at peak load for two different simulations of the same specimen shown in Figure 3.5 - type A. In Figure 3.11a, blowholes are neglected and all interface elements have zero initial damage, whereas in b, two blowholes are placed exactly at the positions that they were observed. It is seen that inserting interfacial defects yields to more realistic results. In the rest of the simulations, observed blowholes are inserted to the mesh, and thereby the effect of a blowhole on the strength of the interface is incorporated into the model.

Figure 3.12 shows a number of experiments and the corresponding numerical simulations covering a variety of specimen geometries and applied strains. The model parameters used to predict the curves in Figure 3.12a are tabulated in Table 3.1. From the fitted parameters, c_n, c_t, m_n and m_t are reproducible. As previously discussed, the solder joint interface is stronger under shear loading than tensile loading, which is also apparent from the numerical results; c_n is 1/3 higher than c_t. Parameter r does not show a clear dependence on the loading direction being normal or tangential, however, it takes distinct values depending on the fracture behavior being gradual (type B) or abrupt (type A).

In summary, the strength of SnAgCu/NiAu interface under mechanical fatigue loading is measured and quantified via cohesive zone elements. The damage parameters are identified as c_n=68000, c_t=47000, m_n=3.16 and m_t=3.135. For parameter r, a range is identified, r_{grad}=1e-6 as the lower bound for gradual fracture and r_{del}=4e-5 as the upper bound for delamination. It is thereby suggested to use r_{grad} in standard life time predictions and r_{del} for safe design.

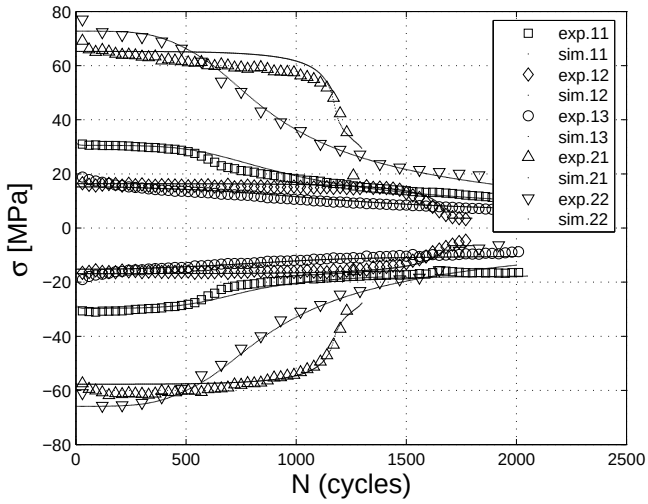

Figure 3.12: Comparison of experimental results and numerical calculations.

3.5 Application to SnAgCu solder interconnect

The cohesive zone parameters given above are used to simulate a solder bump having the dimensions 760 μm diameter, 500 μm height and 100 μm thickness in 2D plane stress. The solder material is SnAgCu, metallization is 20 μm copper pad and 10 μm nickel diffusion barrier. Between the metallization and solder, there is a 2 μm thick Ni_3Sn_4 intermetallic layer. Cohesive zone (cz) elements having a 100 nm initial thickness are placed between the solder and the intermetallic layer. Bottom nodes are constrained in both x and y directions, and the middle top node is loaded in cyclic shear. All material properties are the same as in the previous section. Copper is modeled linear elastically with the material parameters E=128 GPa and ν=0.35. The geometry of the solder bump and the prescribed loading is shown in Figure 3.13. Numerical analysis is carried out at 1% alternating cyclic strain for 5000 cycles. At each cohesive zone an effective damage value D_{eff} is calculated from the normal and tangential damage components according to the following relation:

$$D_{\text{eff}} = (D_{\text{t}}^2 + D_{\text{n}}^2 - D_{\text{t}}D_{\text{n}})^{\frac{1}{2}} \tag{3.6}$$

Contour plot of effective damage D_{eff} at the end of cycles N=0, 1000, 3000 and 5000 is shown in Figure 3.14. For visibility nodal values are linearly averaged in the contour plot. Thus, damage is made visible through the neighboring continuum elements, only for visualization purposes.

The solder ball geometry does not allow to simply justify a plane deformation state. The solder ball model is run with a plane stress and a plane strain assumption. Damage values for the plane stress case is higher than the plane strain case with the same

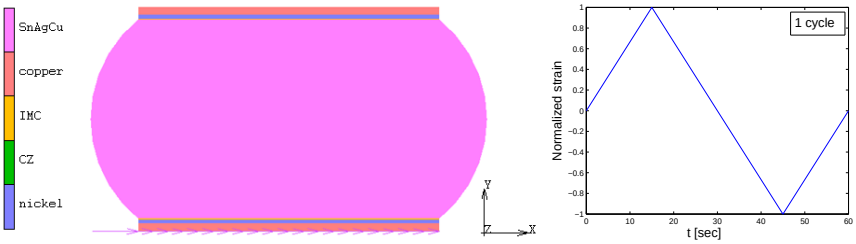

Figure 3.13: (a) 2D SnAgCu solder ball with Cu/Ni/Au metallization, (b) Prescribed loading on the top middle node ε_{xx}.

boundary and loading conditions. Thus plane stress assumption provides a lower bound for the fatigue life in the present study, which is preferential from an engineering perspective.

To summarize the discussion so far, an adequate agreement between experimental and numerical work has been established, whereby the cohesive zone approach is proven to be an effective tool in solder joint fatigue failure simulation. The model is numerically stable, and has the potential to be extended to chip size modeling and component life time predictions. The proposed model has the potential for blowholes to be included in the calculation, provided that adequate data on blowhole size and distribution specific to the manufacturing procedure is known in advance.

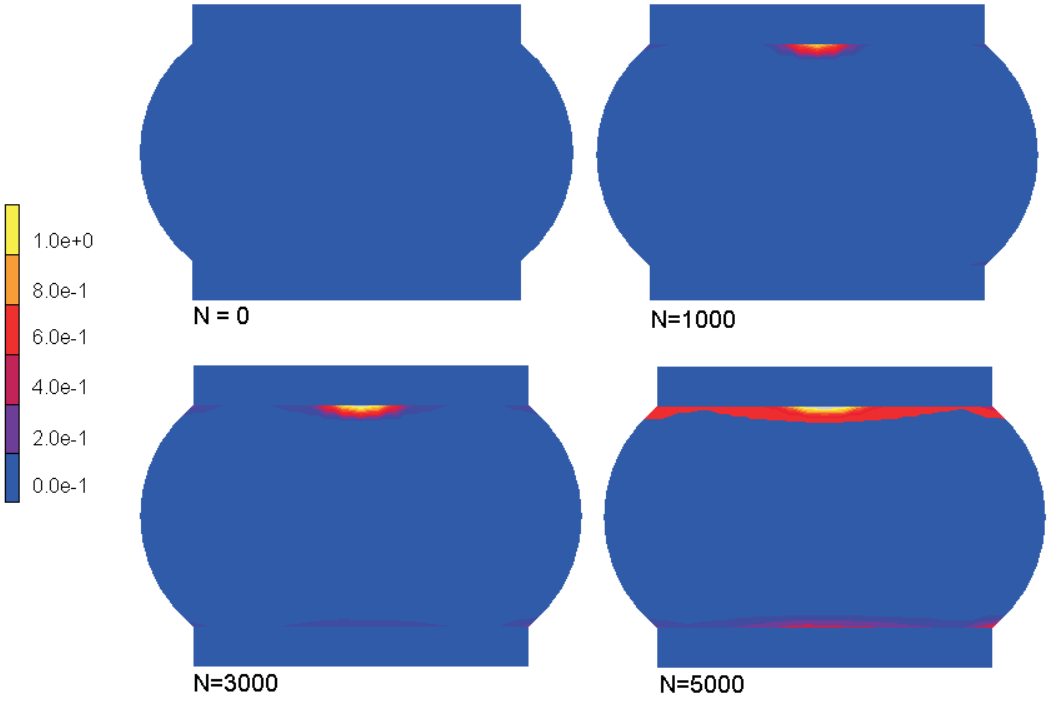

Figure 3.14: Effective damage (D_{eff}) in a SnAgCu solder bump after indicated number of cycles of shear strain.

3.6 Conclusions

A combined experimental-numerical study on solder joint fatigue failure is carried out. Ni/Au-SnAgCu solder joints are tested under cyclic shear and cyclic tension for different specimen geometries and strain amplitudes. From the qualitative and quantitative data obtained, interfacial separation due to fatigue damage evolution at the bump/pad interface is simulated using cohesive zone elements. The following conclusions are drawn from the present study:

- From the local strain fields observed in a soldered joint under tensile loading, strain localization is seen to be strongly microstructure dependent. Highest local strains are observed at the solder joint interface followed by grain boundaries.
- Two different microstructural failure mechanisms are observed; i.e. heterogeneous matrix deformation and localization of deformation at the bonding interface. The interfacial failure mode is typically favored at a high initial stress, and small solder volume.
- Strain life of soldered joints is size dependent.
- A strain life fatigue limit for the SnAgCu-Ni/Au bonding interface is observed.
- Cohesive zone material parameters for bump/pad fatigue crack propagation have been established for normal and tangential directions separately using different sample geometries and strain amplitudes.
- An adequate agreement between experimental and numerical work has been established, whereby the cohesive zone approach is proven to be an effective tool in solder joint fatigue failure simulation. The model is numerically stable, and has the potential to be extended to chip size modeling and component life time predictions.

At present, a mechanical model for cyclic mechanical loading has been established. This study is complemented in Chapter 4 by thermally cycled non-constrained solder specimens, in order to quantify the bulk damage in the solder due to thermal cycling. Both mechanical and thermal damage mechanisms is combined in Chapter 5 to predict thermomechanical damage in solder balls in a BGA assembly.

CHAPTER FOUR

Intergranular thermal fatigue damage[1]

Abstract

At present, SnAgCu appears to be the leading lead-free solder in the electronics industry. Driven by miniaturization, decreasing the component size leads to a stronger influence of microstructure on the mechanical properties. The present study concentrates on the thermal fatigue response of a near-eutectic SnAgCu solder alloy with the objective of correlating damage mechanisms with the underlying microstructure, on the basis of which a thermomechanical fatigue damage evolution model is characterized. Bulk Sn4Ag0.5Cu specimens are thermally cycled between -40 and 125°C up to 4000 cycles. The intrinsic thermal anisotropy of the β-Sn phase leads to localized deformations, especially along Sn grain boundaries. Mechanical degradation of test specimens after temperature cycling is identified from a reduction of the global elasticity modulus measured at very low strains. Using OIM scans, the test specimens are simulated including the local grain orientations and the detailed microstructure. A traction-separation based cohesive zone formulation with a damage variable that traces the fatigue history is used to simulate thermal cycling experiments. Damage evolution parameters are identified on the basis of the experimentally obtained global elastic moduli after a certain number of cycles. The resulting damage evolution law is applied to a number of numerical examples and the mismatch factor is discussed in detail. Finally, the damage evolution law characterized in this study is exploited towards the fatigue life prediction of a 2D microstructure-incorporated BGA solder ball.

[1] *Reproduced from*: M. Erinc, P.J.G. Schreurs, M.G.D. Geers (2007). Intergranular thermal fatigue damage evolution in SnAgCu lead-free solder. *Mechanics of Materials*, submitted.

4.1 Introduction

In microelectronic packages, solder joints are responsible for both the electrical and the mechanical connection between the printed circuit board (PCB) and the chip. During service, local operating temperatures increase and decrease repeatedly. Components of the package are exposed to thermomechanical strains arising from different coefficients of thermal expansion of the materials involved. Cyclic mechanical strains in the solder lead to thermomechanical fatigue crack initiation and propagation. As a result of legislation and technological requirements, microelectronics industry recently switched to eutectic SnAgCu solders as a replacement for the traditional SnPb solder. A broad review on solder materials, reliability issues and solder/substrate interactions can be found in the literature [3, 12, 46]. The reliability, failure and lifetime behavior of this solder alloy remains a subject of broad interest, since critical technology sectors (automotive, aerospace, etc.) are still exempted from using lead-free solders.

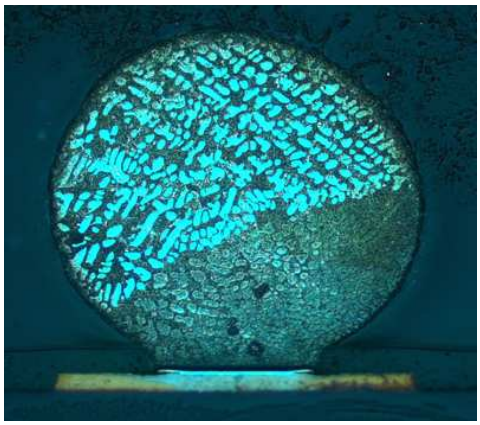

Figure 4.1: A 760 μm diameter SnAgCu BGA solder ball, polarized light image.

Thermomechanical fatigue failure in ball grid array (BGA) packages generally occurs at the bump/pad interface. In Chapter 3, a cohesive zone based interfacial separation model for the SnAgCu/Ni-Au (bump/pad) interface was developed. Apart from the bump/pad fatigue crack propagation in solder balls, Sn based solders are prone to thermal fatigue damage due to the intrinsic thermal anisotropy of the β-Sn phase. It has been well reported in the literature that thermal fatigue in Sn causes intergranular fatigue damage [47–51]. This issue is intrinsic to Sn-based solder balls due to their polycrystalline structure (Figure 4.1). Also, for packages where higher quantities of solder are used (i.e. QFN type packages), thermally induced intergranular fatigue failure becomes dominant over solder/pad interfacial fatigue failure [52]. In this context, a study on thermomechanical loading in Sn-Ag based lead-free solders with local grain orientations is given in [53]. Solders are exposed to high homologous temperatures in service use, and therefore their microstructural and mechan-

ical characterization requires an adequate evaluation of time-dependent properties. Studies on the time dependent material behavior of SnAgCu in connection with its microstructure can be found in [29–31].

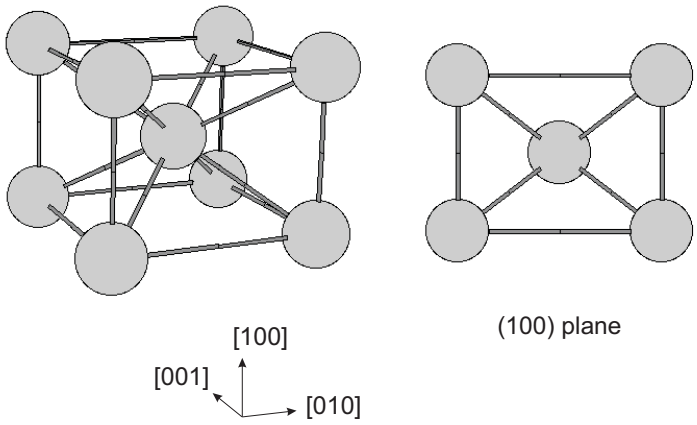

Figure 4.2: BCT lattice of β-Sn.

SnAgCu in its solid state consists of a β-Sn matrix and a fine dispersion of Cu_6Sn_5 and Ag_3Sn intermetallic compounds. The microstructure can be considered as a precipitation hardened (Sn) matrix. Pure Sn has an allotropic phase transformation at 13°C where diamond cubic α-Sn is the low temperature stable phase and β-Sn is the high temperature stable phase. β-Sn has a body-centered-tetragonal (BCT) lattice structure, with parameters a=b=583 pm and c=318 pm, with atomic positions (0 0 0), (0 1/2 1/4), (1/2 0 3/4) and (1/2 1/2 1/2), as shown in Figure 4.2. Direction [001] (side c) is almost half the length of the basal plane sides ([100] and [010]) which leads to anisotropic thermal properties. The thermal expansion coefficient α in the principal lattice directions are: α[100]=α[010]=16.5e-6°C^{-1} and α[001]=32.4e-6°C^{-1} [54]. This anisotropy is the main cause of intergranular fatigue damage evolution under thermal fatigue loading, which has been observed in thermal cycling over a range as small as 30-75°C [55]. α-Sn has a diamond cubic lattice which causes an increase in the volume by 27% upon transformation from β-Sn to α-Sn. It has been reported that small alloying additions of Sb, Bi or Pb suppress the transformation from β-Sn to α-Sn upon cooling [56]. In general, impurities in Sn are known to suppress this phase transformation. In this study, it seems reasonable to account for the thermal anisotropy of β-Sn, whereas the occurrence of the allotropic phase transformation is unlikely due to the presence of Ag and Cu in the β-Sn solid solution.

As motivated above, damage mechanisms in the bulk SnAgCu solder need to be identified for a proper thermomechanical fatigue analysis of Sn based solders. The objectives of this study are:

(i) to characterize SnAgCu bulk material under thermal cycling,

(ii) to investigate corresponding fatigue damage paths in correlation with the microstructure and

(iii) to characterize a damage evolution model using the quantitative data obtained.

The specimens, thermal cycling procedures and the experimental tools are explained in Section 4.2.1. The experimental results are presented in Section 4.2.2. It is shown that thermal fatigue damage localizes especially at high angle grain boundaries. Damage due to fatigue cracks is related to the global mechanical properties of the test samples. In Section 4.3, the experimental data is used to develop a damage model, which is solved with the finite element method. Fatigue crack propagation along grain boundaries leading to mechanical degradation in the solder bulk is predicted by a cohesive zone approach, where an interfacial damage variable is used to record the thermal fatigue history. Microstructural modeling of the test specimens is explained in Section 4.3.1. Damage evolution parameters in the cohesive zone model are identified on the basis of the experimentally obtained elastic moduli after a certain number of cycles. The exploitation of the model is discussed using a number of numerical examples.

4.2 Experimental

4.2.1 Experimental Procedure

Tensile specimens having the dimensions shown in Figure 4.3 are machined from a cast Sn4Ag0.5Cu slab. Six tensile specimens with thickness 1, 2 and 3 mm, 18 specimens in total, are metallographically prepared. Thermal cycling was performed in the standard testing range between -40 to 125°C. The ramp rate was 11°C/min and the duration of a cycle was approximately 1 hour. The temperature profile is shown in Figure 4.4. In the furnace chamber, specimens were allowed to expand and shrink without any mechanical constraints. One specimen of each thickness is removed from the furnace chamber after N=500, 1000, 1500, 2000, 3100 and 4000 cycles. No surface conditioning was applied to the samples after thermal cycling. The gage areas of the specimens were scanned with Orientation Imaging Microscopy (OIM) before and after thermal cycling. After N=1000 cycles, the surface roughness of the specimens exceeded the allowable limits for an OIM scan.

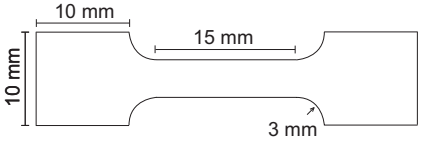

Figure 4.3: Sn4Ag0.5Cu tensile specimens.

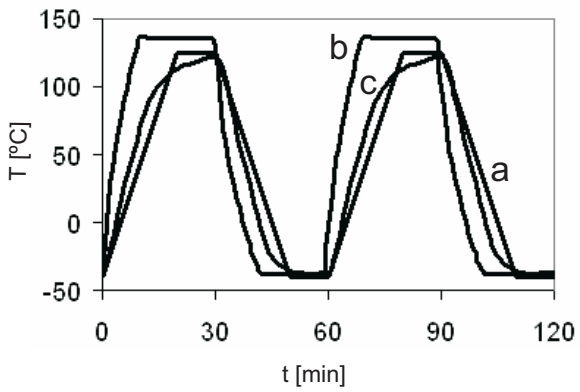

Figure 4.4: Thermal cycling temperature profile, ramp rate: 11°C. (a: required profile, b: air in test chamber, c: temperature on sample, Philips Applied Technologies).

After thermal cycling, strain gages were attached to the specimens to measure the overall Young's modulus which is used later as a macroscopic damage indicator. Four strain gages were glued on the damaged samples; two perpendicular to the loading direction for temperature compensation and two active gages for the displacement measurement. Tensile tests were performed in a computer controlled double spindle micro-tensile stage shown in Figure 4.5. A 20 N load cell was used and the clamp speed was equal to 0.5 μm/s. An appropriate strain (in the order of e-5) was applied to produce a stress of $\sim$2 MPa in the cross-section of the specimen. The critical resolved shear stress for some slip systems in Sn is as low as 3-4 MPa [57]. Therefore, in order to limit the amount of plasticity in the material, the stress level was chosen to be below 2 MPa. The calculations were computed over the elastic range of the hysteresis curves. A reference elastic modulus value of 64$\pm$1 GPa was measured prior to thermal cycling.

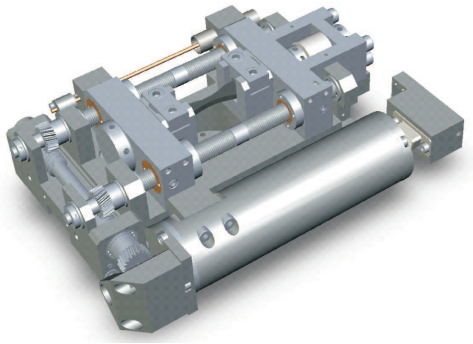

Figure 4.5: Double spindle micro-tensile stage (Kammrath&Weiss).

4.2.2 Results and Discussion

Bulk SnAgCu specimens were thermally cycled between -40 and 125°C. Figure 4.6 shows optical images of sample surfaces after N=0, 500, 1500 and 2000 temperature cycles. On the initial specimen surface (N=0) only the hard eutectic intermetallic particles are visible. After 500 cycles, grain boundaries become directly visible as well. Many small cracks appeared on the grain boundaries due to thermal fatigue. Further cycling results in pronounced deformation patterns around the grain boundaries. Damage is highly localized at intergranular regions whereas there is no noticeable damage in the core of the grains. After 2000 cycles, due to the amount of deformation, it is no longer possible to optically focus on the specimen surface. The damaged zones appear to expand towards the grain interior. Especially around triple points, a large area is affected. Yet, the bright flat regions suggest that most of the grain interiors remain free of damage. Figure 4.7 shows a SEM image of the deformation after 1000 cycles around a triple point. As a result of surface roughening, OIM scanning was no longer possible.

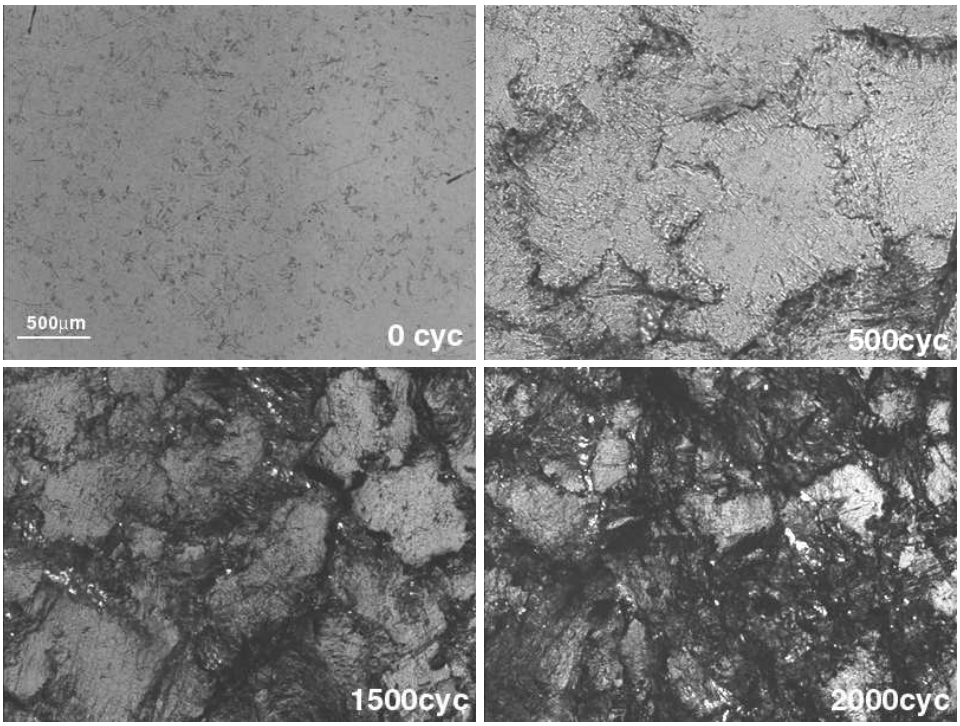

Figure 4.6: Thermal cycling bulk SnAgCu between -40 and 125°C , N=0, 500, 1500, 2000, optical images all at the same magnification.

Thermal fatigue cracks on grain boundaries are further investigated by OIM. In Figure 4.8, three different regions of a sample are shown after N=500 cycles. For every region three images are shown; the first image is the SEM micrograph, the second is the corresponding inverse pole figure (IPF) intensity map, and the third one is the

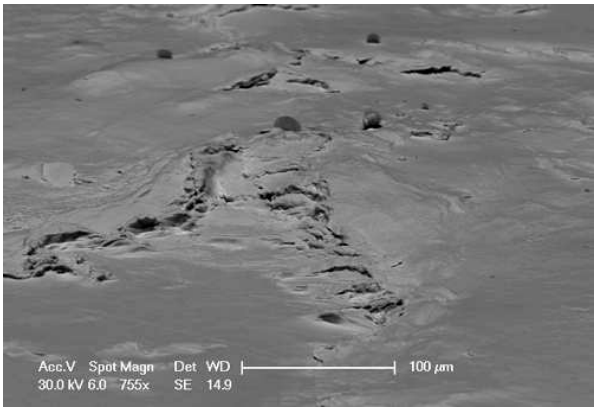

Figure 4.7: Deformation around a triple point after N=1000 T cycles between -40 and 125°C, SEM image.

corresponding misorientation angle map. The misorientation angles are calculated from adjacent pairs of data points with respect to [001]-Sn axis. In region 1, all grain boundaries except the ones with a mismatch angle lower than 15° are clearly damaged. In the middle a fatigue crack is visible on a 15-45° boundary. In region 2, a large crack is visible in the middle section at a 60-75° boundary. Other 60-75°, or higher mismatch boundaries show less damage compared to this central crack. In region 3, degradation at a triple point is noticed again at a 60-75° boundary. The rest of the image does not reveal noticeable damage. In all three regions discussed, grain interiors and low angle grain boundaries are hardly damaged, whereas all high angle boundaries are damaged to a varying extent. On several occasions a grain boundary with a lower mismatch angle damages more than a boundary with a higher mismatch angle. This is due to the fact that not only the grain boundary misorientation angle but also the mismatch factor, the projection of local grain orientations on the grain boundary plane, plays a key role in the stress concentrations at the boundary [58]. The mismatch factor is discussed in detail in Section 4.3.

Cycled specimens are mechanically tested in order to quantify the thermal fatigue damage. Hysteresis curves for 2 mm thick specimens are shown in Figure 4.9 a. It is seen that thermal cycling results in mechanical softening in the specimens, thus fatigue cracks on the grain boundaries severely affect the overall mechanical properties. It should be noted that these observations only result from thermal cycling, since no mechanical constraints were applied to the specimens. Global Young's moduli measured before and after thermal cycling are plotted in Figure 4.9 b. In the figure, measurements are shown after N=0, 500, 1000, 1500, 2000, 3100 and 4000 cycles for 1, 2 and 3 mm thick specimens are shown. Each error bar indicates 12 measurements.

Although cyclic softening is observed in all specimens, the amount of deformation clearly shows a size-effect. Thinner specimens suffer more from thermal fatigue than thicker specimens. In the thickness direction, 3 mm thick specimens contain 3-5 grains, whereas 1 mm thick specimens contain mostly a single grain. Thus, if a

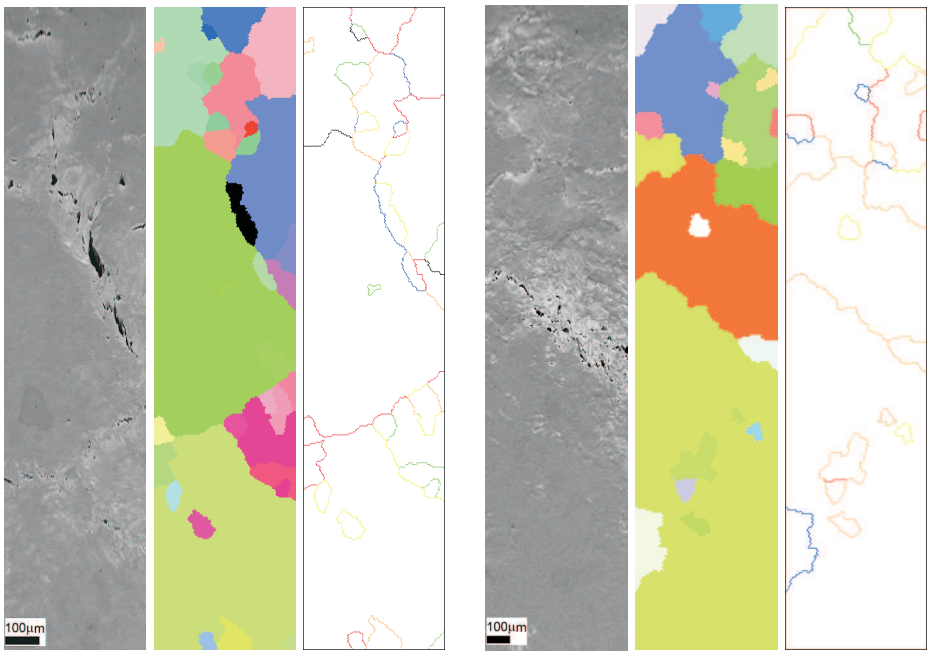

(a) Region 1 (b) Region 2

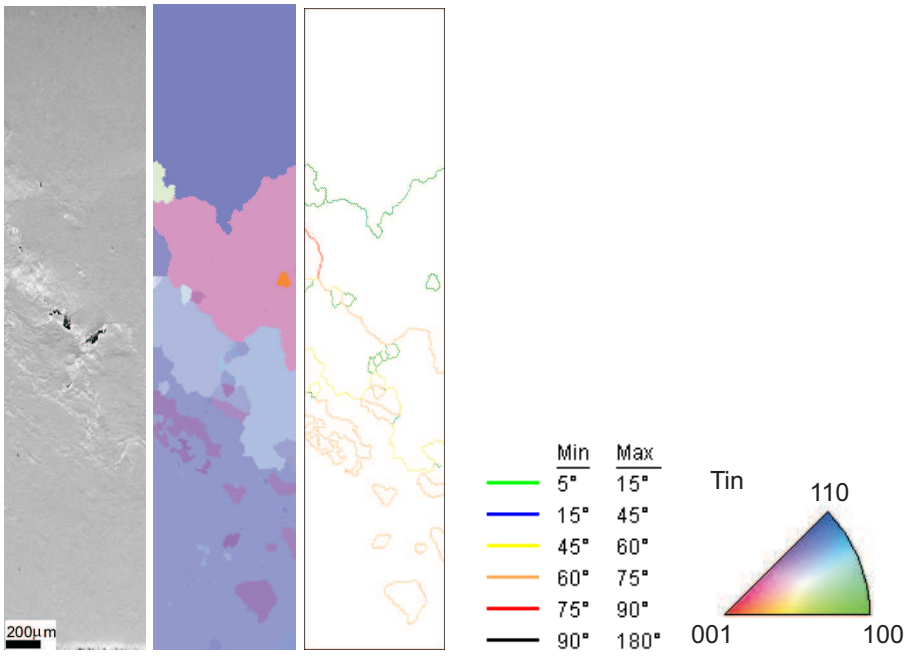

(c) Region 3

Figure 4.8: SEM images, corresponding OIM scans and misorientation angles between grains for three different regions in SnAgCu after N=500 cycles between -40 and 125°C.

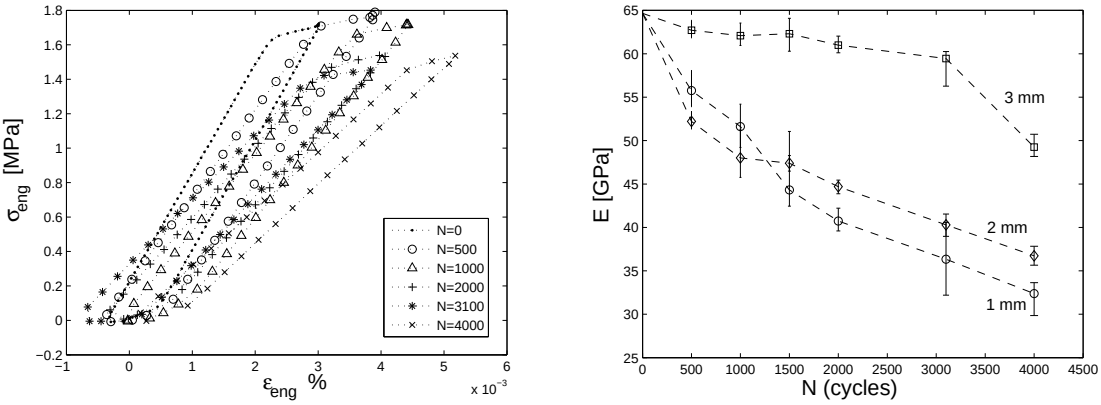

Figure 4.9: Stress-strain hysteresis curves for selected experiments of 2 mm samples (left), global elastic moduli measured as a function of temperature cycling (right).

grain boundary is damaged in the thinner specimens, the material continuity is lost more rapidly and the applied load cannot be transmitted through the specimen.

4.3 Simulations

Thermal cycling experiments are simulated incorporating the local grain orientations and the microstructure of the test specimens. OIM scans of test specimens are used to identify grain boundaries as a collection of 2D line vectors and to store all local Euler angles. The grain boundary lines are directly transferred to the finite element geometry on the basis of which the discretization is performed. To assign crystallographic orientations to the grains, first the OIM reference frame has to be rotated to coincide with the FEM reference frame (Figure 4.10).

OIM scans relate the local crystal orientation to the OIM reference frame in Euler angles (ϕ,θ,ψ) by the so-called x-convention method. The local crystal orientation

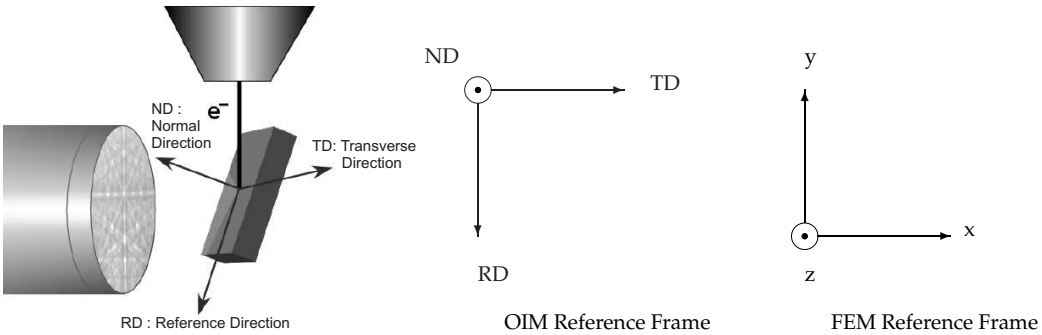

Figure 4.10: OIM set-up and OIM and FEM reference frames.

with respect to the OIM reference frame is found by three subsequent rotations; 1st rotation around normal direction (ND) by an angle ϕ (R_ϕ), 2nd rotation around reference direction (RD) by an angle θ (R_θ) and 3rd rotation again around ND, by an angle ψ (R_ψ). Last, the OIM reference frame is rotated 90° (R_{OIM}) to match the FE reference frame. All four rotations are combined in a single rotation matrix R according to Eqn 4.1, where each matrix is defined with respect to the vector basis resulting from the previous rotation step. The grain boundaries in the thickness direction are assumed to be straight and perpendicular to the surface. The resulting grain orientations are thereby approximately expressed in the FEM coordinate system.

$$R = R_\phi R_\theta R_\psi R_{OIM} \tag{4.1}$$

where

$$R_\phi = \begin{bmatrix} cos\phi & -sin\phi & 0 \\ sin\phi & cos\phi & 0 \\ 0 & 0 & 1 \end{bmatrix} \qquad R_\theta = \begin{bmatrix} 1 & 0 & 0 \\ 0 & cos\theta & -sin\theta \\ 0 & sin\theta & cos\theta \end{bmatrix}$$

$$R_\psi = \begin{bmatrix} cos\psi & -sin\psi & 0 \\ sin\psi & cos\psi & 0 \\ 0 & 0 & 1 \end{bmatrix} \qquad R_{OIM} = \begin{bmatrix} 0 & 1 & 0 \\ -1 & 0 & 0 \\ 0 & 0 & 1 \end{bmatrix}$$

A SnAgCu bulk specimen with dimensions 15×3×1.5 mm is simulated as explained above using 3D solid elements. The model consists of 40 grains and ∼9000 elements. SnAgCu is modeled with a steady-state creep model [30] in combination with an initial linear elastic regime (E=64.1 GPa, ν=0.4). The anisotropic thermal expansion coefficients are assigned to individual grains as given in Section 4.1. Figure 4.11 shows the OIM scan and the resulting equivalent Von Mises stresses σ_{vm} at 125°C. In the contour plot, the high stress regions are most likely to be subject to thermal fatigue damage.

The expected stress concentration on the boundaries is related to the grain boundary mismatch factor M [58], which is a coefficient giving the difference between the projected local [001] directions (i.e. the short BCT axes) of the neighboring grains on the grain boundary plane:

$$M = \|(\vec{c}_1 - \vec{c}_2) \cdot (\mathbf{I} - \vec{n}\vec{n})\| \tag{4.2}$$

where the components $\vec{c}_i$ are the crystallographic [001]-directions of the two grains and $\vec{n}$ is the normal to grain boundary plane. The role of the mismatch factor is illustrated in Figure 4.12, where two Sn grains separated by a grain boundary is thermally loaded and the resulting stress concentrations are examined. Two models are presented which **only** differ through the grain boundary normal used, which is n=[100] for the top mesh and n=[1$\bar{1}$0] for the bottom mesh. The local [001]-Sn

Figure 4.11: OIM scan of an 15×3×1.5 mm SnAgCu bar (top) and the predicted Eqv. Von Mises stresses [MPa] at 100°C (bottom).

orientation for both cases is $\vec{c}_1 \Rightarrow[\bar{1}\bar{1}0]$ for grain 1 (g1) and $\vec{c}_2 \Rightarrow[\bar{1}10]$ for grain 2 (g2). The resulting σ_{vm} at 100°C for both models are shown in the same figure. Although the crystal orientations are the same, the top mesh is stress free at 100°C whereas the bottom mesh exhibits a stress of σ_{vm}= 65 MPa around the grain boundary.

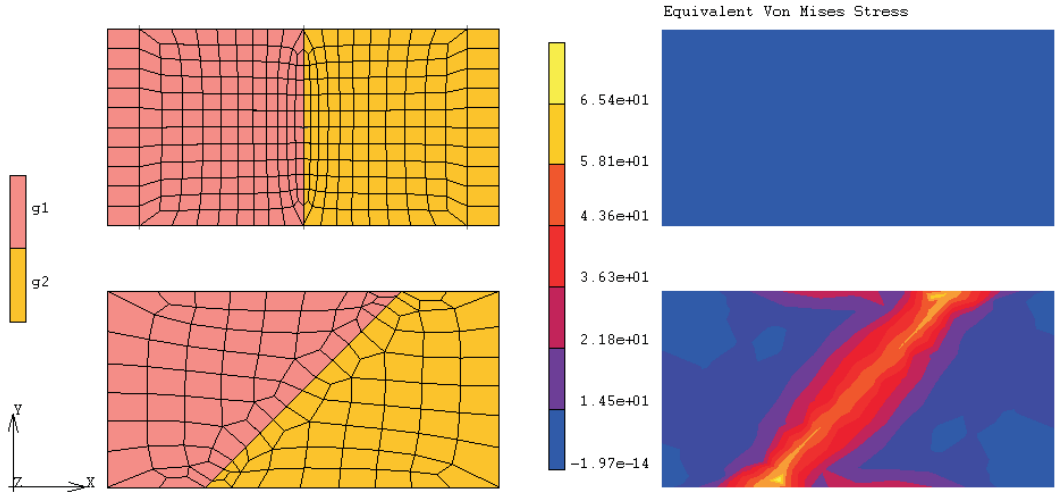

Figure 4.12: The effect of grain boundary normal on the amount of stress concentration (MPa) at the grain boundary.

A crystallographic equivalent direction of $\vec{c}_1 \Rightarrow[\bar{1}\bar{1}0]$ in grain1 is $\vec{c}_1{}^* \Rightarrow[110]$. For grain 2, the crystallographic equivalent of $\vec{c}_2 \Rightarrow[\bar{1}10]$ is $\vec{c}_2{}^* \Rightarrow[110]$. For the top mesh,

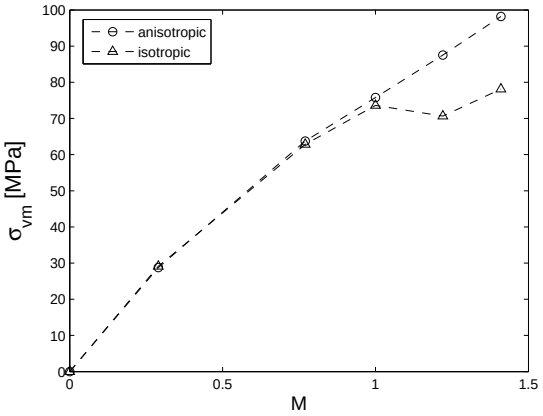

Figure 4.13: A comparison between anisotropic and isotropic material properties of SnAgCu on the effect of mismatch factor M and stress concentrations on the grain boundary.

the mismatch factor using (c_1,c_2) pair yields M=0. However, if the pair (c_1,c_2^*) is chosen, the mismatch factor would equal M=$\sqrt{2}$. In the top mesh a stress free state is calculated because in at least one of the four possible $c_{1,2}$ combinations, the mismatch factor equals M=0. In the bottom mesh, for all possible $c_{1,2}$ combinations, (c_1,c_2) , (c_1,c_2^*) , (c_1^*,c_2) , (c_1^*,c_2^*), the mismatch factor equals to M=1. For this reason, a stress concentration is observed at the grain boundary in the bottom mesh. Thus, in the calculation of the mismatch factor, it is imperative to consider all crystallographically equivalent directions. The mismatch factor should be calculated with the $c_{1,2}$ pair giving the smallest projection on the grain boundary:

$$\mathrm{M} = \min_{\forall \vec{c}_{1,2}{}^*} \|(\vec{c}_1 - \vec{c}_2) \cdot (\mathbf{I} - \vec{n}\vec{n})\| \tag{4.3}$$

A number of simulations yielding different M values have been carried out in 3D, assuming isotropic and anisotropic **mechanical** material properties [54] for β-Sn. All results are plotted in Figure 4.13. It is seen that as the mismatch factor increases the stress concentration along the grain boundary also increases, where anisotropic mechanical material properties give more realistic results. Due to the symmetry in a 2D simplification, the mismatch factor cannot exceed M=1. The theoretical maximum mismatch (M=$\sqrt{2}$) is reached when $\vec{c}_1$, $\vec{c}_2$ and the grain boundary normal are orthogonal to each other, which is only possible in 3D.

4.3.1 Parameter identification

The cohesive zone model introduced in Chapter 3 is also employed here to characterize the thermal fatigue behavior of Sn grain boundaries. The constitutive equations

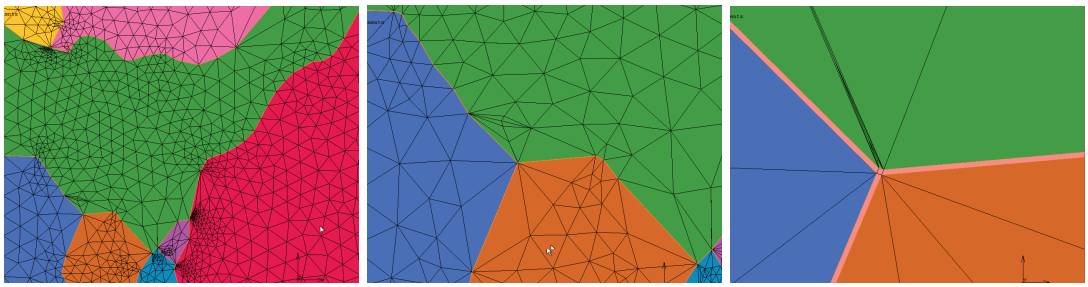

Figure 4.14: Sections from a sample mesh with local magnifications showing the granular structure and cohesive zone elements at the grain boundaries.

of the CZM were given in Eqn.s 3.1, 3.2 and 3.6.

The parameter identification is performed on the basis of 1 mm thick test specimens, as justified by the following arguments. First, the 1 mm thick specimens have a single grain in the thickness and thus grain boundaries perpendicular to the specimen surface can be effectively approximated in 2D. For thicker specimens such a simplification cannot be made since there are more grains in the thickness. Second, the biggest solder balls used in BGA packages have a diameter of 760 μm, which is closely represented by the considered specimens, since their thickness reduces to $\sim$800 μm after the initial surface preparation. The simulations are simplified to 2D as explained above, to prevent laborious 3D calculations. A plane-stress assumption is made since out-of plane deformations were observed in the test specimens (Figures 4.6 and 4.7).

The mesh is produced by placing cohesive zone (cz) elements at the grain boundaries using the OIM output files, such that the tangential direction of the cz element corresponds with the grain boundary plane, and the normal direction is parallel to the grain boundary normal. As explained in Section 3.4.1, cz elements are assigned an extremely small, yet finite, initial thickness t_{cz}=100 nm, by which a finite initial stiff-

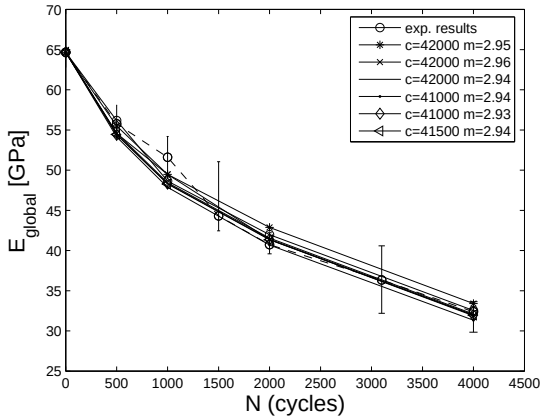

Figure 4.15: Fit of cohesive zone based fatigue damage model to experimental results.

ness is calculated such that cz-elements do not alter the initial stiffness of the overall system. To prevent loss of continuity in the mesh during computation, a tiny finite sized cz element is placed at the triple points, as shown in Figure 4.14. After placing cz elements at the grain boundaries, grains are meshed using triangular elements with 6 nodes. The crystallographic orientation of each grain is calculated by using only the in-plane components (local [100]-Sn and local [001]-Sn). Doing so, the short axis in the Sn lattice causing the anisotropic behavior, lies in the x-y plane for every grain, enabling an approximate 2D analysis.

In the simulations, two load cases are subsequently applied. First the material is thermally cycled between -40 and 125°C as shown in Figure 4.4. The ramp rate, peak hold and cycle duration were consistent with the experimental conditions. Eight increments were calculated per cycle. Applied boundary conditions allowed the specimen to expand and shrink freely. Thermal cycling is followed by a tensile test, which is treated as a separate loadcase with a prescribed axial elongation up to σ_{xx}=2 MPa. Using the resulting reaction force and the applied displacement, average global stresses and strains are calculated, and the global elasticity modulus is extracted. Experimental results and simulation results with different damage parameter sets are shown in Figure 4.15. Using a least squares minimization, a good agreement between the experiments and simulations was achieved with the parameter set {c m r}={42e3 2.94 0} in Equation 3.2. These values can be further improved in the context of a full 3D analysis.

4.3.2 Sensitivity Analysis

The representativeness and the uniqueness of the identified parameters is further examined in this section. The effect of small modifications in the mesh, i.e. grain boundary normal, grain orientations, grain size, on the overall mechanical properties is investigated using the damage evolution law with the same parameter set:
{c m r}={42e3 2.94 0}

In Figure 4.16, the experimentally measured E_{global} values for 1 mm samples and all modified simulation results obtained by using the same parameter set as given above are plotted. First grain boundaries are tilted randomly between 0-5°. Then the grain orientations are modified such that the local (010)β-Sn plane, which contains one long axis [100] and the short axis [001], is rotated clockwise randomly for each grain between 0-5°, 0-15° and 0-30°. Finally, 10% of the grains are merged with other grains. It is seen that the damage law characterized by experiments is capable of representing a variety of specimens which differ in grain size, orientation, and grain boundary geometry, provided that the specimen is still polycrystalline.

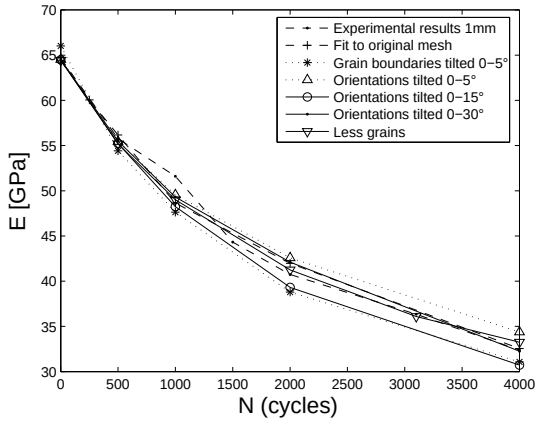

Figure 4.16: Effect of microstructural modifications in a simulated specimen on the overall results obtained with a single set of damage evolution parameters.

4.3.3 BGA solder ball simulations

In this section, the bulk SnAgCu damage model given in this study and the interfacial damage model regarding the SnAgCu/Ni-Au interface are combined to simulate thermomechanical fatigue damage evolution in BGA solder balls.

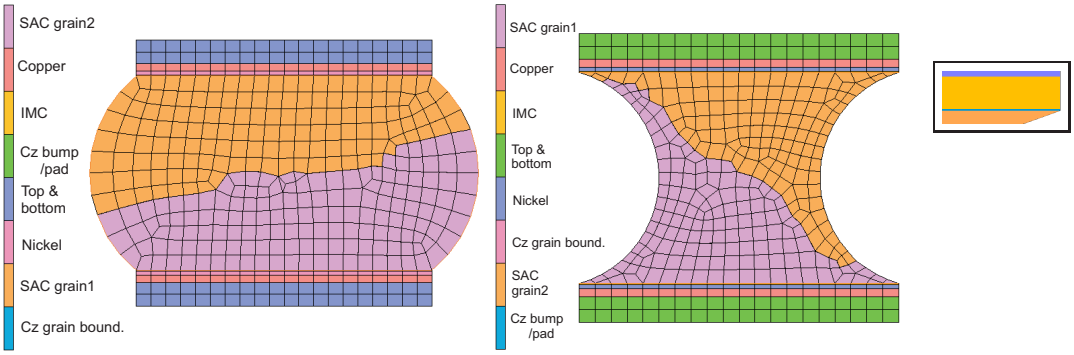

Figure 4.17: Finite element mesh of a standard solder ball and an hourglass joint.

Two solder joints are modeled in 2D plane stress, as shown in Figure 4.17. On the left is a standard solder bump with 2 grains where the misorientation angle between the local [001]-Sn directions is 75°, corresponding to an average mismatch factor M=0.81. On the right is an hourglass joint, often encountered in flip-chip joints, also composed of two grains. High-standoff hourglass solder joints are known to improve fatigue life [59].

In this study, the hourglass joints are examined with the presence of an underlying microstructure. The grain boundary cuts the joint diagonally; local [001]β-Sn orientations of the grains are [110] and [$\bar{1}$10], respectively, such that the mismatch factor is

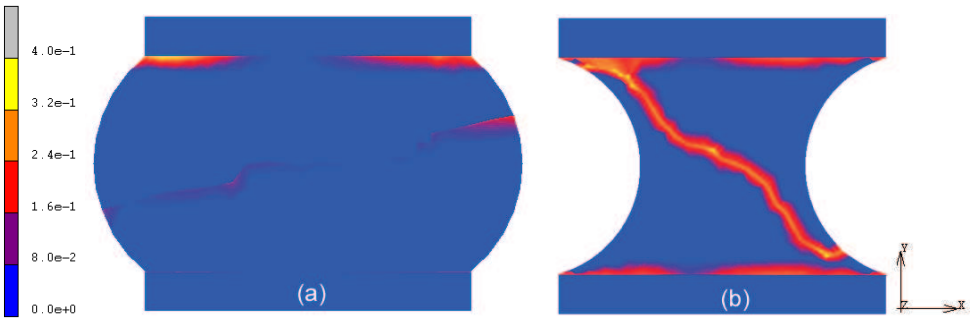

Figure 4.18: Contour plot of D_{eff} in SnAgCu solder joints, (a) Standard ball N=5000, (b) Hourglass joint premature failure at N=1180 thermal cycles.

approximately M=1. Both solder joints are 760 μm in diameter at the bump/pad, 500 μm in height, with a 20 μm Cu/ 10 μm Ni metallization. There is a 2 μm Ni_3Sn_4 intermetallic compound between the metallization and the solder. Between the bump/pad interfaces and the grain boundaries, 100 nm thick cz-elements are placed. The proper governing damage law and the initial stiffness is assigned to each of the cohesive elements. A cyclic thermal load between -40 and 125°C is applied to every element. One corner is fixed and the top and bottom layer nodes are constrained in the x-direction. The used material models, elastic material constants and damage evolution parameters are tabulated in Table 4.3.3.

In [43], the fatigue life of an interface is defined as the number of cycles where D_{eff}=0.5. Figure 4.18 shows the contour plot of D_{eff} for both solder joints. In the contour plot the damage values in the cohesive zone element nodes are smeared out by nodal averaging for visualization. Damage evolution takes place both at the bonding interface and at the grain boundaries at different rates. In the standard solder bump on the left, the average damage in the top bump/pad interfacial cz nodes is D_{eff}^{avg}=0.25, and in the grain boundary cz nodes it is D_{eff}^{avg}=0.05 after N=5000 cycles. In the hourglass solder joint, after N=1180 cycles the grain boundary has completely failed and thus the calculation ends prematurely. These two solder joints have the

Table 4.1: Elastic material constants and damage evolution parameters.

Material	**model**	**E**[GPa]	ν
SnAgCu	visco-el.pl.	64.1	0.4
Cu	lin.el	128	0.35
Ni	lin.el	197	0.31
Ni_3Sn_4	lin.el	140.4[a]	0.2
Cz sets	**c**	**m**	**r**
SnAgCu-Ni/Au, normal[b]	68000	3.16	1e-6
SnAgCu-Ni/Au, tangential[b]	47000	3.135	4e-5
SnAgCu, intergranular	42000	2.94	0

[a] Jang et al.2004, [b] Erinc et al.2007

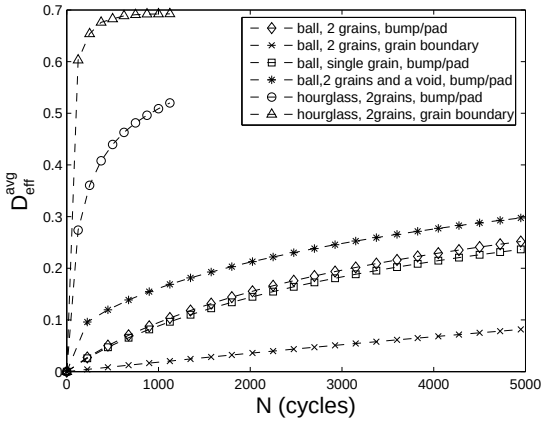

Figure 4.19: Fatigue life and failure zone prediction in solder joints.

same materials, same boundary conditions and a comparable mismatch factor at the grain boundaries; only the joint geometry is different.

In a BGA solder ball, overall failure preferentially occurs at the bump/pad interface under thermomechanical loading. A number of explanations for this can be traced. First, the ball shape localizes stresses at the bump/pad interfaces. The hourglass joint on the other hand, shows stress concentrations near the middle of the joint which enhances crack propagation on the grain boundaries. In [60] hourglass solder joints with a fatigue crack through the middle of the joint, among with other fracture modes are clearly shown. Also, the values of c given in Table 4.3.3 indicate that the intergranular interfaces are less prone to damage than the bump/pad interface. Obviously, the bump/pad interface is mechanically weaker than Sn grain boundaries. Furthermore, thermal fatigue damage always affects the bump/pad interface, however along the grain boundaries, the amount of thermal fatigue damage is determined by the crystallographic mismatch between neighboring grains. In an hourglass joint however, depending on how critical the mismatch factor at grain boundaries is, the overall failure might take place across the joint intergranularly.

Figure 4.19 shows damage evolution against the number of thermal cycles in the cz elements for different models. The expected failure zone for the solder ball is the bump/pad interface since damage evolution at the bump/pad is significantly higher than that of the grain boundary. In the solder ball model, if the grains are assigned the same lattice orientation, i.e. a single crystal solder ball, damage evolution at the bump/pad interface slows down slightly. A more realistic solder ball is obtained by inserting a void (or blowhole) with dimensions of $1/10^{\text{th}}$ the size of the interface in the model. After N=5000 cycles, the average damage in the top bump/pad interfacial cz nodes is approximately $D_{\text{eff}}^{\text{avg}}$=0.3. For the hourglass joint, overall failure occurs already at the grain boundaries with the same boundary conditions applied to the solder ball.

The present analyses suggest that, for a standard solder bump, the continuity of the bump/pad interface is more important than the microstructure of the solder ball.

However, for an hourglass joint, the microstructure is crucial since existence of critical grain boundaries might cause fatigue crack propagation and overall failure across the joint. Based on the adopted analytical formula for the damage evolution, an estimate for the lifetime can be computed. The standard solder bump with the good interface will fail at their bond/pad interface at N≈27e3 cycles whereas the ball with a blowhole will fail at N≈18e3 thermal cycles between -40 and 125°C according to the selected failure criterion. The analysis suggests that a small void such as 1/10 length of the interface reduces the fatigue life of the joint by 1/3.

4.4 Conclusions

Thermal fatigue damage mechanisms in bulk Sn4.0Ag0.5Cu lead-free solder are examined in correlation with the underlying microstructure. All observations and results reflect the response under pure thermal cycling, with no mechanical constraints. Intergranular fatigue cracks induced by the intrinsic thermal anisotropy of β-Sn are here predicted through the damage in the interfacial cohesive zone elements. The mechanical degradation in the thermally cycled specimens measured by tensile experiments is used to identify the damage evolution parameters using a coupled numerical-experimental approach. The representativeness of the parameters is investigated by a sensitivity analysis. The model is applied to BGA solder balls, and the thermomechanical fatigue life is predicted. From the present study, the following conclusions are drawn:

- Thermal fatigue loading causes local damage patterns along Sn grain boundaries. At grain boundaries where the local mismatch angle between two grains was less than 15°, no significant damage was observed. For higher angle boundaries, the amount of deformation depends on the mismatch factor on the boundaries. The surface deformation was clearly visible without any magnification.

- Thermal fatigue cracks on the grain boundaries severely affect the overall mechanical properties. In the worst case, after N=4000 cycles the stiffness has dropped to half of its initial value.

- SnAgCu reflects size dependent thermomechanical properties. Thick samples with more grains in the thickness are more resistant to thermal fatigue than thin samples where only a single grain in the thickness remains.

- The degradation of the overall stiffness due to thermal fatigue is used as an input to identify damage evolution parameters for a cohesive zone based interfacial fatigue damage model by inverse modeling. A good agreement between the experiments and simulations is established.

- The damage model investigated is used to assess microstructural aspects in the thermomechanical fatigue life of BGA solder joints. The simulations suggest

that for a standard BGA ball, the integrity of the bump/pad interface is more important than the microstructure in this respect. For hourglass solder joints, depending on the geometry, intergranular damage might dominate over interfacial damage.

In continuation to this work, different ranges of temperatures in thermal cycling can be investigated to relate the amount of damage to the temperature range applied. In the following chapter, a statistical representation of SnAgCu solder ball microstructures and interfacial defects are established, and the model is expanded to a 3D chip scale fatigue life prediction tool.

CHAPTER FIVE

Microstructural modeling and fatigue life predictions[1]

Abstract

The ongoing miniaturization trend in the micro-electronic industry enforces component sizes to the micron, or even to the nano scale. At these scales, the underlying microstructural sizes and the geometrical dimensions are comparable. The increasing influence of microscopic entities on the overall mechanical properties makes continuum material models more and more questionable. In this study, the thermomechanical reliability of lead-free BGA solder balls is investigated by microstructural modeling. Microstructural input is provided by orientation imaging microscopy (OIM), converted into a finite element framework. Blowholes in BGA solder balls are examined by optical microscopy and a statistical analyses on their size, position and frequency is conducted. Combining the microstructural data with the appropriate material models, three dimensional slice models are created. The fatigue life of the package is determined through a critical solder ball. The thermomechanical reliability of the slice models are predicted using cohesive zone based fatigue damage models. The simulation results are validated by statistical analyses provided by the industry. Microstructural modeling allows to predict and understand the scatter in the solder ball fatigue life in reality. The methodology used in this study will be further used to assess solder interconnect reliability under different geometrical and/or loading conditions.

[1] *Reproduced from*: M. Erinc, P.J.G. Schreurs, M.G.D. Geers (2007). Microstructural modeling and interfacial reliability of SnAgCu solder interconnects. *Microelectronic Engineering*, submitted.

5.1 Introduction

In microelectronic packages, mechanical integrity and electrical connection is utilized by solder connections. Lead being a toxic element, the microelectronics industry has switched to lead-free solders in 2006. Since then, near-eutectic and eutectic compositions of SnAgCu alloy are being extensively used as a replacement for the traditional SnPb solder. Solder joints are exposed to thermomechanical fatigue loading caused by the fluctuations in local operating temperatures. Repeated heating and cooling of the device provokes cyclic mechanical strains resulting from the CTE mismatch between the different materials in the package (Figure 5.1).

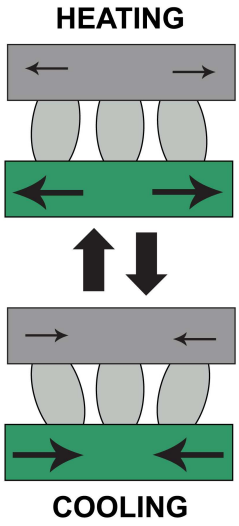

Figure 5.1: Solder fatigue resulting from CTE mismatch.

As discussed in the previous chapter, Sn based solders are prone to thermal fatigue damage even without being mounted on the package. The thermal anisotropy of the β-Sn phase causes intergranular fatigue damage upon cyclic thermal loading [47–50]. Both damage mechanisms have been previously addressed in the preceding chapters, where cohesive zone based interfacial fatigue damage models were characterized by inverse modeling through dedicated fatigue experiments [16, 26, 61, 62].

Fatigue life predictions for BGA or flip-chip solder balls in the literature are conducted using mainly Coffin-Manson, J-integral, power law or sinh type of creep models [63–67]. A distinguished study on solder joint reliability is given in [33] where the fatigue crack trajectory and fatigue life of a solder joint is predicted through a numerical-experimental approach. A review on solder joint fatigue models with respect to their applicability to chip-scale packages is given in [32].

As a result of miniaturization, the increasing influence of microscopic entities on the overall mechanical properties makes continuum material models that ignore the microstructure questionable. The original aspects which will be forwarded in this study

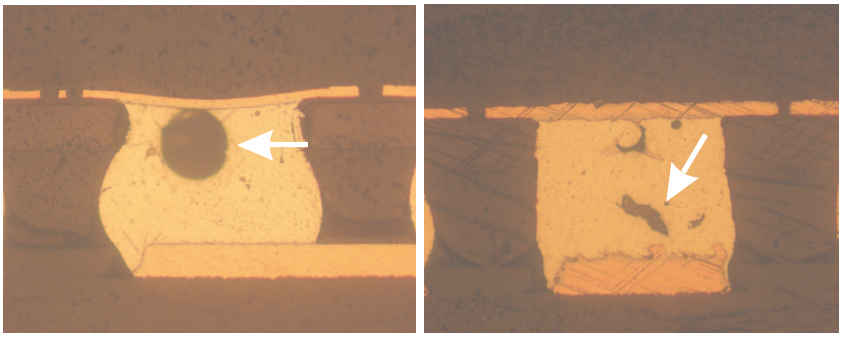

Figure 5.2: Manufacturing defects, i.e. blowholes(left), under-flow gaps (right), in BGA packages with SnAgCu solder balls, optical images $\times 20$.

are: (i) a full microstructural model of SnAgCu solder balls based on crystallographic scans, (ii) incorporation of initial defects in solder reliability analysis in a statistical manner.

In this study, thermomechanical fatigue life of SnAgCu solder joints are predicted by microstructural modeling. The microstructural input for the finite element models are supplied by detailed experimental analyses. Fatigue damage evolution is simulated through cohesive zone based interfacial fatigue damage models. The fatigue life predictions are compared with the experimentally obtained failure distributions of BGA packages from the industry. It will be shown that microstructural modeling adequately predicts and explains the diversity and scatter in the available experimental data. SnAgCu solder ball crystallography and manufacturing defects (i.e. voids, under-flow, over-flow etc.) are discussed in Section 5.2. Following the experimental part, the numerical techniques and the simulations are presented in Section 5.3, including the cohesive zone formulation, microstructural modeling, fatigue life predictions and validation.

5.2 Experimental Analyses

5.2.1 Blowholes in solder balls

Blowholes (or voids) are commonly observed in BGA solder balls. They appear during reflow as a result of the entrapment of gases released by the solder paste. Small voids might arrest a propagating crack and enhance fatigue life. However, if the decrease in the cross-sectional area at the bump/pad interface is causing a critical stress concentration, the fatigue life will decrease. Determining the optimum void size for crack arrest is out of the scope of this study. Nonetheless, a statistical analysis on voids in BGA packages is presented below.

Six newly manufactured EFSOT-BGA256 packages were cross-sectioned row by row. The solder balls were examined by an optical microscope for defects at their maximum diameter ($\sim$760 μm). The images were collected by a digital camera mounted

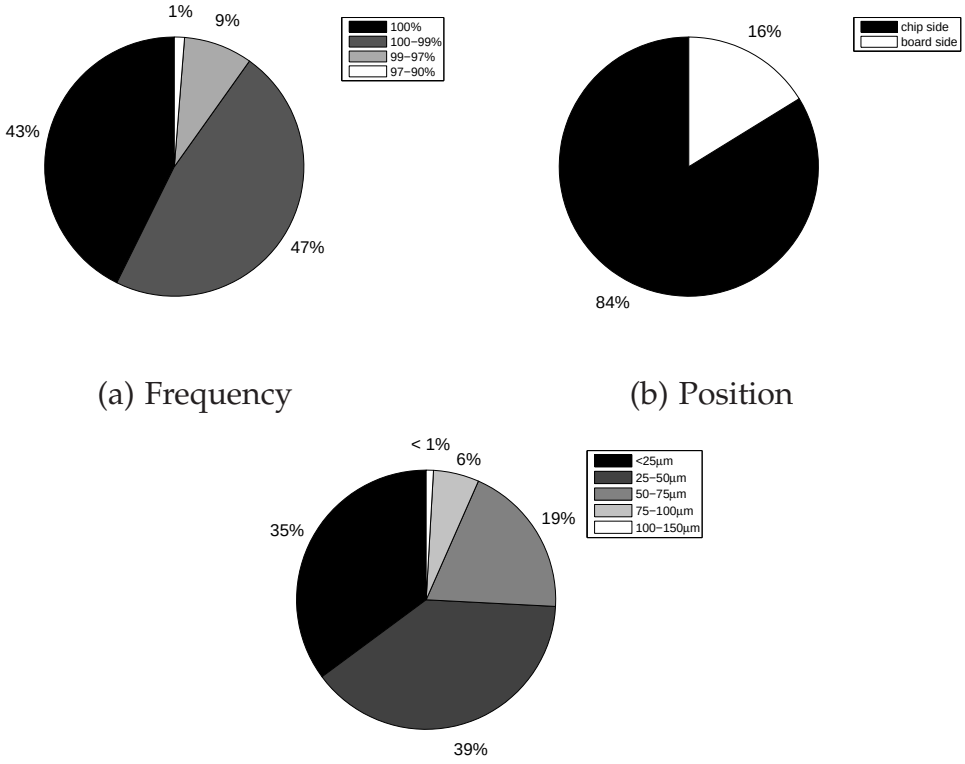

(a) Frequency (b) Position

(c) Diameter

Figure 5.3: Distribution of blowholes in BGA packages.

on the microscope, and void dimensions were measured using an image analysis software. Figure 5.2 shows examples of manufacturing defects encountered in BGA solder balls. Apart from blowholes, defects due to under-flowing were also observed. The data collected from these packages is plotted in Figure 5.3. From all the solder balls examined, 57% contained voids with an average of 1.5 void per ball. 84% of all the voids observed were on the chip side. Solder balls with big voids (>100 μm) were rare (<1%). If the solder contained a void, in almost half of the cases the voids volume was less than 1% of the solder ball volume.

Since the analysis was done by cross-sectioning, the results above are an underestimate of the three dimensional reality.

5.2.2 Crystallography

In order to establish a microstructural database for SnAgCu solder balls, 0.76 μm diameter solder balls are scanned by Orientation Imaging Microscope (OIM). Solder balls were molded in a 2 mm thick epoxy resin mixed with copper powder against charging. Surface preparation was done according to Struers protocols for solder alloys.

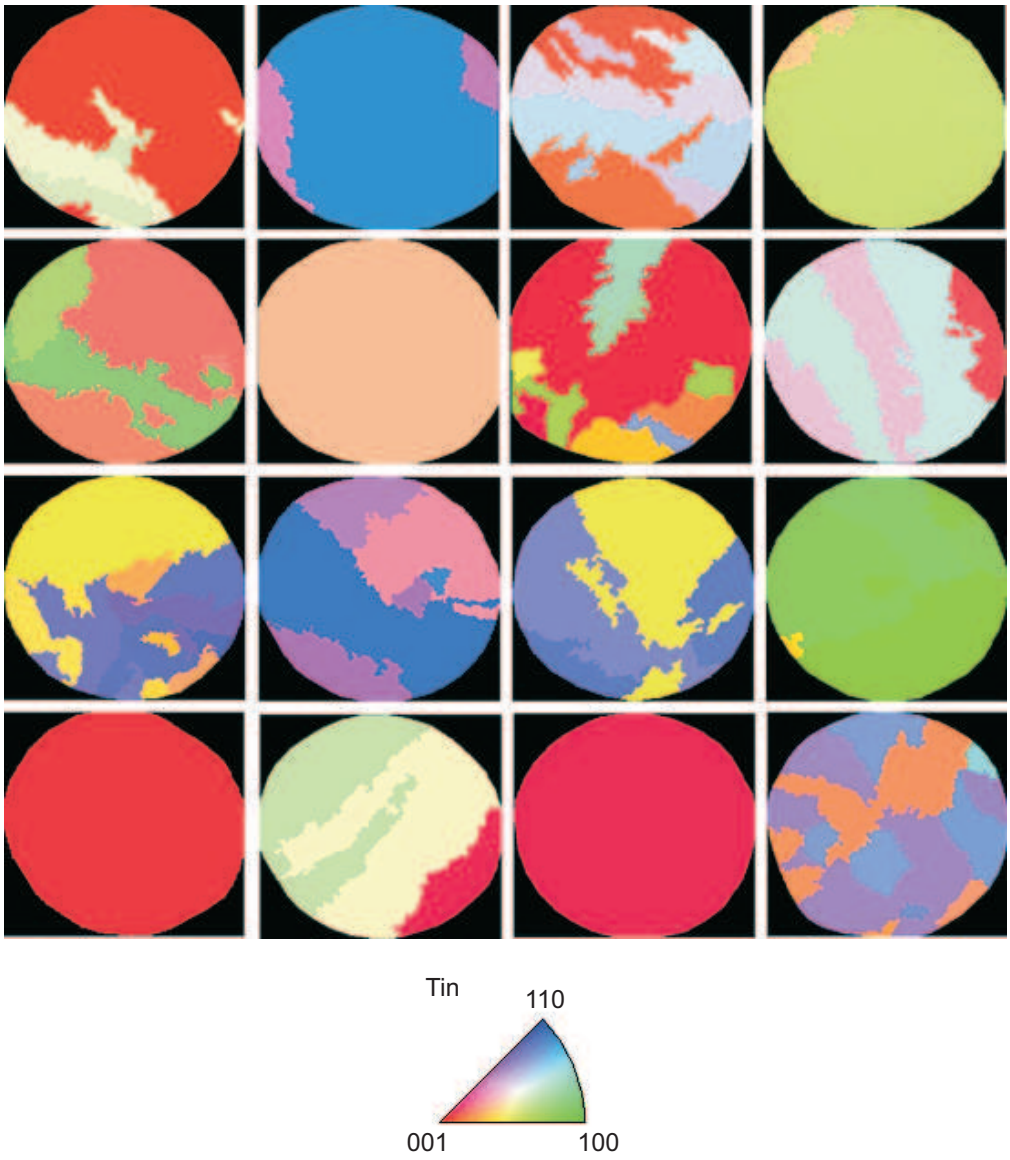

Figure 5.4: OIM scans of 760 μm diameter Sn4Ag0.5Cu solder balls.

Solder balls were cross-sectioned at their maximum diameter and scanned under 30 kV, with a step size of 3 μm. A selection from these scans is shown in Figure 5.4. Approximately 20% of the solder balls appear to be single crystal, 50% contains 2–5 grains and the remaining 30% contains 6–11 grains. The crystallographic orientation of each grain is given by Euler angles and recorded in an output file. The results are filtered such that:

- Minimum neighbor confidence index was set to 0.8 out of 1.
- Grain dilatation tolerance angle was set to 5°.
- There was a single orientation per grain.

5.3 Numerical Analyses

5.3.1 Cohesive zone model

In the work of Abdul-Baqi et al. [43], thermomechanical fatigue damage in solder balls is modeled by a cohesive zone approach and a damage evolution law specific for solder materials is proposed which was previously discussed in Section 3.4. In the current analysis, this model is extended to 3D.

The 3D cohesive zone element is shown in Figure 5.5. The local coordinate system is defined on the mid-plane of the element. Two tangent vectors ($\vec{t}_1$ and $\vec{t}_2$) are located on the mid-plane, and the normal vector $\vec{n}$ is found by the cross-product of these tangents. Opening vectors ($\vec{\Delta}$) at the integration points are calculated from the global openings at element nodes and rotated to the local coordinate system. Using the components of $\vec{\Delta}$, the components of the traction vectors in the normal and tangential directions (T_n, T_{t1}, T_{t2}) are calculated as follows:

$$T_i = k_i(1 - D_i)\Delta_i, \quad \text{where} \quad i = n, t_1, t_2 \tag{5.1}$$

where k_i is the initial stiffness and D_i is a damage variable, which takes values between 0 (no damage) and 1 (complete failure). The slope of T_i-Δ_i for each fatigue cycle gives the instantaneous stiffness $k_i(1\text{-}D_i)$, which decreases due to the evolution of damage. The damage variable is the sum of the incremental damage for every cz element, recording the fatigue loading history. The tangential traction components (T_{t1} and T_{t2}) and opening components (Δ_{t1} and Δ_{t2}) compose the total tangential traction T_t and total tangential opening Δ_t), respectively:

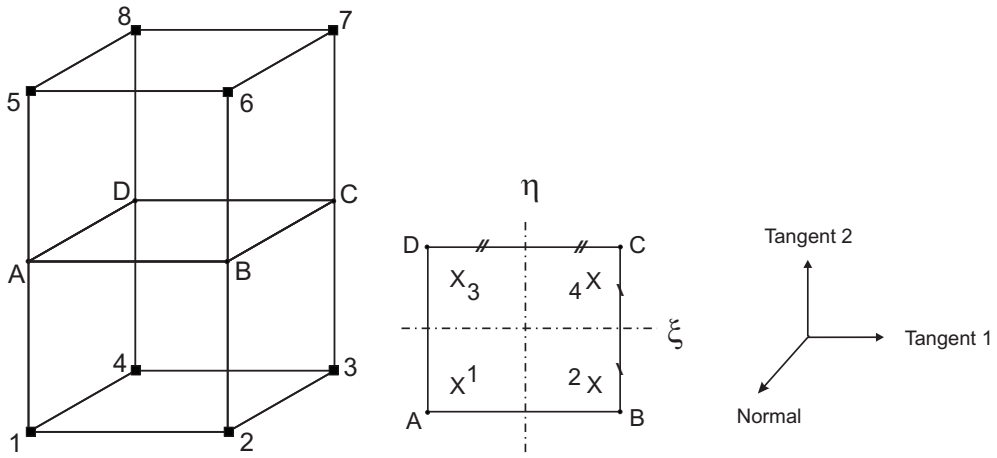

Figure 5.5: 3D cohesive zone element, the mid-plane, and local coordinate system.

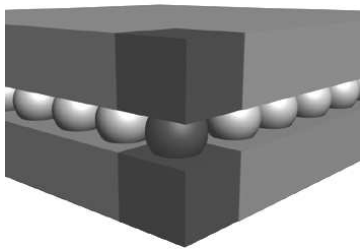

Figure 5.6: The most critical solder balls in a BGA package are the corner balls.

$$\mathrm{T_t} = (\mathrm{T_{t1}}^2 + \mathrm{T_{t2}}^2)^{\frac{1}{2}} \tag{5.2}$$

$$\Delta_\mathrm{t} = (\Delta_{\mathrm{t1}}^2 + \Delta_{\mathrm{t2}}^2)^{\frac{1}{2}} \tag{5.3}$$

The damage variable evolves according to:

$$\dot{\mathrm{D}}_{\mathrm{n,t}} = \mathrm{c_{n,t}} |\dot{\Delta}_{\mathrm{n,t}}| \left(1 - \mathrm{D_{n,t}} + \mathrm{r}\right)^{\mathrm{m_{n,t}}} \left\langle \frac{|\mathrm{T_{n,t}}|}{1 - \mathrm{D_{n,t}}} - \sigma_\mathrm{f} \right\rangle \tag{5.4}$$

where $\dot{\Delta}_{\mathrm{n,t}}$ is the rate of relative opening, σ_f is the fatigue limit, c, m and r are constants controlling the decay of the cohesive interaction.

5.3.2 The slice model

In a BGA package, the corners of the package are prone to high strains arising from CTE mismatches and warpage. It is generally observed that the corner solder balls fail first and they are therefore named 'critical solder balls'. In this section, a detailed damage analysis on the corner solder ball and the top and bottom constituents (Figure 5.6) is conducted. This repetitive part of the package is termed as a 'slice'.

The slice model is created by first making the 3D solder ball incorporating the local grain orientations and the microstructure, which is then combined with the rest of the model. As explained in Section 5.2.2, 760 μm diameter solder balls were scanned by OIM. Grain boundaries are identified as a collection of line vectors and local Euler angles. The grain boundary lines are directly transferred to the finite element geometry on the basis of which the discretization is performed.

A preliminary 3D analysis is performed on the microstructural meshes created as explained above, in order to coarsen the discretization without substantially altering the overall mechanical response. The mesh is smoothened (or filtered) on a scale of f=0-11, 0 being the original mesh, the exact representation of the OIM scan. The models are heated to 100°C homogenously, and the resulting distributions of equiva-

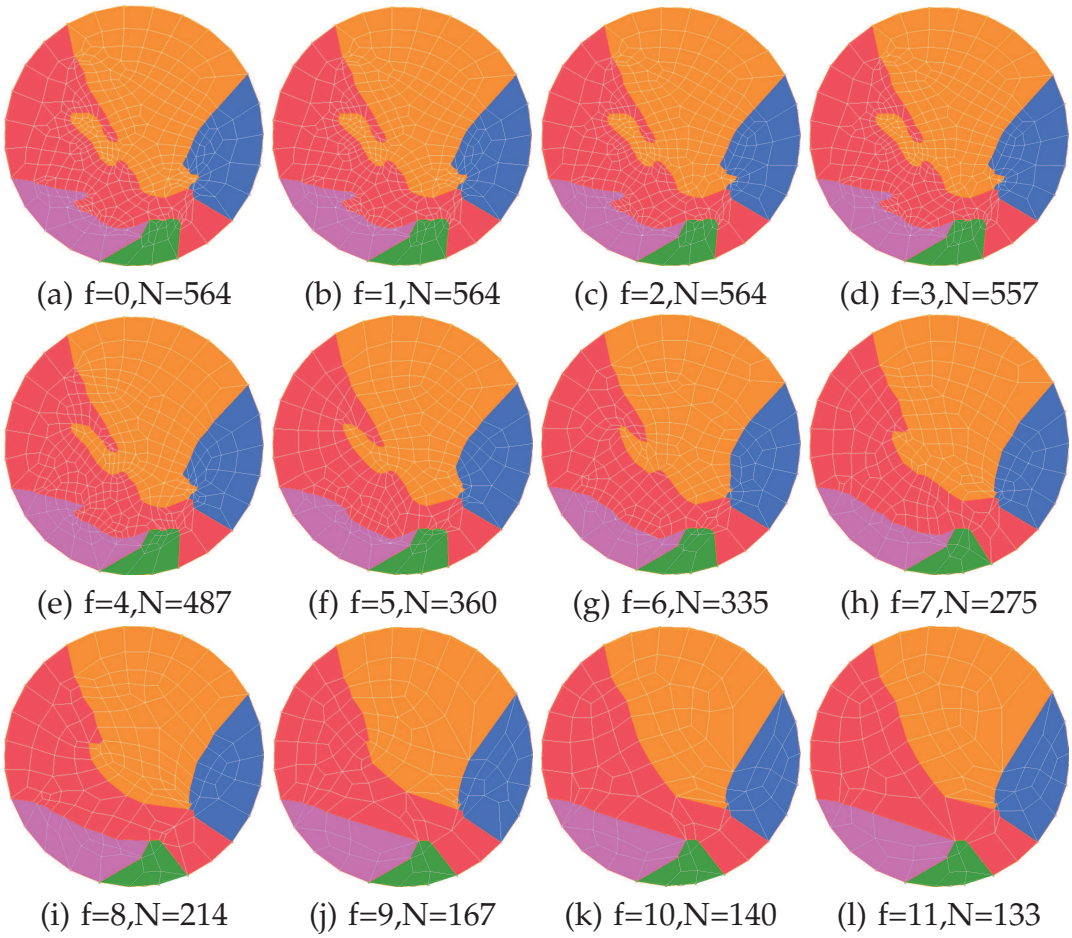

Figure 5.7: Reducing the number of elements (N) by coarsening with a factor f.

lent Von Mises stresses (σ_{vm}) are compared. The meshes and the contour plots of σ_{vm} for every mesh are shown in Figures 5.7 and 5.8, respectively. After coarsening 4 levels (f=4), the number of elements significantly reduces. Coarsening level f=6 seems to be a good compromise since at this level the details in the results are adequately captured while the number of elements is reduced by a factor 2.

The microstructure of ten solder balls is discretized from the OIM scans as explained above. The grain interiors are meshed using hexagonal elements with 8-nodes. At the grain boundaries, a thin line of cz elements is placed. Cz elements are placed such that the normal direction corresponds to the crack opening between two grains, while the two tangential directions reside in the grain boundary plane, representing grain boundary sliding. Next, solder balls having a contact angle of 120° are created from the discs. The microstructural meshes and the cz network at the grain boundaries are shown in Figure 5.9.

The crystallographic orientations were assigned to the grains after rotating the local Euler angles (ϕ, θ, ψ) in the OIM reference frame to coincide with the FEM reference frame. The OIM and FE reference frames along with the rotation matrices were given in Figure 4.10 and Eqn 4.1, respectively.

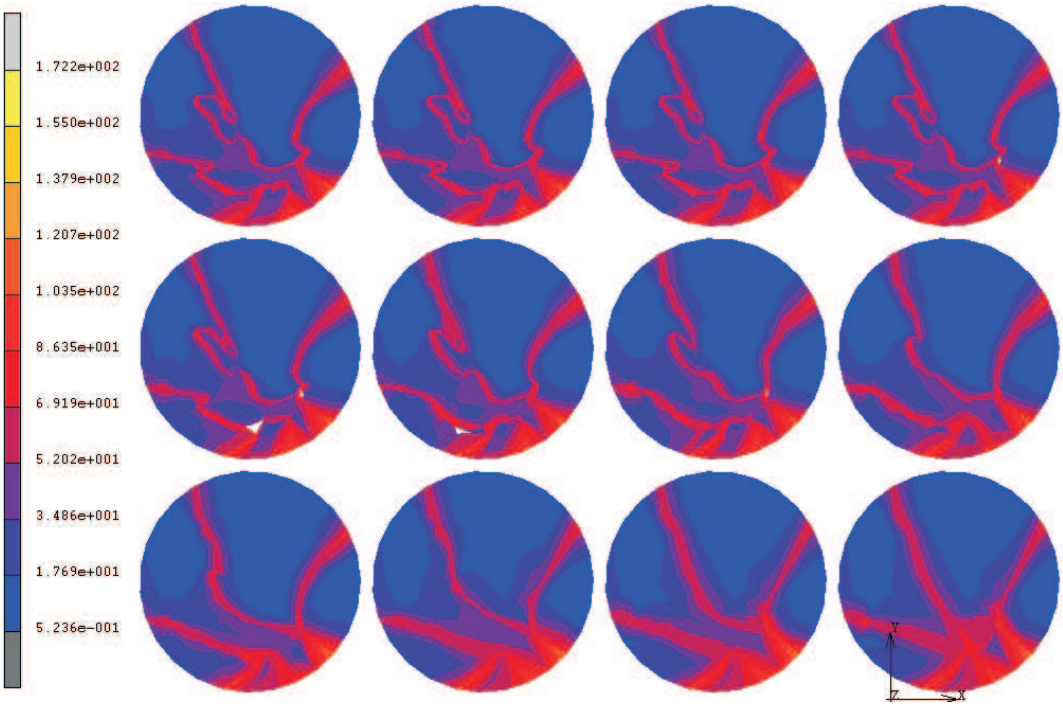

Figure 5.8: Corresponding equivalent Von Mises stress [MPa] distribution at 100°C.

The slice model is shown in Figure 5.10 consists of, top to bottom, molding compound, substrate, solder mask, metallization (UBM: copper, nickel and Ni_3Sn_4 intermetallic layer), solder ball, metallization, solder mask and the printed circuit board. The material properties are given in Table 5.3.2. SnAgCu is modeled elasto-plastically [62], combined with a steady-state creep model for bulk SnAgCu. The creep model and the parameters were given in Eqn. 3.5 [30]. Besides the grain boundary cz elements, two sets of cz elements are placed between the metallization and the solder ball on both sides, referred as bump/pad cz elements. The damage evolution parameters for the bump/pad and grain boundary cz elements are tabulated in Table 5.3.2.

The initial stiffness of the cz elements k° is calculated such that their existence (100 nm initial thickness) do not alter the initial stiffness of the slice model.

Periodic boundary conditions are applied to the slice model. A cyclic thermal loading is applied, being either thermal cycling ΔT=-40 to 125°C with a moderate temperature change rate (Figure 5.11a), or thermal shock ΔT=-55 to 125°C with a strong temperature change rate (Figure 5.11b). Each cycle is computed in 10 increments.

5.3.3 Fatigue life predictions

In Chapter 3, D_n and D_t are averaged to get an effective damage value D_{eff} according to Eqn. 3.6, repeated here:

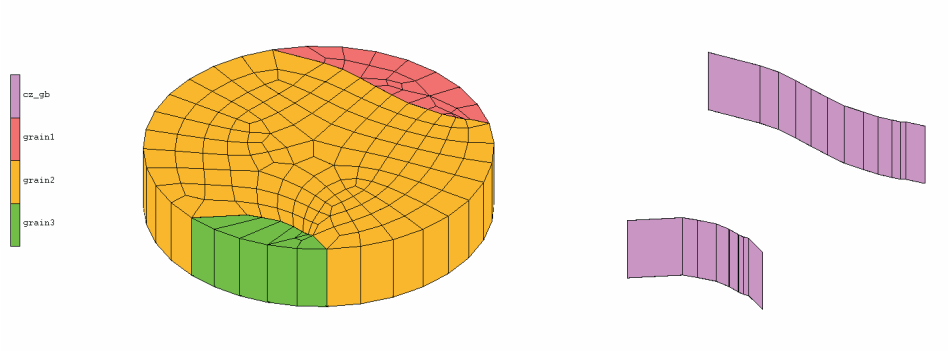

(a) Disc nr.1

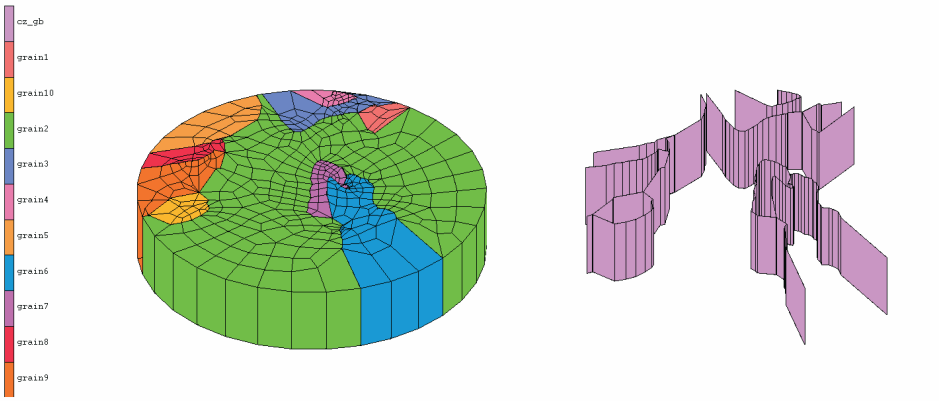

(b) Disc nr.3

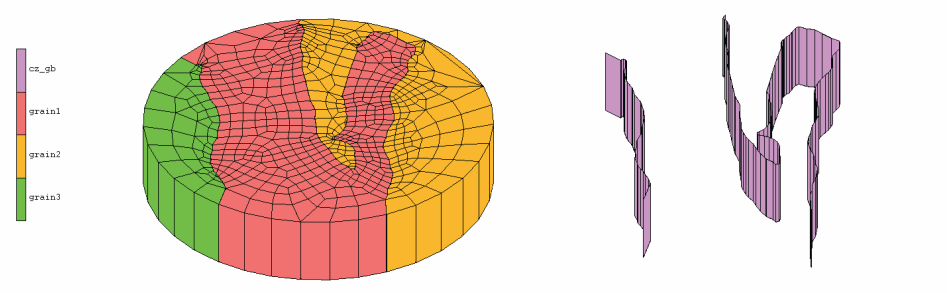

(c) Disc nr.4

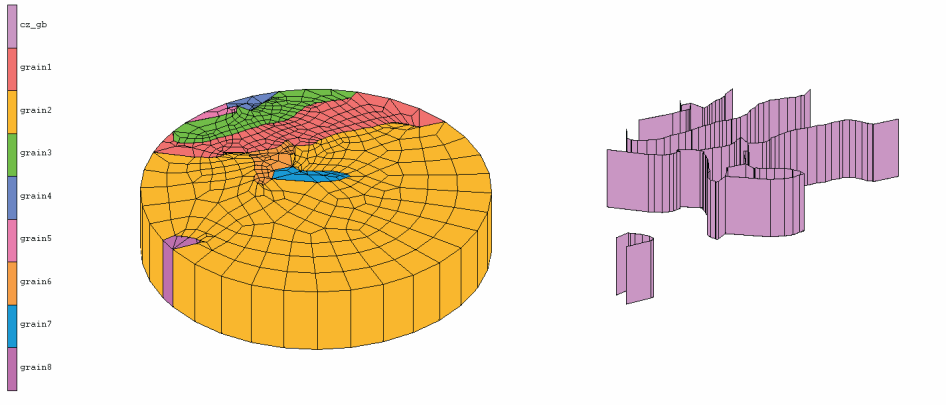

(d) Disc nr.5

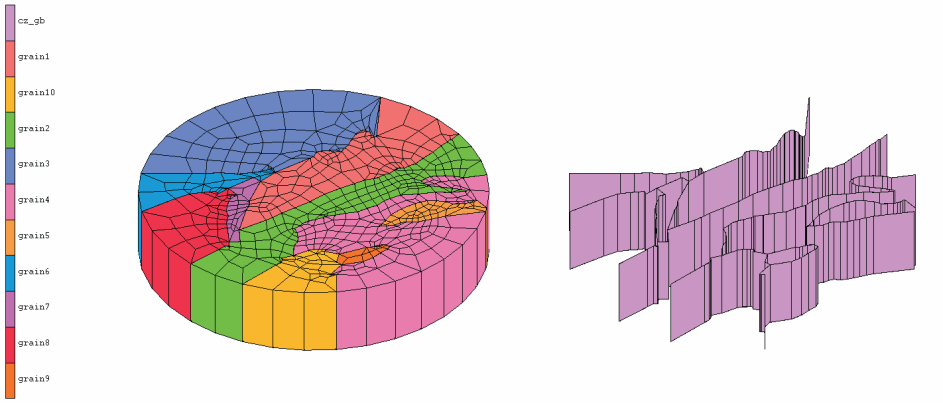

(e) Disc nr.6

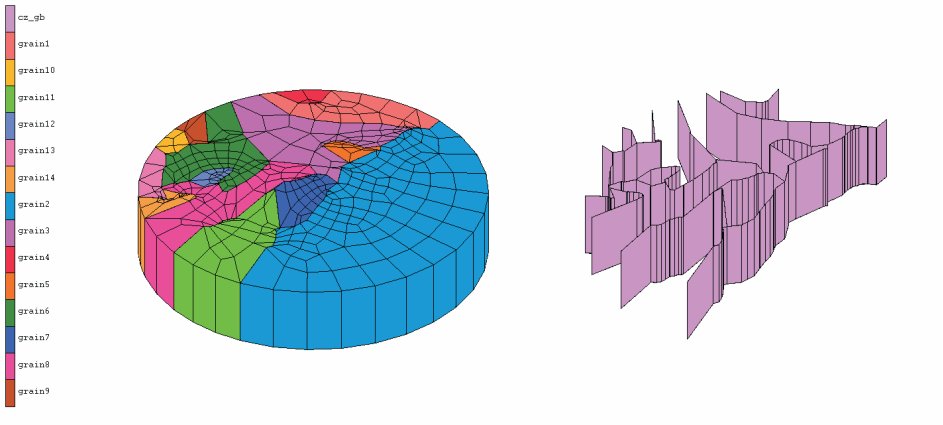

(f) Disc nr.8

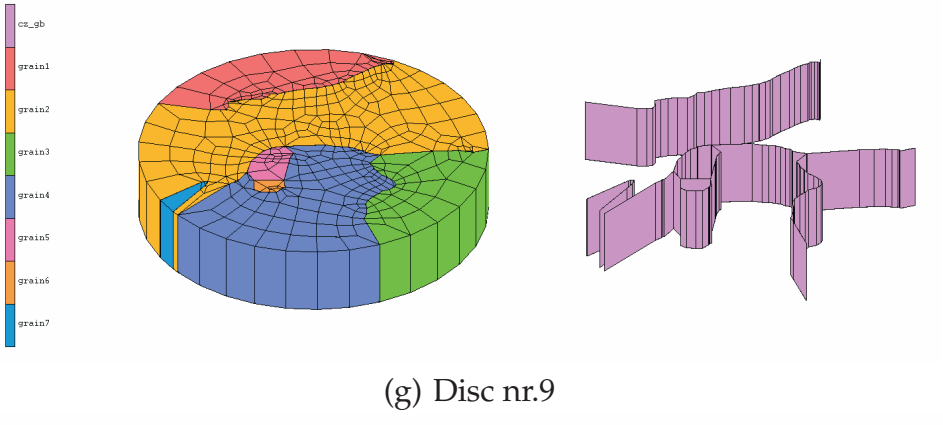

(g) Disc nr.9

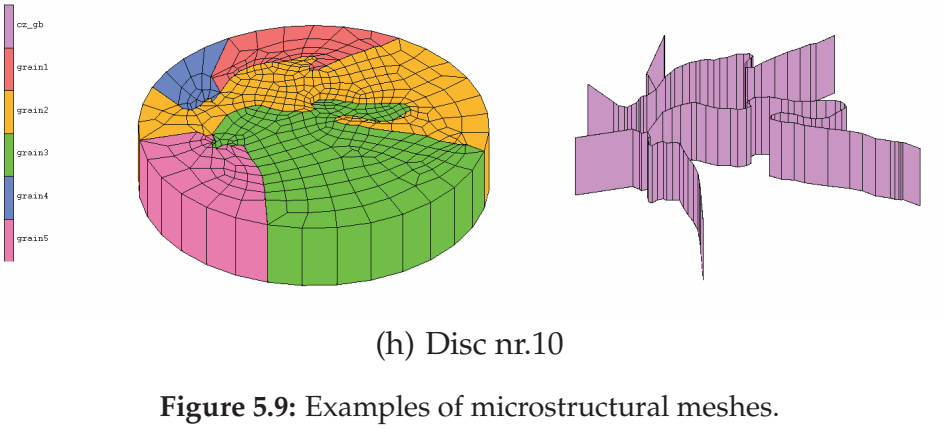

(h) Disc nr.10

Figure 5.9: Examples of microstructural meshes.

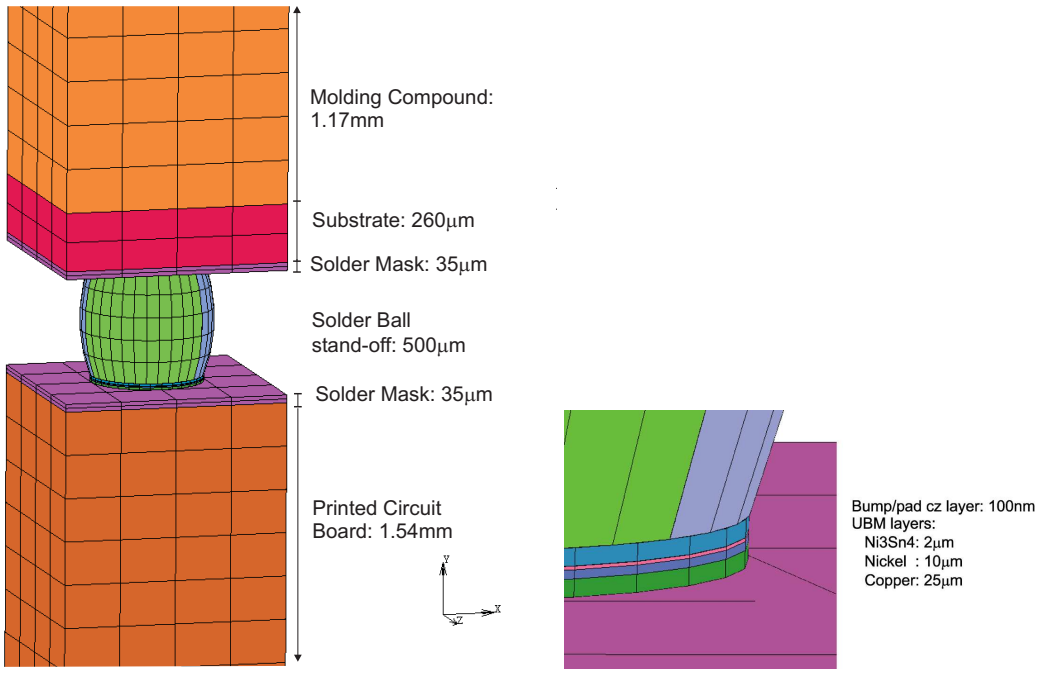

Figure 5.10: A representative slice model.

Table 5.1: Elastic material parameters and CTE values used in simulations.

Material	**E** [GPa]	ν	α [ppm/°C]
SnAgCu	64.1	0.4	[100],[110]:16.5, [001]:32.4
Cu	128	0.35	17
Ni	197	0.31	12.96
Ni_3Sn_4 [a]	140.4	0.3	14.98
PCB[b]	17.5	0.11	17.6
Moulding Compound[b]	10	0.25	16.9
Substrate[b]	1	0.11	16
Solder Mask[b]	2.412	0.467	60

[a] [45], [b] [68]

Table 5.2: Cohesive zone element parameters used in simulations.

Cz elements	**k°** [GPa]	**c**	**m**	**r**
bump/pad, normal[a]	8.79e8	68000	3.16	1e-6
bump/pad, tang.[a]	3.21e8	47000	3.135	4e-5
grain bound, normal[b]	6.4e8	42000	2.94	0
grain bound, tang.[b]	2.28e8	42000	2.94	0

[a] [61], [b] [62]

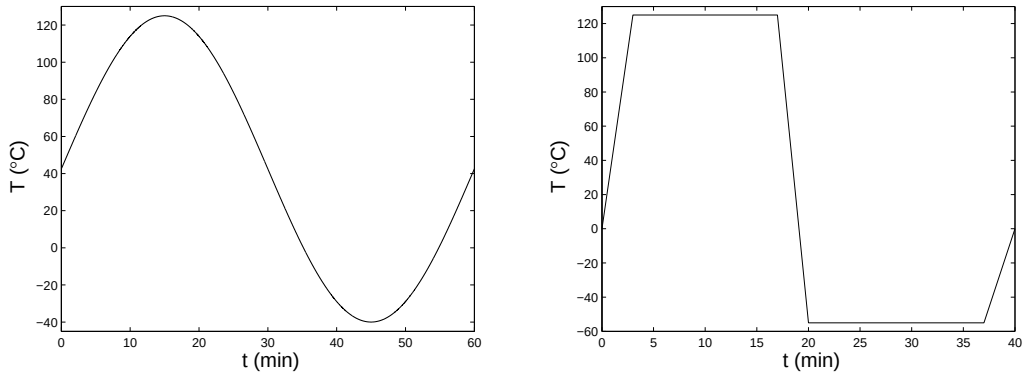

Figure 5.11: Thermal cycling (left) and thermal shock (right) loading schemes prescribed as boundary conditions in the simulations.

$$D_{eff} = (D_t^2 + D_n^2 - D_t D_n)^{\frac{1}{2}} \tag{5.5}$$

This formulation may yield unrealistic results, i.e. the effective damage can decrease during a calculation. Thus, in this paper a new formulation is proposed, given in Equation 5.6. D_{eff} is defined in the range [0 1]. The term $2/\pi$ is added to normalize D_{eff} towards unity. Values of D_n and D_t are calculated at the end of every increment for every cz element according to Equation 3.2. For low values of D_n and D_t, D_{eff} follows a circular pattern. As they approach 1, D_{eff} tends to a square pattern. At no instance D_{eff} decreases by increasing damage, nor exceeds D_n and/or D_t. The contour plots of both old and new formulations are shown in Figure 5.12. D_{eff} values for both cases are shown in Figure 5.13.

$$D_{eff} = \frac{2}{\pi} \arccos\left(\cos(\frac{\pi}{2} D_n) * \cos(\frac{\pi}{2} D_t)\right) \tag{5.6}$$

After D_{eff} is calculated for all elements, an average damage value per interface is computed by weighing D_{eff} with the element size. Figure 5.14 shows the average effective damage D_{eff}^{avg} at the interfaces, (1) top bump/pad interface, (2) bottom bump/pad interface, (3) grain boundaries. In all computations, top bump/pad interface shows the highest damage, followed closely by the bottom bump/pad interface, and least damage was observed at the grain boundaries. Damage at the grain boundaries always came to a stationary value early in the calculation in the current analyses. It was shown in Chapter 4 that, if the solder geometry is chosen such that it concentrates stresses in the solder, i.e. hourglass shape, the grain boundaries take most of the damage and eventually fail, whereas damage at the pads level-off. Thus, there is a competition between the grain boundaries and the pads favored by a specific

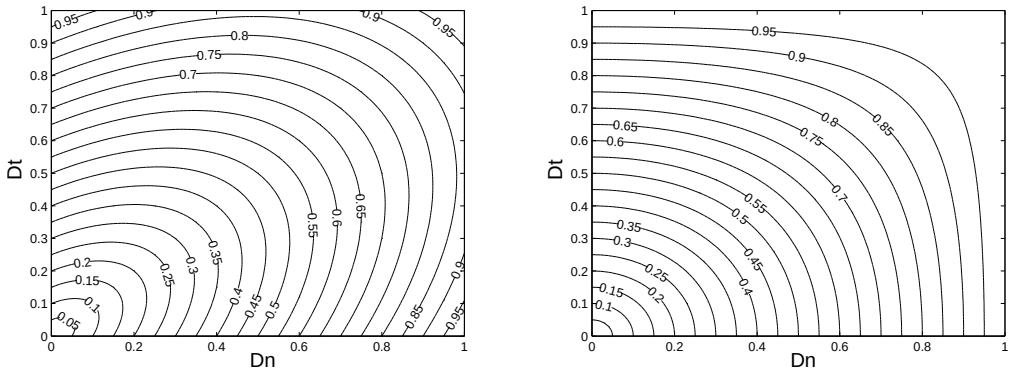

Figure 5.12: Contour plot of D_{eff} according to: Eqn 5.5 (left), Eqn 5.6 (right), where D_n is the normal damage and D_t is the tangential damage.

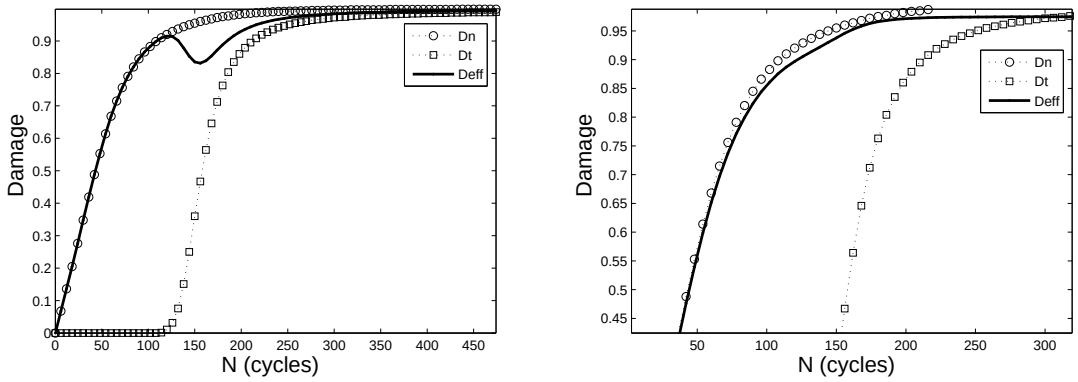

Figure 5.13: D_{eff} calculated according to Eqn 5.5 (left), Eqn 5.6 (right).

geometry. The bump shape (contact angle>90°) favors pad failure, i.e. the damage is taken mostly by the pads, and damage at grain boundaries stagnates. The fatigue limit and the plasticity in the solder relaxes stresses after a certain number of cycles, and damage evolution ceases to progress.

A calculation with N=5000 cycles takes approximately 60-70 hours of CPU time. If damage evolution can be predicted at an earlier stage in the calculation, significant amount of time can be saved, allowing to analyse a larger number of different microstructures. Damage evolution in arbitrary slice models (nr.1 and 2) are computed over N=5000 thermal cycles, the results of which are shown in Figure 5.15. In connection with the damage evolution law given in Eqn 3.2, the shape of the curve suggests an exponential evolution ($1 - e^{-a*N}$). However, a single exponential parameter cannot describe its entire span, nor is able to predict the rest of the curve at an earlier stage. A rational function of quadratic polynomials with five parameters $(p_1x^2 + p_2x + p_3)/(x^2 + q_1x + q_2)$ is used instead. As obvious from Figure 5.15, with

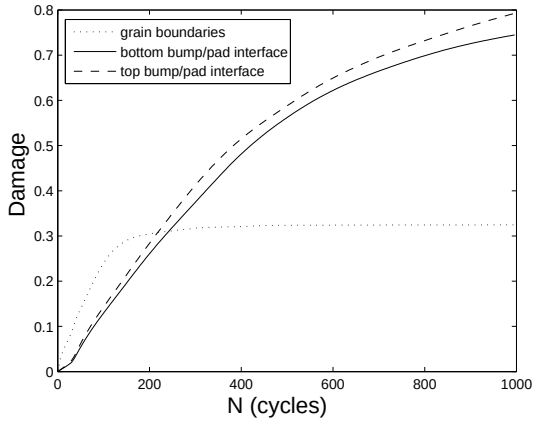

Figure 5.14: Damage at all interfaces in the slice model nr. 4 with thermal shock loading.

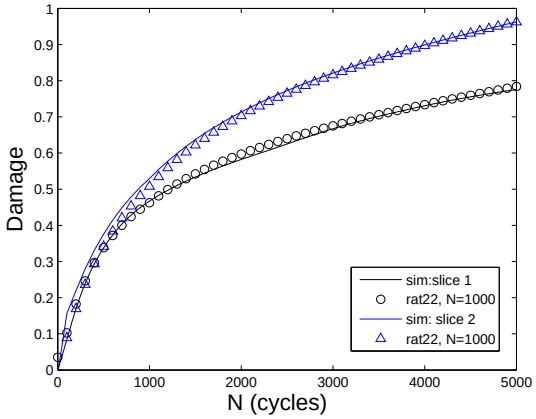

Figure 5.15: Fit of damage evolution curve by a quadratic rational function (rat22) between N=0 and N=1000 cycles, extrapolated to N=5000 cycles.

five parameters, the damage evolution curve can be described and predicted fairly well. The fitting function is fit over the simulation results between N=0 and N=1000, and how well it captures the rest of the curve is compared with the rest of the simulation results. It is concluded that, after N=1000 cycles, the curve can be predicted till N=5000 cycles. Before N=1000 cycles, the steep increase in the earlier stages gives a false over-estimate in damage evolution.

5.3.4 Validation

The simulation results are validated using an experimental analysis of BGA packages under thermal cycling and thermal shock loading. All slice models are computed separately for both types of loading, until N=1000 cycles. The numerical results are then extrapolated to N=5000 as explained in the previous section. According to Eqn 5.6, a critical effective damage value D_{eff} is defined to predict the number of cycles to failure (ncf), that adequately reproduces the experimental failure distributions provided by the industry.

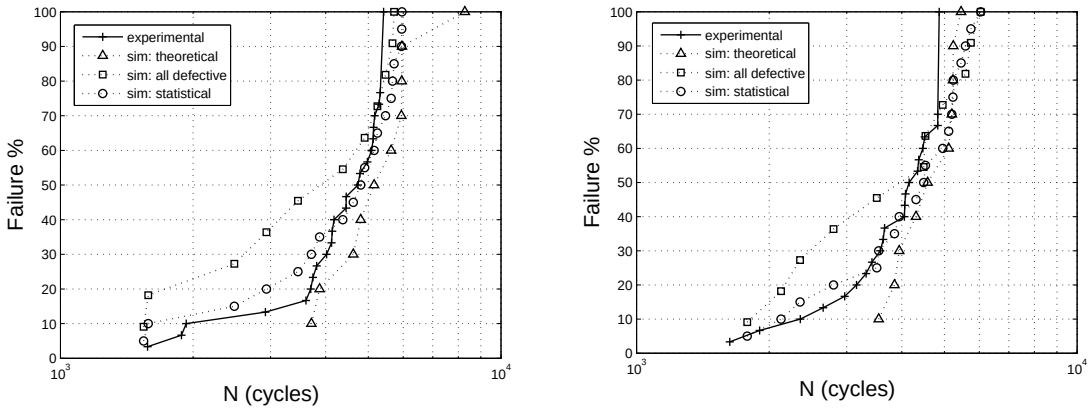

Figure 5.16: Comparison of experimental results [69] with simulations for thermal cycling (left), and thermal shock (right).

First, all slice models were computed without any defects, representing a theoretical case. Then, defects were introduced in the mesh, as they were statistically determined in Section 5.2. In the defective models, the average number of voids in a solder balls was 1.5, 80% of the voids contained a void with diameter ϕ <=50μm (74% measured), 20% of the voids contained a void with diameter ϕ <=100μm, (25% measured). Voids with a diameter larger than 100μm are not modeled (1% measured). 80% of the voids were placed at the chip side (84% measured). Last, a data set consisting of good (45%) and defective balls (55%) is constructed. Figure 5.16 shows that, with a critical damage level for failure equal to D_{eff}^{crit}=0.87, a good agreement between the statistically constructed data set and the experimental data is obtained. The fatigue life of long living (N>5000) solder balls is over-estimated. This seems logical due to the fact that, as mentioned previously, the cross-sectional defect analysis hides many defects, yielding too optimistic results (45% of all solder balls were defect-free). In reality, more defects have to be inserted into the slice models.

5.4 Conclusions

In this study, the thermomechanical reliability of lead-free BGA solder balls is investigated by microstructural modeling. Three dimensional solder joints are simulated incorporating the microstructure, local orientations and initial defects, which were not handled in the literature before. The fatigue life is determined using cohesive zone based damage models for bump/pad crack propagation and intergranular fatigue damage. It is seen that microstructural modeling allows to predict and understand the scatter in the solder ball fatigue life observed in reality. The methodology used in this study will be used to assess solder interconnect reliability under different geometrical and/or loading conditions, especially regarding the effect of miniaturization on solder reliability.

The following conclusions are drawn from the current analyses:

- Manufacturing defects in EFSOT-BGA256 packages are optically examined. 57% of all solder balls examined contained voids, on average 1.5 void per ball. 84% of all the voids observed were on the chip side. Solder balls with big voids ($>$100 μm) were rare ($<$1%). If the solder contained a void, almost half of the cases the voids volume was less than 1% of the solder ball volume.

- 760 μm SnAgCu solder balls from a single manufacturer are examined for their crystallographic structure. Approximately 20% of the solder balls were single crystal, 50% contained 2–5 grains, remaining 30% contained 6–11 grains.

- Microstructural meshes of 10 solder balls are created. At the grain boundaries and bump/pad interfaces, cohesive zone elements are placed. The thermal fatigue damage evolution at certain interfaces is monitored through these cz elements. Fatigue lives of the solder balls are predicted under thermal cycling (ΔT=-40 to 125°C), or thermal shock (ΔT=-55 to 125°C) loading.

- The numerical results are compared with experimental fatigue life analyses obtained from the industry. A critical effective damage value for failure for an interface is determined. After inserting initial defects into the models, an adequate agreement between the numerical analyses and the experimental values is achieved.

CHAPTER SIX

Impact of miniaturization on solder reliability

Abstract

The solder ball model developed in this thesis is extended in order to predict the effect of solder ball size and geometry on the interconnect reliability, which is particularly important for miniaturization. In BGA packages the pitch size is correlated to the solder ball diameter and the stand-off height. In this study, pitch size is also correlated to the contact angle between the solder and the substrate. Finite element slice models are constructed separately for five contact angles with different stand-off heights. Bump/pad interfaces and the bulk solder are analyzed by determining plastic strain accumulation and equivalent Von Mises stresses resulting from thermal loading. Geometrical and microstructural criticality are quantified by describing a geometry factor and a microstructure factor. The geometry factor is related to the shape of the solder, and the microstructure factor is related to the grain boundary area and the mismatch of local crystallographic orientations at the grain boundaries. The influence of these two factors on solder reliability is discussed.

6.1 Introduction

The ongoing miniaturization trend requires more functionality in smaller space. To this purpose, the BGA pitch size has decreased over the past years. The pitch size in traditional BGA packages is generally between 1-1.5$\times$ the pad diameter, in order to prevent short circuiting. With the same pad diameter, the pitch size can be further decreased by controlling the solder shape. Hourglass type of solder joints would clearly allow a smaller pitch size than the traditional solder bumps (Figure 6.1). Increasing the stand-off height in order to decrease the contact angle α may be a challenging task for the production units to tackle. For this reason, stacked solder bumping techniques have been developed [59, 70], where two or three solder parts are stacked together to obtain the desired geometry.

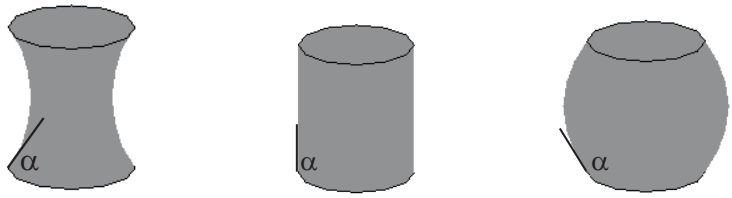

(a) Hourglass (b) Cylinder (c) Bump

Figure 6.1: Solder interconnect shapes.

The solder/substrate contact angle is a physical quantity, determined by the surface tension of the soldered components. Forcing a high stand-off in an attempt to obtain a smaller contact angle than the physically allowed minimum α will result in disconnection between the board and the chip. Unfortunately, a detailed experimental study on bump/pad contact angles for a variety of lead-free solders is not available in the literature. The contact angle of Sn-3.5Ag-1Cu solder with Kester Rosin flux at 250°C is reported as 36°, whereas with the flux %20 Rosin in isopropyl alcohol, it is 44° [71]. These values clearly show the dependence of the contact angle on the type of flux during reflow.

In this study, the pitch size is correlated to the contact angle between the solder and the substrate. Finite element slice models are constructed separately for five contact angles (30, 60, 90, 120 and 150°) with different stand-off heights. Thermal loading conditions are considered. Bump/pad interfaces and the bulk solder are analyzed by determining the plastic strain accumulation and equivalent Von Mises stresses in the horizontal cross-sections. The geometrical and microstructural criticality are quantified by describing a geometry factor and a microstructure factor. The geometry factor is related to the solder shape, whereas the microstructure factor is related to the grain boundary area and the mismatch of local crystallographic orientations at

the grain boundaries. The influence of these two factors on damage evolution is discussed in a miniaturization context.

6.2 Simulations

BGA package slice models with five different contact angles α = 30, 60, 90, 120 and 150° are created. The slice models shown in Figure 6.2 consist of, top to bottom, molding compound, solder mask, intermetallic compound, solder ball, intermetallic compound, solder mask and the printed circuit board. The UBM layers Cu/Ni(Au) are situated in the solder mask, approximating the physical reality better than the slice models shown in Section 5.3.2. The material properties are assigned as given in Table 5.3.2, except the printed circuit board. Here orthotropic elastic and thermal material properties are used, as listed in Table 6.1 [72].

Table 6.1: Orthotropic elastic material properties for the FR-4 PCB [72].

Direction	E [GPa]	ν	α [ppm]
x	25.2	0.39 (xy)	14.5
y	25.2	0.11 (yz)	14.5
z	11	0.11 (xz)	63.5

In order to separate the effect of size and geometry from the microstructure, the solder joints in the slice models are first considered as single crystals. Periodic boundary conditions are applied to (xy) and (yz) edge planes. A monotonously increasing thermal load is applied from T=25 to 125°C homogenously, in 10 increments. Two different stand-off height values are considered for all contact angles being h = 234 and 300 μm, where the solder pad diameter is fixed to 250 μm.

6.2.1 Geometrical Considerations

A geometry factor GF is next proposed allowing to compare the criticality imposed by the solder geometry (Eqn. 6.1):

$$\mathrm{GF} = \left(\frac{\mathrm{d_{mid}}}{\mathrm{h}}\right)^{\frac{1}{2}} \mathrm{V}^{-\frac{1}{3}} \tag{6.1}$$

where h is the stand-off, $\mathrm{d_{mid}}$ is the diameter of solder joint at h/2 and V is the total solder volume. According to this relationship, the GF values calculated for the several solder shapes discussed are tabulated in Table 6.2.

Unlike the previous chapters, cohesive zone elements are not used in the present

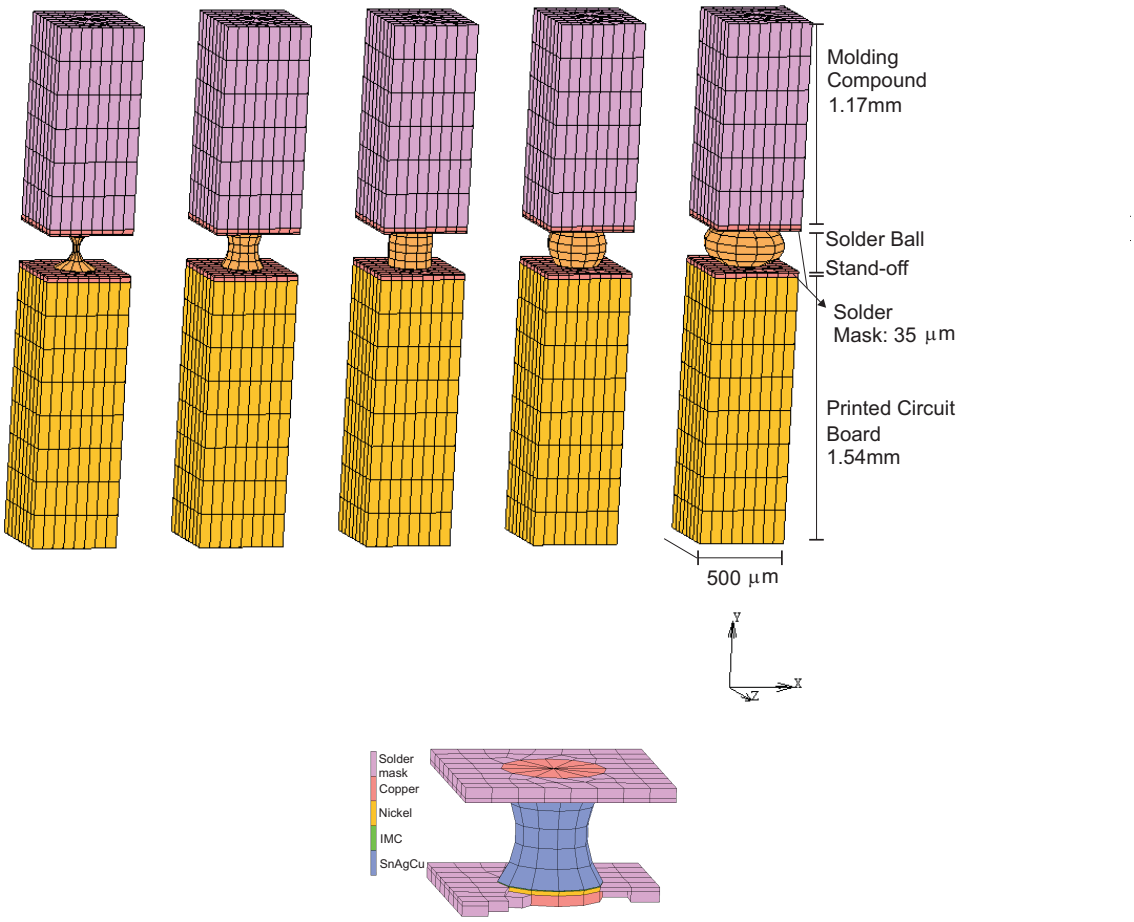

Figure 6.2: Slice models with varying contact angle, left to right: α = 30, 60, 90, 120, 150° (top), detail for α = 60° showing the UBM layers (bottom).

Table 6.2: Geometry factor of the solder joint shapes considered.

Case#	α	stand-off [μm]	Volume [e-4mm^3]	GF [norm.]
1 h.gl.	30°	234	2.9	0.9
2 h.gl.	60°	234	9.7	0.41
3 cyl.	90°	234	11.5	0.35
4 bump	120°	234	17.1	0.29
5 bump	150°	234	30.8	0.22
6 h.gl.	30°	300	3.2	1.00
7 h.gl.	60°	300	11.7	0.42
8 cyl.	90°	300	14.7	0.35
9 bump	120°	300	23.4	0.27
10 bump	150°	300	44.8	0.20

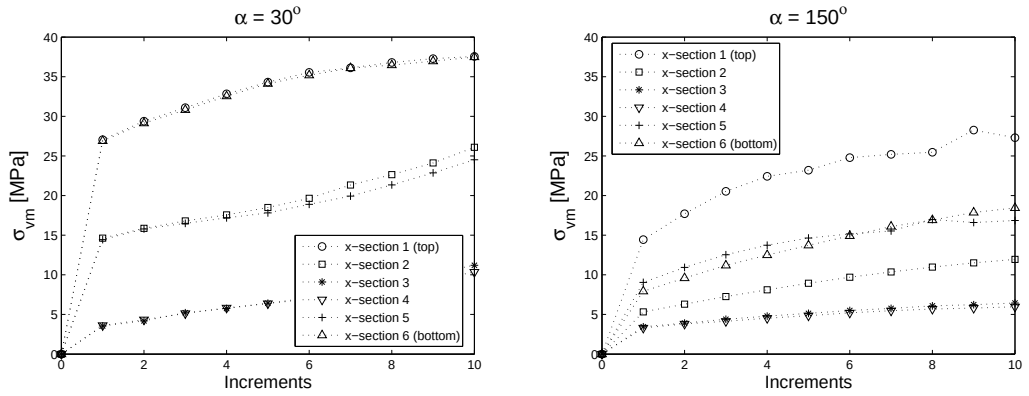

Figure 6.3: Average $\bar{\sigma}_{\text{surf}}$ at the horizontal cross-sections of case 1 (left) and case 5 (right) single crystal solder joints.

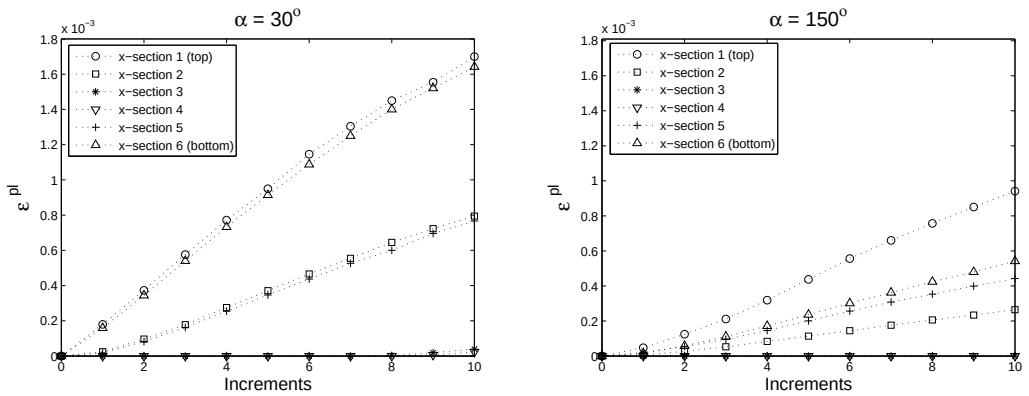

Figure 6.4: Average $\bar{\epsilon}^{\text{pl}}_{\text{surf}}$ at the horizontal cross-sections of case 1 (left) and case 5 (right) single crystal solder joints.

analysis. Instead, equivalent plastic strain and equivalent Von Mises stresses are used as damage indicators. A surface average $\bar{\epsilon}^{\text{pl}}_{\text{surf}}$ and $\bar{\sigma}_{\text{surf}}$ value is calculated for every horizontal cross-section of the solder connection, whereby the top cross-section is the top bump/pad interface, given by Eqn. 6.2:

$$\bar{\sigma}_{\text{surf}} = \frac{1}{A_{\text{surf}}} \int_{\text{surf}} \sigma_{\text{vm}}\, dA \quad , \quad \bar{\epsilon}^{\text{pl}}_{\text{surf}} = \frac{1}{\text{A}_{\text{surf}}} \int_{\text{surf}} \epsilon^{\text{pl}}\, \text{dA} \tag{6.2}$$

The $\bar{\sigma}_{\text{surf}}$ values of the two geometrical extremes (cases 1 and 5) are shown in Figure 6.3. Numerical results of the conventional bump shapes, cases 4 and 5 show that the top cross-section (x-section 1) has the highest stress. If the contact angle decreases, the average stress level in the cross-sections become nearly symmetric, i.e. cases 1,2, and 3. The $\bar{\epsilon}^{\text{pl}}_{\text{surf}}$ distribution in the cross-sections of cases 1 and 5 is

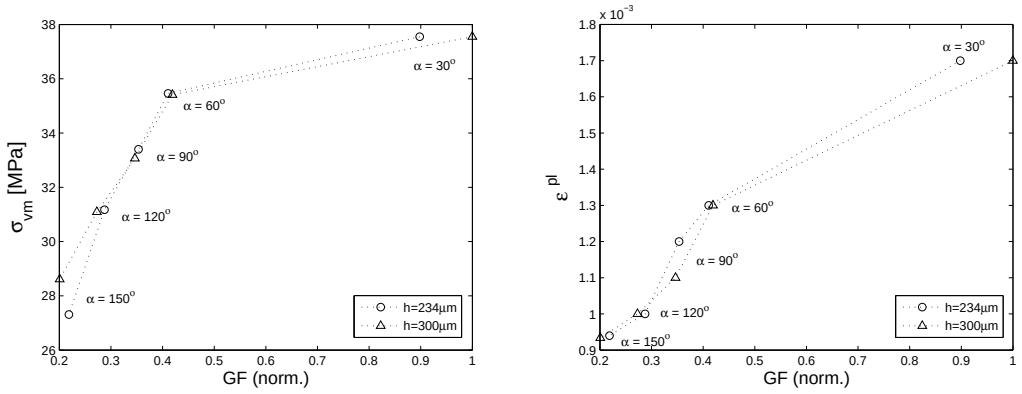

Figure 6.5: Geometry factor vs. average σ_{vm} (left), ϵ^{pl} (right) for top bump/pad interfaces, case numbers are indicated.

shown in Figure 6.4. Average plastic strains follow the same trend as the average Von Mises stresses, with respect to contact angle. In cases 6-10, where the stand-off is higher, h=300 μm, the same behavior in both stress and strain averages within the cross-sections can be noticed.

For all the cases examined, $\bar{\sigma}_{\mathrm{surf}}$ and $\bar{\epsilon}^{\mathrm{pl}}_{\mathrm{surf}}$ values for the top bump/pad interface are plotted in Figure 6.5 with respect to the geometry factor defined. The traditional solder ball shapes where $\alpha > 90°$, correspond to a geometry factor between 0 and 0.3. The GF for α = 30° is 2.2× higher than the GF for α = 60° for the smaller stand-off, and 2.4× higher for the larger stand-off. It can be concluded that decreasing the contact angle tends to be less critical as the stand-off gets shorter, keeping in mind the same contact angle gives a smaller GF with a higher stand-off. It is clearly seen that as the geometry factor increases, both plastic strain and stress values increase. The cross-sectional plastic strain is more sensitive to the geometry factor than stress, since $\bar{\epsilon}^{\mathrm{pl}}_{\mathrm{surf}}$ increases 30% from α = 60° to 30°, whereas $\bar{\sigma}_{\mathrm{surf}}$ increases only by 6%.

6.2.2 Microstructural Considerations

An idealized microstructure is implemented in the slice models of the previous section. Two grains are placed in the solder joints, one set of models with a vertical grain boundary and another set with a horizontal boundary. The grain orientations are chosen such that a maximum mismatch M=$\sqrt{2}$ is reached at the grain boundaries, as illustrated in Figure 6.6.

A microstructure factor MF is calculated to evaluate the criticality of the underlying microstructure as follows:

$$\mathrm{MF} = \sum \frac{\mathrm{A_{gb}}}{\mathrm{d} * \mathrm{h}} * \mathrm{M} \tag{6.3}$$

where $\mathrm{A_{gb}}$ is the grain boundary area, d is the pad diameter, h is the stand-off and M

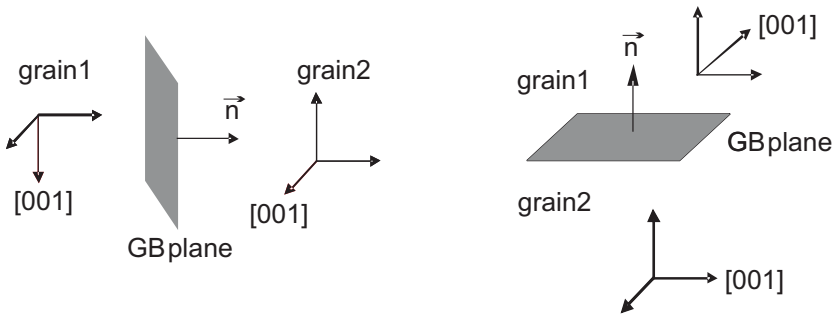

Figure 6.6: Illustration of crystallographic orientations of the grains in the slice models, left: vertical, right: horizontal grain boundaries.

Table 6.3: Microstructure factor for the solder joints considered.

		234 μm stand-off			300μm stand-off		
α	GB	Case#	GB area [e-3mm^2]	MF []	Case#	GB area [e-3mm^2]	MF []
30°	vert.	11	2.37	0.57	21	2.67	0.50
	horz.	12	0.11	0.02	22	0.06	0.01
60°	vert.	13	4.63	1.12	23	5.74	1.08
	horz.	14	2.33	0.56	24	1.98	0.37
90°	vert.	15	5.85	1.39	25	7.5	1.41
	horz.	16	4.91	1.19	26	4.91	0.93
120°	vert.	17	7.15	1.73	27	9.39	1.77
	horz.	18	8.86	2.14	28	9.65	1.82
150°	vert.	19	9.33	2.25	29	12.48	2.35
	horz.	20	16.79	4.05	30	19.86	3.75

is the mismatch factor given in Eqn. 4.3. This formulation basically sums up the area of element faces that participate in a grain boundary, multiplied by the mismatch present at that face arising from the orientation difference between the elements who share that face. For a vertical grain boundary that spans the pad diameter, MF equals only to the mismatch. The calculated microstructure factors of the models in discussion are tabulated in Table 6.3.

As emphasized in the preceding section, $\bar{\epsilon}^{\mathrm{pl}}_{\mathrm{surf}}$ and $\bar{\sigma}_{\mathrm{surf}}$ values tend to follow the same trend. Hence, only average cross-sectional Von Mises stresses will be discussed. Figure 6.7 shows the results for h=234 μm stand-off solder joints with a horizontal grain boundary with M=$\sqrt{2}$, located on x-section 3 (case 12 and case 20). In the α=30° joint, the stress level at x-section 3 is 27 MPa, which is approx. 3 times larger than the single crystal case (case 1 shown in Figure 6.3). Stress at the top bump/pad interface however is comparable to case 1. In the α=150° joint, the stress level at the grain boundary is 30 MPa, comparable with case 12. However, the total stress level in the α=150° joint is lower than α=30°, which results in the stress at the grain boundary as high as the top bump/pad interface in case 20. It can be concluded that a horizontal

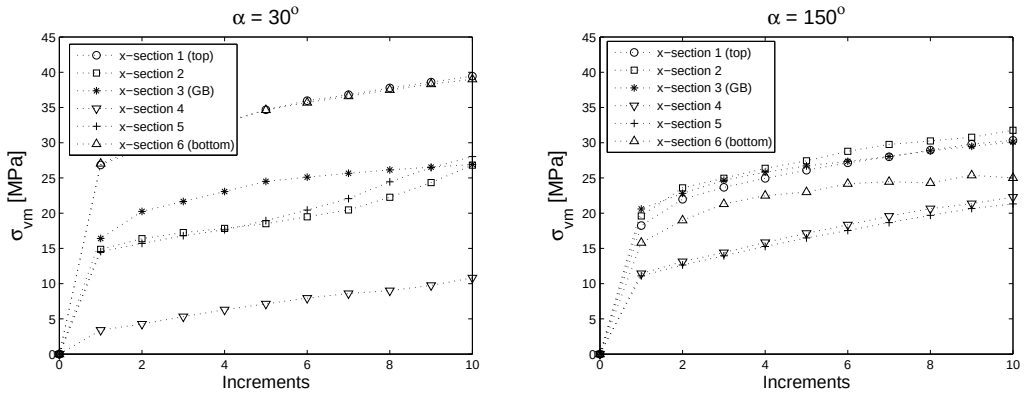

Figure 6.7: Average $\bar{\sigma}_{\mathrm{surf}}$ at the horizontal cross-sections of case 12 (left) and case 20 (right) solder joints with a M=$\sqrt{2}$ horizontal grain boundary at x-section 3.

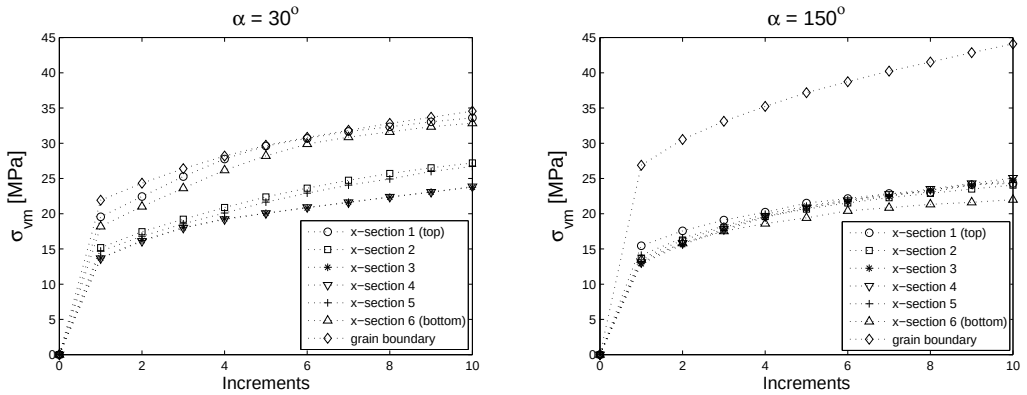

Figure 6.8: Average $\bar{\sigma}_{\mathrm{surf}}$ at the horizontal cross-sections of case 11 (left) and case 19 (right) solder joints with a M=$\sqrt{2}$ vertical grain boundary.

grain boundary becomes more critical as the contact angle increases, keeping in mind the highest stress is still at bump/pad interface with this kind of a grain boundary.

Figure 6.8 shows the results of h=234 μm stand-off solder joints with a vertical grain boundary with M=$\sqrt{2}$ (case 11 and case 19). An interesting result here is that the stress level at the grain boundary is larger than the value in all other cross-sections. In case 19, the stress level at the grain boundary is almost twice the level at the bump/pad interface. These results suggest that a vertical grain boundary has crucial importance in solder joint reliability.

The results shown in Figure 6.8 are related to the ones shown in Section 4.3.3. In Section 4.3.3, it is suggested that a grain boundary is less critical in a bump shaped joint compared to an hourglass joint, where a nearly horizontal grain boundary in a bump was compared to a diagonal boundary in an hourglass. Here it is shown that this conclusion is incomplete, since apparently apart from the mismatch and the contact angle, the grain boundary area and the position of the grain boundary with

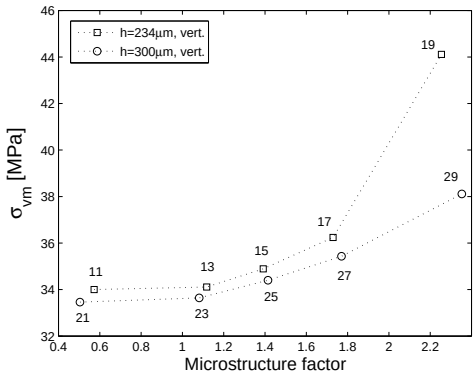

Figure 6.9: Microstructure factor vs. average $\bar{\sigma}_{\mathrm{surf}}$ on the grain boundaries, case numbers are indicated.

respect to the pad planes are also factors that affect the stress concentration. For this reason, the microstructure formulation given in Eqn. 6.3 is extended to include the grain boundary position as follows:

$$\mathrm{MF}' = \sum \frac{\mathrm{A_{gb}}}{\mathrm{d} * \mathrm{h}} * \mathrm{M} * \sin\beta \tag{6.4}$$

where β is the angle between the grain boundary normal and pad normal. In this way, a horizontal grain boundary has no effect in the total microstructure factor whereas a vertical grain boundary is fully taken into account.

In Figure 6.9, $\bar{\sigma}_{\mathrm{surf}}$ values for the grain boundaries are plotted in with respect to the microstructure factor, calculated according to Eqn. 6.4. Horizontal grain boundaries are discarded since they are not critical. The stress level on grain boundaries clearly increase with increasing microstructure factor. Smaller stand-off pronounces this effect. It can be concluded that vertical grain boundaries that touch the bump/pad interface have the highest average stress level under thermal loading and thus they constitute a possible crack initiation path.

6.3 Conclusions

With the ongoing miniaturization trend, it is a necessity to determine solder reliability with respect to size and to evaluate the increasing influence of microstructure. To this purpose, finite element slice models have been constructed for different contact angles and stand-off heights. The geometrical and microstructural criticality are quantified by describing a geometry factor and a microstructure factor. The geometry factor is related to the solder shape, and the microstructure factor is related to the grain boundary area and the mismatch of local crystallographic orientations at the grain boundaries.

From the current study, the following conclusions are drawn:

- As the geometry factor increases, cross-sectional averages of plastic strain and Von Mises stress values increase. Plastic strain is more sensitive to the geometry factor than stress.
- A horizontal grain boundary becomes more critical as the contact angle increases. However the highest stress is still at bump/pad interface, thus a horizontal grain boundary is not critical compared to the overall.
- A vertical grain boundary may play a crucial role in solder joint reliability, which becomes more pronounced as the grain boundary area increases.
- The stress level at a grain boundary increases with increasing microstructure factor. Smaller stand-off pronounces this effect.
- Vertical grain boundaries that touch the bump/pad interface have the highest stress level under thermal loading and therefore constitute a possible crack initiation path starting from the bump/pad interface.

Recommendations:
In the finite element models discussed so far, substrate warpage, or bending, is not included. Warpage is negligible in small packages. In order to make a full stress analysis for bigger packages, substrate bending has to be included as one of the boundary conditions.

In this chapter, solder reliability analysis is conducted through plastic strain accumulation and equivalent Von Mises stresses. For a complete fatigue life analysis, the cohesive zone formulation for 3D shown in Chapter 5 should be employed as well.

CHAPTER SEVEN

Conclusions

Being a promising lead-free solder alternative for the microelectronics industry, SnAgCu has been extensively studied in the past decade. However, there are still issues to be resolved concerning solder reliability, thermo-mechanical fatigue failure mechanisms, fatigue life predictions and the overall effect of decreasing component size, driven by the industrial trend of miniaturization. Concerning solder fatigue with respect to miniaturization, there is an inevitable necessity to employ local damage models rather than continuum approaches. Therefore, an in-depth study relating microstructure and fatigue damage evolution is crucial for the physical understanding of the thermo-mechanical fatigue problem in solder joints. This thesis presents a detailed microstructural analysis on SnAgCu and a coupled numerical-experimental study on solder reliability focusing mainly on the underlying microstructure.

The main conclusions of this thesis are:

- The solder/substrate interaction of SnAgCu with Cu, Ni/Au and Cu/Ni(V)/Au substrates are investigated. As a surface finishing layer on Ni based metallizations, Au film thickness of less than 1 μm is dissolves completely in the solder. In commercial BGA packages however, $AuSn_4$ formation is observed, which is known to cause 'gold embrittlement'. In order to control size of the interfacial intermetallic compounds and blowholes, an optimum laser reflow procedure is established.
- Mode I and mode II crack propagation in SnAgCu are closely related to the microstructure. Purely due to morphological reasons, solder joints are stronger in mode II type loading compared to mode I. Regarding the observed failure mechanisms, the crack propagation can be decomposed into normal and tangential components in an interfacial separation scheme.
- Nano-indentation method is employed to collect the elastic material properties of the materials relevant to solder joining. For soft metals (or alloys) like Sn

based solders, a strong influence of indentation parameters on the measured material properties is observed. Prolonging the peak hold time evokes time-dependent internal mechanisms. An assessment on indentation parameters for solders is conducted.

- Depending on the joint size and geometry, two competitive damage mechanisms are identified under thermo-mechanical fatigue loading: bump/pad interfacial crack propagation and intergranular failure. Both mechanisms are experimentally investigated and local damage models are developed by inverse modeling:

  (i) In service use, the CTE mismatch between the package components leads to cyclic thermo-mechanical strains in the solder joints. The 'bump' shape localizes these strains at the bump/pad interfaces, where the overall failure is generally observed. Since the fatigue crack paths are known in advance and the crack can be split into normal and tangential components, cohesive zones are used to simulate the fatigue crack propagation. A linear traction-separation based cohesive zone model is proposed. An interfacial damage variable is used to monitor the fatigue loading history. Using pure tensile and pure shear fatigue tests, the damage evolution parameters for the normal and the tangential openings in the cohesive zone model are identified. An adequate agreement between experimental and numerical work is established, whereby the cohesive zone approach is proven to be an effective tool in modeling solder joint fatigue failure.

  (ii) In Sn based solders, the intrinsic thermal anisotropy of β-Sn causes causes local deformations especially on the grain boundaries under cyclic thermal loading. A size dependent cyclic softening behavior is observed. The mechanical degradation of the specimens after temperature cycling is quantified from a reduction of the global elasticity modulus measured at small strains. Using OIM scans, the test specimens are simulated including the local grain orientations and the detailed microstructure. Using the developed cohesive zone law, damage evolution parameters for thermal fatigue on Sn grain boundaries are identified on the basis of the mechanical response of the thermally cycled specimens. The representativeness of the parameters is investigated by a sensitivity analysis. It is shown that the damage law characterized by experiments is capable of representing a variety of specimens which differ in grain size, orientation, and grain boundary geometry, provided that the specimen is still polycrystalline.

- Thermo-mechanical fatigue life of SnAgCu solder joints is size dependent.

- The amount of thermal fatigue damage on a Sn grain boundary is related to both the local crystallographical mismatch and the grain boundary plane, given by a 'mismatch factor'. The mismatch factor in the literature is here extended such that the crystallographically equivalent directions are also taken into account.

- Thermo-mechanical damage localization in a solder ball is closely related to the joint geometry and the amount of interfacial defects. A solder joint with a contact angle larger than 90° localizes strains at the joining interface, whereby the integrity of the bump/pad interface is more important than the microstructure in this respect. For hourglass solder joints, where the contact angle is smaller than 90°, intergranular damage might dominate over interfacial damage depending on the crystallographical state.

- Manufacturing defects in EFSOT-BGA256 packages are optically examined. 57% of all solder balls examined contained voids. 84% of all the voids observed were on the chip side. Solder balls with big voids (>100 μm) were rare (<1%). If the solder contained a void, the voids volume appeared to be less than 1% of the solder ball volume in half of the cases.

- The numerical tools presented in 2D are extended to 3D for a complete description of the industrial problem. Combining the data collected (i.e. material properties, microstructure, defects, local damage laws), 3D slice models representing critical solder balls are constructed. The fatigue life of these models are predicted and the results are validated by industrial failure distribution analyses of BGA packages. Using a critical damage value for the interfaces subjected to fatigue damage, a good agreement with the experiments and simulations is obtained. It is shown that microstructural modeling allows to predict and understand the scatter in the solder ball fatigue life observed in reality.

- The solder ball model developed so far is extended in order to predict the effect of miniaturization on interconnect reliability on the basis of numerical analyses. Finite element slice models are constructed separately for different contact angles with different stand-off heights. A geometry factor, related to the contact angle and the stand-off, and a microstructure factor, related to grain boundary area, grain boundary position and the mismatch of local crystallographic orientations at the grain boundaries are defined. The influence of these two factors on solder reliability is studied:

  (i) As the geometry factor increases, both plastic strain and stress values increase. Plastic strain is affected more by the geometry factor than stress.

  (ii) Vertical grain boundaries that touch the bump/pad interface have the highest stresses under thermal loading and thus they create a possible crack path at the bump/pad interface. Horizontal grain boundaries do not affect the overall situation.

Bibliography

[1] Allen L.A., Notis M.R., Chromik R.R., and Vinci R.P. Microstructural evolution in lead-free solder alloys: Part1, cast Sn-Ag-Cu eutectic. *Journal of Materials Research*, 19:1417–1424, 2004.

[2] Matin M.A., Vellinga W.P., and Geers M.G.D. Quantitative microscopy of microstructural evolution in eutectic solders subjected to static thermal load. In *Proceedings of EuroSimE*, Aix-en-Provence, France, 2003.

[3] Abtew M. and Seldavuray G. Lead-free solders in microelectronics. *Materials Science and Engineering R*, 27:95–141, 2000.

[4] Luo W.C., Ho C.E., Tsai J.Y., Lin Y.L., and Kao C.R. Solid-state reactions between Ni and SnAgCu solders with different Cu concentrations. *Materials Science and Engineering A*, 396:385–391, 2005.

[5] Kim K.S., Huh S.H., and Suganuma K. Effects of intermetallic compounds on properties of SnAgCu lead-free soldered joints. *Journal of Alloys and Compounds*, 352:226–236, 2003.

[6] Yoon J., Kim S., and Jung S. IMC morphology, interfacial reaction and joint reliability of Pb-free Sn-Ag-Cu solder on electrolytic Ni BGA substrate. *Journal of Alloys and Compounds*, 392:247–252, 2005.

[7] Chun H.S., Yoon J.W., and Jung S.B. Solid-state interfacial reactions between Sn3.5Ag0.7Cu solder and electroless Ni-immersion Au substrate during high temperature storage test. *Journal of Alloys and Compounds*, 439:91–96, 2007.

[8] Shih P.C. and Lin K.L. Spallation of interfacial AgAuCuZn compounds in SnAgCu/SnZnBi joints during 210^{o}C reflow. *Journal of Alloys and Compounds*, 439:137–142, 2007.

[9] Liu P.L. and J.K. Shang. Interfacial embrittlement by bismuth segregation in copper/tin-bismuth Pb-free solder interconnect. *Metall. Mater. Trans. A*, 31:286, 2000.

[10] Chan Y.C., Tu P.L., Tang C.W., K.C. Hung, and Lai K.L. Reliability studies of μ-BGA solder joints - effect of Ni-Sn intermetallic compound. *Journal of Materials Research*, 24:25–32, 2001.

[11] Liu C.Y., Tu K.N., Sheng T.T., Tung C.H., Frear D.R., and Elenius P. Electron microscopy study of interfacial reaction between eutectic SnPb and Cu/Ni(V)/Al thin-film metallization. *Journal of Applied Physics*, 87:750–754, 2000.

[12] Zeng K. and Tu K.N. Six cases of reliability study of Pb-free solder joints in electronic packaging technology. *Materials Science and Engineering R*, 38:55–105, 2002.

[13] Li M., Zhang F., Chen W.T., Zeng K., Tu K.N., Balkan H., and Elenius P. Interfacial microstructure evolution between eutectic SnAgCu solder and Al/Ni(V)/Cu thin-films. *Journal of Materials Research*, 17:1612–1621, 2001.

[14] Ratchev P., Vandevelde B., and De Wolf I. Reliability and failure analysis of Sn-Ag-Cu solder interconnections for PSGA packages on Ni/Au surface finish. *IEEE Transactions On Device And Materials Reliability*, 4:5–10, 2004.

[15] Li D., Liu D., and Conway P.P. Characteristics of intermetallics and micromechanical properties during thermal ageing of SnAgCu flip-chip solder interconnects. *Materials Science and Engineering A*, 391:95–103, 2005.

[16] Erinc M., Schreurs P.J.G., Zhang G.Q., and Geers M.G.D. Characterization and fatigue damage simulation in SAC solder joints. *Microelectronics Reliability*, 44:1287–1292, 2004.

[17] Deng X., Chawla N., Chawla K.K., and Koopman M. Deformation behavior of (Cu, Ag)Sn intermetallics by nanoindentation. *Acta Materialia*, 52:4291–4303, 2004.

[18] Chromik R.R., Vinci R.P., Allen S.L., and Notis M.R. Nanoindentation measurements on Cu-Sn and Ag-Sn intermetallics formed in Pb-free solder joints. *Journal of Materials Research*, 18:2251, 2003.

[19] Rhee H., Lucas J.P., and Subramanian K.N. Micromechanical characterization of thermomechanically fatigued lead-free solder joints. *Journal of Materials Science: Materials in Electronics*, 13:477–484, 2003.

[20] Liu H., Basaran C., Cartwright A.N., and Casey W. Application of moire interferometry to determine strain fields and debonding of solder joints in BGA packages. *IEEE Transactions on Components and Packaging Technologies*, 27:217–223, 2004.

[21] Stout E.A., Sottos N.R., and Skipor A.F. Mechanical characterization of plastic ball grid array package flexure using moire interferometry. *IEEE Transactions on Advanced Packaging*, 23:637–645, 2000.

[22] Drexler S.E. Plastic strain in thermally cycled flip-chip PBGA solder bumps. *IEEE Transactions on Advanced Packaging*, 23:646–651, 2000.

[23] Oliver W.C. and Pharr G.M. An improved technique for determining hardness and elastic modulus using load and displacement sensing indentation experiments. *Journal of Materials Research*, 7:1564, 1992.

[24] Matin M.A. *Microstructure evolution and thermo-mechanical fatigue of solder materials*. PhD thesis, Technische Universiteit Eindhoven, 2005.

[25] Sharif A. and Chan Y.C. Interfacial reactions of Sn-3.5%Ag and Sn-3.5%Ag-0.5%Cu solder with electroless Ni/Au metallization during multiple reflow cycles. *Journal of Materials Science: Materials in Electronics*, 16:153–158, 2005.

[26] Erinc M., Schreurs P.J.G., Zhang G.Q., and M.G.D. Geers. Microstructural damage analysis of SnAgCu solder joints and an assessment on indentation procedures. *Journal of Materials Science: Materials in Electronics*, 16:93–100, 2005.

[27] Zeng K., Vuorinen V., and Kivilahti J.K. Interfacial reactions between lead-free SnAgCu solder and Ni(P) surface finish on PWBs. *IEEE Transactions on Electronics Packaging Manufacturing*, 25:162–167, 2002.

[28] Plumbridge W.J., Gagg C.R., and Peters S. The creep of leadfree solders at elevated temperatures. *Journal of Electronic Materials*, 30:1178–1183, 2001.

[29] Wiese S., Feustel F., and Meusel E. Characterisation of constitutive behaviour of SnAg, SnAgCu and SnPb solder in flip chip solder joints. *Sensors and Actuators A*, 99:188–193, 2002.

[30] Wiese S. and Wolter K.J. Microstructure and creep behaviour of eutectic SnAg and SnAgCu solders. *Microelectronics Reliability*, 44:1923–1931, 2004.

[31] Lin C.K. and Chu D.Y. Creep rupture of lead-free Sn-3.5Ag and Sn-3.5Ag-0.5Cu solders. *Journal of Materials Science: Materials in Electronics*, 16:355–365, 2005.

[32] Lee W.W., Nguyen L.T., and Selvaduray G.S. Solder joint fatigue models: review and applicability to chip scale packages. *Microelectronics Reliability*, 40:231–244, 2000.

[33] Towashiraporn P., Subbarayan G., and Desai C.S. A hybrid model for computationally efficient fatigue fracture simulations at microelectronic assembly interfaces. *International Journal of Solids and Structures*, 42:4468–4483, 2005.

[34] GOM GmbH. *Aramis v 5.3.0 User's Manual*, 2004.

[35] *Metals Handbook*, volume 8: Mechanical Testing, Fatigue Testing. Metals Park, Ohio: American Society for Metals, 9th edition, 1978-1989. pp:361–437.

[36] Visser J.W.W. Microstructure and deformation analysis of lead-free solder joints. Technical Report MT02.12, Technische Universiteit Eindhoven, 2002.

[37] Dugdale D.S. Yielding in steel sheets containing slits. *Journal of the Mechanics and Physics of Solids*, 8:100–104, 1960.

[38] Barenblatt G.I. The mathematical theory of equilibrium cracks in brittle fracture. *Advances in Applied Mechanics*, 7:55–129, 1962.

[39] Needleman A. An analysis of decohesion along an imperfect interface. *International Journal of Fracture*, 42:21–40, 1990.

[40] Foulk J.W., Allen D.H., and Helms K.L.E. A model for predicting the damage and environmental degradation dependent life of SCS-6/Timetal21S$[0]_4$ metal matrix composite. *Mechanics of Materials*, 29:53–68, 1998.

[41] De-Andres A., Perez J.L., and Ortiz M. Elastoplastic finite element analysis of three-dimensional fatigue crack growth in aluminum shafts subjected to axial loading. *International Journal of Solids and Structures*, 36:2231–2258, 1999.

[42] Roe K.L. and Siegmund T. An irreversible cohesive zone model for interface fatigue crack growth simulation. *Engineering Fracture Mechanics*, 70:209–232, 2003.

[43] Abdul-Baqi A., Schreurs P.J.G., and Geers M.G.D. Fatigue damage modeling in solder interconnects using a cohesive zone approach. *International Journal of Solids and Structures*, 42:927–942, 2005.

[44] Chaboche J.L., Feyel F., and Monerie Y. Interface debonding models: a viscous regularization with a limited rate dependency. *International Journal of Solids and Structures*, 38:3127–3160, 2001.

[45] Jang G.Y., Lee J.W., and Duh J.G. The nanoindentation characteristics of Cu_6Sn_5, Cu_3Sn, and Ni_3Sn_4 intermetallic compounds in the solder bump. *Jounal of Electronics Materials*, 33:1103–1110, 2004.

[46] Laurila T., Vuorinen V., and Kivilahti J.K. Interfacial reactions between lead-free solders and common base materials. *Materials Science and Engineering R*, 49:1–60, 2005.

[47] Matin A., Coenen E.W.C., Vellinga W.P., and Geers M.G.D. Correlation between thermal fatigue and thermal anisotropy in a Pb-free solder alloy. *Scripta Materialia*, 53:927–932, 2006.

[48] Subramanian K.N. and Lee J.G. Effect of anisotropy of tin on thermomechanical behavior of solder joints. *Journal of Materials Science: Materials in Electronics*, 15:235–240, 2004.

[49] Telang A.U., Bieler T.R., Lucas J.P., Subramanian K.N., Lehman L.P., Xing Y., and Cotts E.J. Grain-boundary character and grain growth in bulk tin and bulk lead-free solder alloys. *Journal of Electronic Materials*, 33:1412–1423, 2004.

[50] Vianco P.T., Rejent J.A., and Kilgo A.C. Creep behavior of the ternary 95.5Sn-3.9Ag-0.6Cu solder: Part ii–aged condition. *Journal of Electronic Materials*, 33:1473–1484, 2004.

[51] Erinc M., Schreurs P.J.G., and M.G.D. Zhang. A coupled numerical and experimental study on thermo-mechanical fatigue failure in SnAgCu solder joints. *Proceedings in EuroSimE, London*, 2007.

[52] De Vries J.W.C., Jansen M.Y., and Van Driel W.D. The effect of board stiffness on the solder-joint reliability of HVQFN-packages. In *Proceedings of EuroSimE*, London, England, 2007.

[53] Telang A.U., Bieler T.R., and Crimp M.A. Grain boundary sliding on near-7°, 14°, and 22° special boundaries during thermomechanical cycling in surface-mount lead-free solder joint specimens. *Materials Science and Engineering A*, 421:22–34, 2006.

[54] Pearson W.B. *A handbook of lattice spacings and structure of metals and alloys*, volume 2. Pergamon Press, London, 1958.

[55] Lea C. *A Scientific Guide to Surface Mount Technology*. Electrochemical Publications Ltd., GB-Port Erin, British Isles, 1988.

[56] Lewis W.R. *Notes on Soldering*. Tin Research Institute, 1961.

[57] Matin M.A., Vellinga W. P., and Geers M.G.D. Aspects of coarsening in eutectic SnPb. *Acta Materialia*, 52:3475–3482, 2004.

[58] Ubachs R.L.J.M., Schreurs P.J.G., and Geers M.G.D. Elasto-viscoplastic nonlocal damage modelling of thermal fatigue in anisotropic lead-free solder. *Mechanics of Materials*, 39:685–701, 2007.

[59] Liu X., Xu S., Lu G.Q., and Dillard D.A. Stacked solder bumping technology for improved solder joint reliability. *Microelectronics Reliability*, 41:1979–1992, 2001.

[60] Lee H.T., Lin H.S., Lee C.S., and Chen P.W. Reliability of Sn-Ag-Sb lead-free solder joints. *Materials Science and Engineering A*, 407:36–44, 2005.

[61] Erinc M., Schreurs P.J.G., and Geers M.G.D. Integrated numerical-experimental analysis of interfacial fatigue fracture in SnAgCu solder joints. *International Journal of Solids and Structures*, 44:5680–5694, 2007.

[62] Erinc M., Schreurs P.J.G., and Geers M.G.D. Intergranular thermal fatigue damage evolution in snagcu lead-free solder joints. *Mechanics of Materials, submitted*, 2007b.

[63] Tchankov D., Sakane M., Itoh T., and Hamada N. Crack opening displacement approach to assess multiaxial low cycle fatigue. *International Journal of Fatigue*, in press, 2007.

[64] Desai C.S., Basaran C., Dishong T., and Prince J.L. Thermomechanical analysis in electronic packaging with unified constitutive model for materials and joints. *IEEE Transactions on Components, Packaging, and Manufacturing Technology – Part B*, 21:87–97, 1998.

[65] Li X. and Wang Z. Thermo-fatigue life evaluation of SnAgCu solder joints in flip chip assemblies. *Journal of Materials Processing Technology*, 18:6–12, 2007.

[66] Tee T.Y., Ng H.S., Yap D., Baraton X., and Zhong Z. Board level solder joint reliability modeling and testing of TFBGA packages for telecommunication applications. *Microelectronics Reliabilty*, 43:1117–1123, 2003.

[67] Zhang X., Kripesh V., Chai T.C., Tan T.C., and Pinjala D. Board level solder joint reliability analysis of a fine pitch Cu post type wafer level package (WLP). *Microelectronics Reliability*, in press, 2007.

[68] Lai Y.S., Wang T.H., and Lee C.C. Thermal-mechanical coupling analysis for coupled power and thermal cycling reliability of chip-scale packages. In *Proceedings of EuroSimE*, Berlin, Germany, 2005.

[69] De Vries J.W.C., Jansen M.Y., and Van Driel W.D. On the difference between thermal cycling and thermal shock testing for board level reliability of soldered interconnections. *Journal of Microelectronics & Reliability*, 47:444–449, 2007.

[70] Yeung B.H. and Lee T.T.T. Evaluation and optimization of package processing, design, and reliability through solder joint profile prediction. In *Proceedings of 51^{st} ECTC*, 2001.

[71] National Institute of Standards and Technology. www.metallurgy.nist.gov/solder/clech/Sn-Ag-Cu_Fit.htm, 2007.

[72] Towashiraporn P., Subbarayan G., McIlvanie B., Hunter B.C., Love D., and Sullivan B. The effect of model building on the accuracy of fatigue life predictions in electronic packages. *Microelectronics Reliability*, 44:115–127, 2004.

[73] Armin R. *The Basics of Soldering*. John Wiley & Sons, 1993.

[74] Frear D.R. The mechanical behavior of interconnect materials for electronic packaging. *Journal of Metals*, 48:49–53, 1996.

[75] Guo F., Choi S., Subramanian K.N., Bieler T.R., Lucas J.P., Achari A., and Paruchuri M. Evaluation of creep behavior of near-eutectic Sn-Ag solders containing small amount of alloy additions. *Materials Science and Engineering A*, 351:190–199, 2003.

[76] Kariya Y., Morihata T., Hazawa E., and Otsuka M. Assessment of low-cycle fatigue life of Sn-3.5mass%Ag-X(X=Bi or Cu)alloy by strain range partitioning approach. *Journal of Electronic Materials*, 30:1184–1189, 2001.

[77] Kempf B., Graff M., Hutin O., and Rettenmayr M. Lead-free Ball-Grid-Array balls: Production method and properties. *Journal of Electronic Materials*, 31:1270–1275, 2002.

[78] Kim H.K., Tu K.N., and Totta P.A. Ripening-assisted asymmetric spalling of Cu-Sn compound spheroids in solder joints on Si wafers. *Applied Physics Letters*, 68:2204, 1996.

[79] Lee H.T., Chen M.H., Jao H.M., and Liao T.L. Influence of interfacial intermetallic compound on fracture behavior of solder joints. *Materials Science and Engineering A*, 358:134–141, 2003.

[80] Liu X. *Processing and Reliability Assessment of Solder Joint Interconnection for Power Chips*. PhD thesis, Virginia Polytechnic Institute and State University, 2001.

[81] Liu A.A., Kim H.K., and Tu K.N. Spalling of Cu_6Sn_5 spheroids in the soldering reaction of eutectic SnPb on Cr/Cu/Au thin films. *Journal of Applied Physics*, 80:2774, 1996.

[82] Poon N.M., Wu C.M.L., Lai J.K.L., and Chan Y.C. Residual shear strength of Sn-Ag and Sn-Bi lead-free SMT joints after thermal shock. *IEEE Transactions on Advanced Packaging*, 23:708–714, 2000.

[83] Spraul M., Nuchter W., Moller A., Wunderle B., and Michel B. Reliability of SnPb and Pb-free flip chips under different test conditions. *Microelectronics Reliability*, 47:252–258, 2007.

[84] Stam F.A. and Davitt E. Effects of thermomechanical cycling on lead and lead-free (SnPb and SnAgCu) surface mount solder joints. *Microelectronics Reliability*, 41:1815–1822, 2001.

[85] Suganuma K. and Nakamura Y. Microstructure and strength of interface between Sn-Ag eutectic solder and Cu. *Journal of Japanese Institute of Metals*, 59:1299–1305, 1995.

[86] Van den Bosch M.J., Schreurs P.J.G., and Geers M.G.D. An improved description of the exponential Xu and Needleman cohesive zone law for mixed-mode decohesion. *Engineering Fracture Mechanics*, 73:1220–1234, 2006.

[87] Vandevelde B., Gonzalez M., Limaye P., Ratchev P., and Beyne E. Thermal cycling reliability of SnAgCu and SnPb solder joints: A comparison for several IC-packages. *Microelectronics Reliability*, 47:259–265, 2007.

[88] Yu D.Q., Zhao J., and Wang L. Improvement on the microstructure stability, mechanical and wetting properties of Sn-Ag-Cu lead-free solder with the addition of rare earth elements. *Journal of Alloys and Compounds*, 376:170–175, 2004.

Samenvatting

Volgens de EU-norm, opgesteld door de Electrical and Electronic Equipment Directive (WEEE) en de Restriction of Hazardous Substances Directive (RoHS), is het gebruik van lood in electronische apparaten niet meer toegestaan vanaf 1 juli 2006. In soldeerverbindingen wordt de PbSn-soldeer daarom vervangen door een SnAgCu-legering, die een stabiele microstructuur heeft met goede kruip- en vermoeiingseigenschappen. Hoewel er de afgelopen tien jaar veel onderzoek is gedaan naar de eigenschappen van SnAgCu, bestaan er nog steeds onduidelijkheden ten aanzien van de te verwachten levensduur van de soldeerverbindingen, waarin ze worden toegepast, vooral in samenhang met de steeds verdergaande miniaturisatie. In dit proefschrift wordt beschreven hoe via een gekoppelde experimenteel-numerieke werkwijze, de mechanismen bij thermo-mechanisch bezwijken zijn onderzocht.

In de micro-electronica bestaat de soldeerverbinding bij zogenaamde Ball Grid Arrays (BGA's) uit een soldeer *bump* tussen verbindingsplaatsen (*pads*) op chip en Printed Circuit Board (PCB). De betrouwbaarheid van de soldeerverbinding wordt vooral bepaald door de metallisatie van en de defecten in het overgangsgebied (interface) tussen *bump* en *pad*. Om dit te onderzoeken zijn oldeerbumps, soldeerpasta en gegoten eutectisch SnAgCu aangebracht op een Cu, Ni/Au en Cu/Ni(V)/Au metallisatie. De invloed van dit substraat op de metallurgie van soldeer en interface is onderzocht, evenals de voortplanting van defecten in SnAgCu-soldeerverbindingen op Cu en Ni/Au metallisatie. Het belangrijkste bezwijkmechanisme bleek localisatie van schade in de bump/pad interface, zodat geconcludeerd kon worden dat een continuumsmodel niet geschikt is voor bestudering van het fenomeen. De mechanische eigenschappen van SnAgCu zijn gekarakteriseerd met nano-indentatie experimenten en trekproeven. De invloed van de Ag concentratie op deze eigenschappen is onderzocht.

Een van de belangrijkste oorzaken van het bezwijken van BGA's, namelijk scheurvoortplanting tijdens wisselende thermo-mechanische belasting, wordt vrijwel altijd waargenomen in de bump/pad interface. Dit thermo-mechanisch vermoeiingsgedrag van SnAgCu/Ni-Au verbindingen is daarom nader onderzocht. Allereerst zijn vermoeiingsexperimenten uitgevoerd om de evolutie van defecten in de bump/pad interface te karakteriseren. Schade bleek op te treden zowel in het soldeermateriaal

van de bump als in de bump/pad interface. Bezwijken van de interface trad meestal op bij grote initiële spanningen en bij geringe soldeer volumes. Scheurvoortplanting werd vervolgens gesimuleerd met een *cohesive zone* model, waarbij de interactie kracht tussen twee punten aan beide zijden van de interface lineair gerelateerd wordt aan hun relatieve verplaatsing (=opening van de interface). De stijfheid in normale en tangentiële richting wordt door wisselende belasting gereduceerd m.b.v. een schadeparameter, waarvan de toename – van 0 (geen schade) tot 1 (volledig bezwijken) – beschreven wordt door een schade-evolutievergelijking. De schadegroeiparameters in deze relatie zijn bepaald door fitten van experimentele en numerieke resultaten.

Bij wisselende temperatuurbelasting ontstaat schade in de bump/pad interface t.g.v. het verschil in thermische uitzettingscoëfficiënt van de diverse materialen. In het soldeermateriaal zelf veroorzaakt de anisotropie in thermische eigenschappen van de Sn β-fase lokale deformaties in de kristalgrenzen, die resulteren in thermische vermoeiingsschade. Om dit nader te onderzoeken zijn SnAgCu-proefstukken herhaald verwarmd tot 125^o C en afgekoeld tot -40^o C. Daarna werden ze onderworpen aan mechanische belasting om via metingen van de stijfheid de vermoeiingsschade te karakteriseren. Het verband tussen kracht en verlenging tijdens een trekproef liet verzwakkend materiaalgedrag (*softening*) zien, dat afhankelijk bleek te zijn van de proefstuk geometrie (*scale effect*). Van alle proefstukken is een numeriek eindige elementenmodel gemaakt, inclusief kristallen met kristallografische oriëntaties van eigenschappen. Ook zijn cohesive zone elementen aangebracht tussen de kristallen. De microstructuur was vooraf gemeten m.b.v. Orientation Imaging Microscopy (OIM). Zowel de wisselende temperatuurbelasting als de erop volgende trekproef zijn met het model gesimuleerd. Door fitten van experimentele en numerieke resultaten, konden de schadegroeiparameters van de interkristallijne cohesive zones worden bepaald. Een twee-dimensionaal model van de hele soldeerverbinding met daarin kristallen, kristalgrenzen, bump/pad en interkristallijne cohesive zones, is vervolgens gebruikt om vermoeiingslevensduur te voorspellen. Gebleken is dat het bezwijkgedrag afhangt van de geometrie.

Ten behoeve van een realistische analyse is een drie-dimensionaal *slice*-model van een soldeerverbinding gemaakt, bestaande uit een soldeerbump en een aangrenzend deel van chip en PCB. Ook nu is de microstructuur gemodelleerd inclusief cohesive zones in bump/pad interface en tussen kristallen. De microstructuur is gebaseerd op OIM-data van diverse SnAgCu-soldeerbumps. Modellering van defecten zoals *blow holes* is gebaseerd op statistisch onderzoek van BGA's, resulterend in gegevens over grootte, positie en aantal. Diverse modellen zijn geanalyseerd, waarna de data statistisch zijn verwerkt. Vermoeiingslevensduur wordt door de modellen voorspeld en vergeleken met gegevens uit de industriële praktijk. De invloed van de grootte, vorm en microstructuur van de soldeerbump op het bezwijkgedrag van de soldeerverbinding, is onderzocht.

Acknowledgements

With deep gratitude I would first like to thank my promoter Marc Geers, for making this thesis possible by his faith in me to manage a numerical-experimental study considering my materials science background. His positive and constructive personality combined with deep knowledge made this task an educative and a truly enjoyable one. Second, I would like to thank my copromotor Piet Schreurs. I have benefited from his everyday availability, the friendly attitude and pragmatic approach to the numerical problems. In short, Marc and Piet, it was a very pleasant and satisfactory time of my life, *hartelijk bedankt!*

I sincerely thank the committee members; prof.dr.ir. Bert Verlinden, prof.dr.ir. Jaap M.J. den Toonder, prof.dr.ir. Jeff Th.M. De Hosson, dr.ing. Steffen Wiese and prof.dr.ir. Kouchi Zhang for their valuable comments on this thesis. Special thanks to Kouchi Zhang for his supervision in 2003-2004.

I would like to thank my fellow project members, René Ubachs and Abdul Matin. It was nice to see how our work completed each other, which resulted in one numerical, one experimental and a coupled numerical-experimental work. Thanks for all the discussions and the scientific input, and all the nice time we had together during conferences! Next, I sincerely thank the STW members who had the time to join our meetings and contributed to this work by the fruitful discussions.

Marcel Kouters, Peter Teesink and Tim Assman contributed this thesis during their bachelor end projects, their work is much appreciated. Very special thanks to Hans de Vries from Philips App.Tech., for that he **always** had time for me and was **always** willing to help me. I would also like to acknowledge Willem van Driel from NXP Semiconductors for the nice discussions we had and the 'custom made specimens' in Nijmegen, in 2003-2004.

Marc van Maris, thanks for running all the machinary, teaching us how to use them, and for the good ideas in constructing challenging set-ups. Sjef, thank you very much for machining n (n>500) samples for me. Patrick & Leo, thanks for all the hardware & software you have arranged, and also for your patience in n (n>3) times changing my tea-spilled-keyboard. Alice, Yvon and Marleen, thanks for your kindness, and for not following the 'minimum answer principle' that governs this country.

I would like to thank my friends and colleagues, basically all MATE people; An-

ish, Arash, Bhairav, Erica, Frederico, Gabriel, Jan, Jesus, Johan, Katja, Hamid, Hans, Linda, Marcel, Marco, Matej, Michiel, MK, Mohammad, Murthy, Peter, Roel, Ron, Sebastiaan and Varya. Here, a special subset has to be mentioned, *the Turkish cluster*, Barış, Cem, Kanat, İsa, İzzet, Özlem and Tuncay. The lunches we had together were truly, homely.

Then, I would like to thank for all the quality time I had with Quadrivium, especially Vokollage, and The Knights (KotKT). I am very grateful to my friends in Eindhoven, Bianca, Jessica and Nele for their warm company, and to the old friends in meteabroad for the e-support to every single one of us wherever we are in the world.

My special thanks goes to all Van Meijltjes and Rullenraadjes, especially André en Lenie. There are no words to express my gratitude to my mum and dad, and my family in Ankara, who have unconditionally loved and supported me all these years. Finally, many thanks to my husband, William, for that I have the most enjoyable -even fruitful- nurdiest discussions with you, and in the mean time share such unconditional love and care. If you were a melody, it would only be the good notes.

Müge Erinç
Eindhoven, December 2007.

Curriculum Vitae

2.10.1978	Born in Ankara, Turkey.
1984–1995	Primary, secondary and high school in TED Ankara College, Ankara, Turkey.
1995–2000	Bachelor's Degree, Metallurgical & Materials Engineering Department, Middle East Technical University, Ankara, Turkey.
2001–2003	Master's Degree, Metallurgical & Materials Engineering Department, under supervision of Prof.Dr. E. Tekin, Research topic: 'Isothermal Transformations in Low Alloy Steels at Sub-Ms temperatures', Middle East Technical University, Ankara, Turkey.
2003–2007	PhD, Mechanical Engineering Department, Institute of Materials Technology, under supervision of prof.dr.ir. M.G.D. Geers, Research topic: 'Thermomechanical fatigue failure of interfaces in lead-free solders', Eindhoven University of Technology, The Netherlands.